Investigation of fluid dynamic effects of endovascular intervention in a model of descending aortic dissection

A Thesis
Presented to
The Academic Faculty

by

Joav Birjiniuk

In Partial Fulfillment
of the Requirements for the Degree
Doctor of Philsophy in the
School of Engineering

Wallace H. Coulter Department of Biomedical Engineering
Georgia Institute of Technology
Emory University
August 2017

INVESTIGATION OF FLUID DYNAMIC EFFECTS OF ENDOVASCULAR INTERVENTION IN A MODEL OF DESCENDING AORTIC DISSECTION

Approved by:

Dr. David Ku, Advisor
George P. Woodruff School of Mechanical Engineering
Georgia Institute of Technology

Dr. John Oshinski, Advisor
Wallace H. Coulter Department of Biomedical Engineering
Georgia Institute of Technology

Dr. Ravi Veeraswamy
Division of Vascular Surgery, Department of Surgery
Medical University of South Carolina

Dr. W. Robert Taylor
Wallace H. Coulter Department of Biomedical Engineering
Georgia Institute of Technology

Dr. Wei Sun
Wallace H. Coulter Department of Biomedical Engineering
Georgia Institute of Technology

Dr. J. Brandon Dixon
Wallace H. Coulter Department of Biomedical Engineering
Georgia Institute of Technology

Date Approved: April 21, 2017

*Il semble que la perfection soit atteinte non quand il n'y a plus rien à ajouter, mais
quand il n'y a plus rien à retrancher*
Perfection is finally attained not when there is no longer anything to add, but when
there is no longer anything to take away

Antoine de Saint Éxupery

Dem höchsten Gott allein zu Ehren, dem Nächsten draus sich zu belehren
To the glory of the most high God, and that my neighbor may be benefitted thereby

Johann Sebastian Bach

CONTENTS

LIST OF TABLES

LIST OF FIGURES

SUMMARY

With advances in endovascular technology and technique, **T**horacic **E**ndo**V**ascular **A**ortic **R**epair (TEVAR) has emerged as an integral component of the management of Stanford Type B dissection of the descending aorta. Whereas this modality is considered vital in the treatment of patients experiencing severe complications as a result of dissection, it has not been shown to be demonstratively superior to treatment with medical therapy alone in the absence of malperfusion, rupture, or aneurysmal degeneration. However, results from various clinical studies on the relative benefits of these therapies may be confounded by the vast heterogeneity in dissection anatomy and hemodynamics. Therefore, little is known regarding which patients should undergo TEVAR, as well as the effect of stent-graft deployment on the functional status of the aorta. In order to address this knowledge gap, compliant models of the aorta possessing a mobile intimal flap mimicking dissection were fabricated and imaged via four-dimensional phase contrast magnetic resonance (4D PCMR) imaging sensitive to fluid flow. We aimed to understand how the fluid flow varies with changes to the dissection anatomy as well as the effect of varying anatomies on the fluid shear rate, which has been related to the thrombotic potential of blood-contacting surfaces. Furthermore, we aimed to study the effects of graft deployment on these hemodynamic effects. Dissection induced flow reversal in the aorta, with concomitant low and oscillatory shear zones, which were reduced in dissections with multiple tears. Device deployment was found to restore normal hemodynamics locally, while preserving distal hemodynamic alterations. These findings suggest a potential for risk-stratification based on anatomical and functional imaging as well as more aggressive intervention to rectify aberrant fluid mechanics of the dissected aorta.

CHAPTER 1

INTRODUCTION

1.1 Type B aortic dissection

1.1.1 Pathology

Aortic dissection is the consequence of a tear of the aortic wall [1], allowing for blood flow within the tunica media (Figure 1.1). The opening of, and flow into, this potential space, known as the false lumen, promotes further separation and propagation, diverting blood away from the original, true lumen. Tracking of blood in the false lumen and subsequent propagation either antegrade or retrograde allows for separation of tissues along the dissection plane. Thus, the dissection can be transmitted antegrade to branches of the aorta, or retrograde to the aortic valve, coronary arteries, or pericardium. The former may lead to critical ischemia of the viscera or extremities, known as malperfusion syndrome, and is considered an emergent situation. The latter situation, itself urgent, may lead to fatality due to acute aortic insufficiency, myocardial infarction, or cardiac tamponade, respectively.

The urgency of both situations requires immediate intervention in order to prevent mortality and severe morbidity. However, the necessary interventions for these two situations differ significantly. In addition, dissections with cardiac complications generally arise from the ascending aorta, whereas malperfusion syndromes are usually the result of dissection of the descending aorta. Thus, simple classification of dissection based on anatomical location is useful in the management of the disease. Any dissection involving the ascending aorta is classified as Stanford Type A, whereas those relegated to the descending portion are given the Type B classification (Figure 1.2). The DeBakey classification system also makes a distinction between dissections
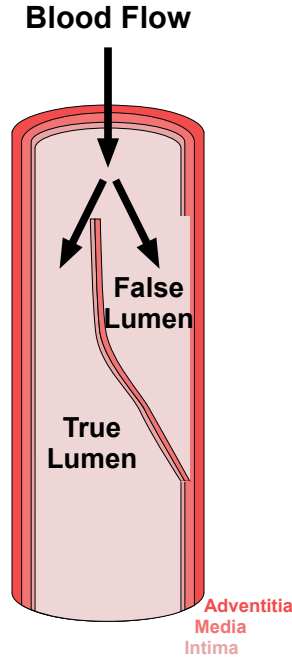
Figure 1.1: Aortic dissection is the result of a tear within the aortic lamellae

of both portions (Type I), ascending only (Type II), and descending alone (Type III). The Stanford classification is particularly quick and useful, given the increased predilection of Type A dissections for retrograde propagation towards the heart.

1.1.2 Morphology, biology, and dynamics of the intimo-medial flap and dissection lumina

The creation of the intimo-medial, or simply intimal, flap due to dissection is thought to lead to a disrupted biological and hemodynamic environment in the dissected aorta. With penetration of the inner lamellae of the aortic wall, collagen and elastin fibers become exposed to flowing blood [2–5]. This exposed matrix and protein may aid in recruitment of humoral factors involved in coagulation and inflammation, such as cytokines and matrix metalloproteinases (MMPs), which has been shown to result in degradation of these fibers [6–8]. Such processes may promote dilatation of the free aortic wall in addition to flexibility of the intimal flap. The latter is a free tissue that
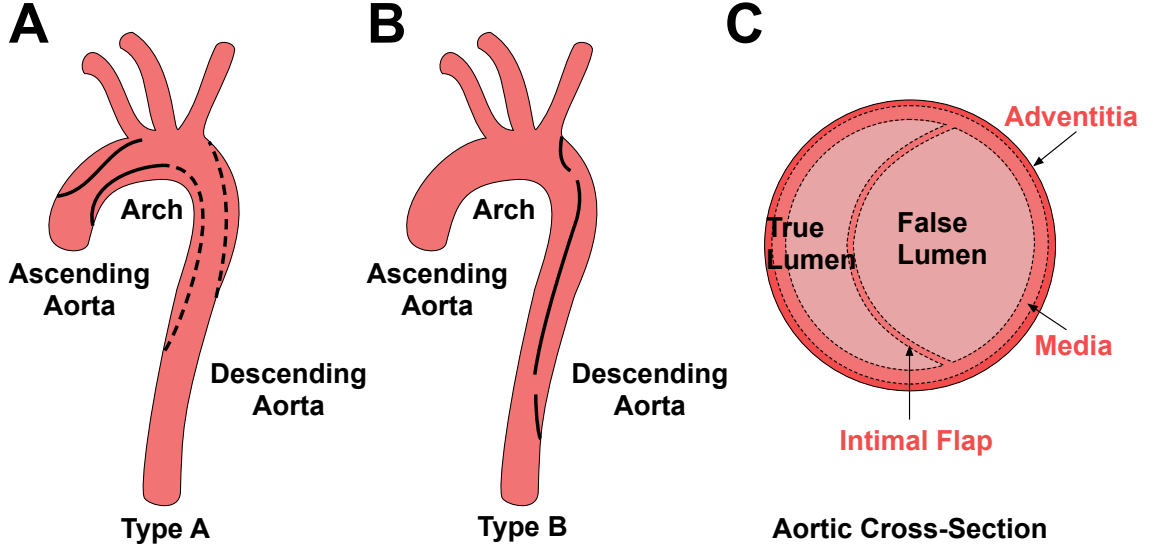
Figure 1.2: Stanford classification of dissection Type **A** and **B**. Aortic cross-section demonstrating bifurcation into true and false lumen (**C**)

may change conformation and position along the length of the dissection. Libraries of dissection morphologies have documented such changes in single dissections, as well as wide heterogeneity amongst different patients. The intimal flap is seen to take on various shapes, allowing for both true- and false-lumen dominant morphologies, with crescentic, circular, and hemicircular cross sections, among other variations [9–11]. While the morphologies and locations of true and false lumen can be identified with these imaging methods, the locations of tear sites remains difficult on static imaging [10, 11].

It has been suggested, however, that over time, inflammatory changes and fibrosis lead to stiffening of the intimal flap and free aortic wall [12], which may also lead to a less biologically active substrate. In addition to spatial changes in lumen cross-section, temporal changes can be measured with EKG-gated imaging techniques, indicating motion of the intimal flap [13, 14]. While distinct groups of dissections appear more or less likely to exhibit pulsatile motion of the intimal flap [15], greater motion is seen in the acute and sub-acute phases of the pathology [12, 15]. This observation leads credence to the suspected stabilization and increased rigidity of the

intimal flap in the chronic phase, ostensibly the result of collagen deposition within the inflamed false lumen. Thus, some reconciliation may occur between degradation via MMPs and fibrosis mediated by immune cells, leading to a stable configuration of the wall components. As rigidity and motion of fluid boundary conditions are crucial determinants of hemodynamics, these changes are expected to have drastic effect on the fluid dynamics of the aorta over time.

1.1.3 Epidemiology and burden of disease

Aortic dissection is estimated to affect 3 to 4 of every 100,000 people per annum, accounting for approximately 250,000 new cases worldwide [16, 17]. Of these, no more than 37% are relegated to the descending aorta alone [17]. While this pathology has traditionally been described as concurrent with thoracic aortic aneurysm (e.g. "dissecting aortic aneurysm" [18]), it is now understood that it may occur independently of any aneurysmal defect. In fact, in patients with co-localized aneurysm and dissection, it is unclear whether the dissection resulted from a damaged and aneurysmal aortic wall, or whether the dissected aorta dilated following the inciting event. However, as described classically, stabbing back pain is considered a definitive feature of dissection symptomatology, found to be present in nearly 95% of patients on presentation [19, 20].

The most common risk factor associated with dissection is hypertension, which is found in the history of nearly 80% of patients presenting with either type [16, 19]. Other risk factors include cocaine use and connective tissue disease, the former reported in 10% of patients with aortic dissection in the United States [16]. Patients with connective tissue syndromes are especially prone to developing dissection, with approximately 70% of all people with Marfan's syndrome developing the condition, representing 5% of all thoracic aortic dissections [16, 21]. Genomic studies have revealed familial mutations unrelated to the known connective tissue disorders asso-

ciated with development of thoracic aneurysm and dissection. These familial types are estimated to account for 22% of all non-syndromic dissections of the thorax [22].

1.1.4   Management of disease

Standard of care for any patient with a dissecting aorta is immediate initiation of beta-blocker therapy [23–25]. Such medical management is aimed at lowering the blood pressure, decreasing cardiac contractility, and decreasing the heart rate [25, 26]. This tripartite approach is thought to reduce the impulse experienced by the aorta, thus preventing further propagation or new dissection sites. In addition, the resultant decrease in cardiac afterload is meant to reduce stress on the heart [27, 28].

The immediacy of potential complications of Type A dissection, as well as its location in the ascending aorta, necessitates prompt surgical intervention via median sternotomy with replacement of the diseased segment of the aorta with synthetic graft [18, 29]. Involvement of the cephalic vessels (inominate, left common carotid, and left subclavian arteries) originating from the aortic arch may be mitigated by graft replacement [29, 30]. Any concurrent complications of the valve or coronary arteries are treated with the appropriate repair, replacement, or bypass [29]. Residual dissection of the descending aorta following Type A repair is generally treated according to the principles of Type B repair [31].

Due to the difficult technical approach to the descending aorta, as well as the significant mortality seen with such procedures, open surgery is avoided in the management of Type B dissection [19, 31–35]. With the advent of endovascular interventions for aneurysm of the thoracic aorta, these techniques have been adopted for the treatment of dissection [36–40]. Endovascular stent-graft deployment is shown to have significant benefit for patients presenting with malperfusion syndrome, aneurysmal degeneration, or suspected rupture, or who develop these complications upon admission [41–43]. However, in the absence of such complications, the role of endovascular

repair is unclear. Despite interest in its consistent use in these patients, it has not demonstrated significant mortality benefit outside of single randomized controlled trial [44, 45]. In fact, mortality rates for patients receiving intervention as an adjunct to beta-blockers remain at 10-20% in two years, as do those for patients remaining on medical therapy alone [16, 19, 33].

1.1.5   Natural history and outcomes of dissection

Though mortality rates are similar regardless of the treatment modality chosen, recent study suggests an insidious and persistent pathology in the absence of surgical or endovascular intervention. While false lumen thrombosis rates vary across studies [46–51], some prominent investigation contends that a complete hemostatic thrombosis of the false lumen, a desired outcome in the dissected aorta, is a fairly rare event in the natural history of the disease [52]. Studies from Japan have shown improved survival ranging from 20-30% at 2 and 5 years in patients with complete thrombosis of the false lumen [47, 48]. Other studies have identified partial thrombosis of the false lumen as a distinct prognostic group, portending much poorer survival, on the order of 15% [46], and accelerated aortic growth [53]. Aneurysmal degeneration of the affected segment of aorta appears to be a characteristic feature of the natural history Type B dissection when patients are managed medically and the false lumen remains canalized [54]. Several parameters, chief among them false lumen status and dissection morphology, seem to modulate the likelihood and rate of aneurysmal degeneration [50, 55–62]. Despite a lack of clear survival benefit with TEVAR, endovascular repair has been shown to restore natural luminal calibers, i.e. positive remodeling [44, 45], as well as slowing aortic growth rates [55, 57, 63–67]. In this regard, endovascular intervention may retard the formation of aneurysm, without completely eliminating the degenerative process. The pathophysiologic processes contributing to false lumen thrombosis and aneurysmal degeneration have not been clearly elucidated, but

are likely to arise from aberrations in the fluid and solid environment of the aorta. Thrombosis has been linked to changes in fluid shear stresses, while changes to hydrodynamic pressures and pulsations may contribute to solid fatigue, and ultimately, failure.

1.2 Fluid and solid mechanics of the vasculature

Given the role of end-organ malperfusion, aneurysmal dilatation, and luminal thrombosis in the progression of disease, there is great interest in understanding the fluid mechanics of dissection, along with its interaction with the solid mechanics of the aorta. Perfusion of tissues is a direct consequence of flow rates through target arteries. Formation of aneurysm is thought to result from a complex process of changes in fluid stresses and pressures that impart solid stresses on the vascular wall, leading to cyclical loading and fatiguing failure [2–5, 68]. Thrombosis is currently understood to follow from pathologically low or high fluid shear rate [69–74], which can affect the transport of active species to the endothelium and induce conformational changes to effector proteins [75–81]. A thorough understanding of the fluid mechanics governing these process is fundamental to study of this disease process.

1.2.1   Conservation principles and fluid mechanics

Fundamentally, all fluid flows adhere to the basic conservation laws of physics; that is to say, mass, momentum, and energy are conserved in any flow [82]. When derived for fluids flowing in three-dimensional space, an independent conservation equation for each of the three quantities arises, first being the mass equation:

$$\frac{\partial \rho}{\partial t} + \nabla \cdot (\rho \mathbf{u}) = 0 \tag{1.1}$$

in which ρ is the fluid density and $\mathbf{u}$ is the fluid velocity vector. This formulation of the conservation of mass is also known as the continuity equation. In the case of incompressible fluids [82], such as water and blood, this simplifies to

$$\rho\left(\nabla \cdot \mathbf{u}\right) = 0 \tag{1.2}$$

Similarly an examination of fluxes of momentum and energy yields equations for these quantities as well:

$$\underbrace{\rho\frac{D\mathbf{u}}{Dt}}_{inertial\,forces} = \underbrace{-\nabla p}_{pressure\,forces} + \underbrace{\rho\sum F_i}_{body\,forces} + \underbrace{\mu\nabla^2\mathbf{u}}_{viscous\,forces} \tag{1.3}$$

$$\rho\frac{DE}{Dt} = \rho\sum f_i + \frac{\partial}{\partial x_j}\left(\tau_{ij}u_i\right) + \nabla \cdot \left(k\nabla T\right) \tag{1.4}$$

with the former commonly referenced as the Navier-Stokes equation. Here, p is the fluid pressure field, F_i are individual body forces applied to the fluid, μ is the dynamic viscosity of the fluid, τ_{ij} the shear stress along face i in direction j, k the thermal conductivity of the fluid, and T the fluid temperature field [83]. Collectively, these three equations can provide the unique solution of the velocity vector field across space and time for a given system when the appropriate boundary conditions are applied. However, the difficulty in solving two simultaneous non-linear partial differential equations prohibits analytical solution of most biological flows. It should be noted that full knowledge of the pressure field gradient ∇p throughout the flow is required for such a solution.

Several simplifications can be made on the basis of assumptions of steady, incompressible, viscid, laminar, pressure-driven flow through pipes of circular cross-section [83], allowing us to develop some intuition as to the flow of fluids in the vasculature [84]. Known as the Hagen-Poiseuille equation, it directly relates fluid flow to spatial pressure gradients:

$$\Delta P = \frac{8\mu L}{\pi r^4} Q \tag{1.5}$$

in which ΔP is the pressure gradient driving the flow, L is the length of the conduit, r is the radius of the conduit, and Q is the volumetric fluid flow rate [85, 86]. Though vascular flows are generally unsteady, and the vasculature full of branches and changes in cross-section, this relationship can be used to estimate vascular resistances and relative flows to different components of the vascular tree.

1.2.2 Solid mechanics of the aorta

While the focus of this work is on the fluid mechanics of aortic dissection, some attention will be taken to describe the role of the relevant solid mechanics as well, as they inform upon fluid flow and pathophysiology. First, we will quickly address the interaction between fluid and solid mechanics. As the aorta is a non-rigid conduit, it will expand in an elastic fashion when it is subjected to a pressure load. This behavior is described by the compliance, C, of the aorta [84], defined as the ratio of change in volume (ΔV) of the vessel to the pressure load applied (ΔP):

$$C = \frac{\Delta V}{\Delta P} \tag{1.6}$$

This compliance is fairly constant over the normal operating range of the aorta (50 - 200 mmHg). Not only does the fluid inform upon the solid via pressure, but changes in the solid dimensions affect the fluid mechanics via a change in the geometric boundary conditions. However, the stretch on the aorta as a result of pressure loading presents a negligible contribution to changes in fluid mechanics. Alternatively, the geometric changes seen with aneurysmal aorta present considerable changes to the boundary conditions of the fluid field.

While the vessel can accommodate pressure loads, such loading conditions induce

circumferential stresses, commonly known as hoop stresses, upon the aortic wall [84]. This stress is directly related to the pressure, P, and vessel radius r, while inversely related to the vessel wall thickness t:

$$\sigma_\theta = \frac{Pr}{t} \qquad (1.7)$$

Thus an increase in hydrodynamic pressure is seen to contribute to greater stress in the aortic wall. In excess of a certain threshold, such pressure loading is thought to induce microscopic fractures of the medial architecture, resulting in an inflammatory response and progressive remodeling. Eventually, the wall may decrease in thickness with a concomitant increase in vascular caliber, perpetuating greater wall tension. Continued cyclical loading in such a fashion is therefore linked with degradation of the vessel wall and eventual aneurysm formation. Though the absolute or mean arterial pressure (MAP) may not contribute to aortic fluid flow patterns, it is suspected to play an important role in vascular remodeling and the degeneration of the aortic wall.

1.2.3   Fluid flow and the vasculature

Equipped with this basis, we can begin to understand some of the idiosyncrasies of blood flow in the human vasculature that are of clinical interest. By combining the resistive (Equation 1.5) and compliant (Equation 1.6) aspects of the vascular wall, we can observe that it is capable of both dissipating and storing energy. As mentioned earlier, viscous (resistive) interactions between fluid and boundaries leads to the dissipation of fluid energy. Conversely, if no changes occur to the integrity of the vessel wall, i.e. the wall maintains nearly perfect elastic rebound from pressure changes, mechanical accommodations to fluid pressure can be seen as energy-storing processes. We can therefore view the addition of superfluous boundaries, as with the additional lumen in dissection, as adding resistance to fluid flow, and the formation of components accommodating of pressure, such as the intimal flap, contributing to

storage of fluid energy. However, the inelastic interactions of the fluid and intimal flap may lead to dissipation of energy as well. These seemingly contradictory forces complicate prediction of overall behavior of the dissection.

Unlike the simplified solutions for straight pipes, the aorta possesses a significant curvature along its extent from the aortic root to the proximal descending portion. This feature of the aorta leads to three important peculiarities of fluid flow within it. First, as the fluid moving along the inner curvature of the vessel experiences a much sharper change of angle, it loses momentum relative to the fluid near the outer curvature, leading to a skewing of the velocity profile towards said curvature. This skewing is relieved by approximately the mid-thoracic descending aorta. Second, as a result of this fluid impinging upon the greater curvature, a reflection of the fluid momentum across the transverse plane occurs, inducing helical secondary flows *revolving* about the longitudinal aortic axis. Lastly, the aforementioned impingement contributes a reflection in angular momentum, imparting a *rotational* component about individual fluid element axes to these vortical structures.

1.2.4 Fluid models of aortic dissection

Given the aforementioned difficulties in solving the governing equations analytically, models are necessary to approximate disease conditions the resulting velocity fields. These models may be computational in nature, employing numerical simulations of discretized forms of the conservation equations to solve for the velocity field; or experimental, in which appropriate flow conditions and boundary geometries are approximated and flow fields measured empirically. The former method is able to compute hemodynamic parameters of interest at very high resolutions in complex geometries [87, 88], but is subject to limiting assumptions of boundary conditions inputted into the model [89]. In addition, motion of solid components within the flow, as with the dissection septum, is rather difficult to model [90–92]. As such, most computational

models of aortic dissection are predicated upon the assumption of immobile solid components (both aortic wall and dissection septum). While not subject to the vagaries of boundary condition assumptions, the latter approach requires robust experimental setup, and cannot acquire velocity fields at arbitrarily high resolutions.

A good model of dissection should approximate the original pathology as closely as possible while allowing for sufficient interrogation of the relevant hemodynamic parameters. As such, it should be amenable to systematic perturbation of anatomy [93] and device deployment [94, 95], and aid in developing some intuition as to the underlying fluid mechanics principles in the dissected aorta [96, 97]. Previous computational models of dissection have yielded some understanding of recirculatory flows in aneurysmal false lumen [98–100], shear stresses throughout the dissection, and potential regions of platelet activation [101, 102]. These models, however, have considered the intimal flap a rigid member maintaining a static profile in the flow field. As predicted earlier, the motion of the flap may have a significant contribution to the resulting hemodynamics [103]. In addition, the patient-specific geometries of some of these models bars deriving general principles regarding the influence of anatomy on patient hemodynamics. Several groups have developed experimental models of dissection utilizing phantoms made of synthetic materials with mobile dissection septa [104–108]. However, due to the difficulty of fabricating an anatomically relevant phantom, these have largely used straight-tube models of the descending aorta, ignoring the hemodynamic effects of flow through the aortic arch. Despite these shortcomings, an experimental model is considered ideal for study of dissection with intimal flap mobility, which is generally the case in acute dissection. Flow loops with *ex vivo* porcine [109, 110] and human [111] aorta have been used, but are difficult to maintain leak-free and are far less stable than synthetic models.

1.3 Phase contrast magnetic resonance imaging

In addition to selection of a relevant model system, study of dissection hemodynamics requires an adequate measurement of fluid velocities. Previous studies have utilized Doppler ultrasound in order to acquire tomographic images demonstrating flow in the direction of the transducer [103, 105]. Though a useful tool, it is limited by impedance matching issues with phantom materials, single slice acquisitions, and sensitivity to flows along a single axis [112]. Particle image velocimetry (PIV) can be used to compute planar velocity fields via resolution of velocity components in two directions orthogonal to the interrogation axis at high spatial resolution. However, it requires sufficient optical clearance through the phantom material, complex optics for measurement, and is unable to acquire velocities along the interrogation axis. In order to acquire full velocity fields in three orthogonal Cartesian directions, four-dimensional phase contrast magnetic resonance (4D PCMR) imaging is employed.

1.3.1 Principles of flow MRI

Phase contrast velocity mapping capitalizes on the innate dependence of the phase of a particle's angular spin momentum on its velocity [113]. Thus, measured phase shifts in the spin signal can be translated directly to the particle's velocity. Such a phase shift can be observed by applying a gradient field to the subject in the direction of interest and comparing to a coherent reference gradient field of a different amplitude and pulse width. Subtraction of these acquisitions removes common mode noise, yielding the phase shift incurred by moving fluid within the field. Application of such gradient fields in three orthogonal axes with near simultaneous acquisition allows for interrogation of three-dimensional velocity fields across imaging planes. Fourier transform of the MR signal yields both magnitude and phase data for each of the Cartesian directions (Figure 1.3). Coherent, EKG-gated image acquisition affords
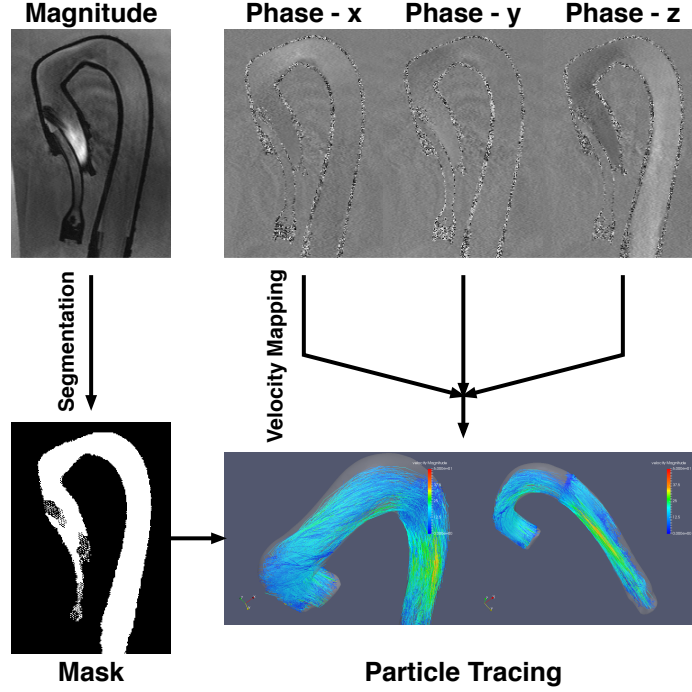
Figure 1.3: Four-dimensional PCMR yields both magnitude and phase data. The former can be used for aortic volume segmentation, while the latter encodes velocity information

the ability to resolve components of the velocity field in time, known as 4D PCMR. Due to the long scan times necessary for full volumes, respiratory gating with a liver-diaphragm navigator is often used to account for breathing motion.

1.3.2 Advantages and limitations of PCMR

As PCMR employs intrinsic signal from relaxation of spins in human tissues, it performs non-invasive imaging with non-ionizing radiation, allowing for clinical adoption without concern for endangering patients or volunteers. In addition, large field of views may be acquired, which can be used to reconstruct velocity fields across full volumes of interest. Magnitude images acquired in simultaneity with the phase shift images allow for easy visualization of the vascular anatomy and dissection septum [114–116]. Furthermore, acquisition of velocity components in all directions allows for understanding of complex and secondary flows within the vessel [117–122].

PCMR does however have limitations inherent to the imaging system and mode

14

of acquisition. Due to the finite sensitivity of coil elements used to measure MR signal and to the size of the magnetic field gradient to be generated, there is a limit to the spatial resolution of resulting MR images [113]. This resolution is further degraded by the realistic limits of patient stillness, respiratory gating, and limitations on scan times for patient comfort. As a result of this resolution limit, flow MRI is subject to partial volume effects, which arise from the presence of both flowing and static material, or materials of greatly different velocity, within a given finite voxel. Thus, the reporting of the full voxel as possessing the greater velocity can result in an overestimation of the true velocity. Additionally, as EKG-gated sequences are acquired over numerous cardiac cycles, significant temporal averaging may occur. This can result in the loss of certain flow features that vary from cycle to cycle or have high levels of disorder. Alternately, coherent fluid structures are reinforced and amplified with this methodology.

Despite the shortcomings of this technology, it is of particular use for the study of aortic dissection as it can be used to acquire full flow fields fairly easily. The resulting velocity measurements can be used to calculate flow and shear rates and provide useful intuition as to the movement of fluid within the pathological aorta.

1.4   Aims and Objectives

1.4.1   Unmet needs in the diagnosis and treatment of Type B dissection

Due to the dearth of knowledge regarding Type B aortic dissection, this pathology presents a unique challenge to the clinician. Despite the availability of state-of-the-art technology, patients may fair poorly due to hidden features of disease that may predispose to aneurysmal degeneration. Little is known regarding the natural history of disease [123], as intervention is often pursued in anticipation of adverse patho-physiologic processes, further confounding the results observed. To aid in improving outcomes with endovascular intervention, we aim to gain some understanding to these

fundamental questions:

- **Which** patients require endovascular intervention?

- **Can** we predict some of the natural history of Type B dissection?

- **How** can stent-graft deployment be optimized to improve aortic hemodynamics while minimizing complications?

While more complete answers and stronger evidence may be gained from clinical study, this investigation into the fluid mechanics of dissection is aimed at providing some intuition as to the altered hemodynamics encountered with a mobile flap in the divided aorta, the use of dynamic imaging in the assessment of these hemodynamic changes, and the utility of endovascular stent-graft devices in restoring aortic fluid mechanics to normal. As such, the **overal goal** of this work is to determine which patients should receive endovascular intervention, and how such intervention should be deployed. To this end, three aims were proposed to answer these questions:

1.4.2   Risk stratification based on dissection anatomy and altered hemodynamics

Proper patient selection is of utmost importance in the treatment of aortic dissection. Though standard surgical considerations are weighed in choosing appropriate candidates for endovascular repair, fluid dynamic considerations beyond pressure are largely ignored as indications for intervention. Currently, outside of the aforementioned complications and increasing aortic diameter [10, 11, 50, 124], there are no clear indications for endovascular repair. Thus, some patients may receive unnecessary intervention, while others at risk of persistent dissection and eventual degeneration go without more definitive treatment.

Various clinical studies have attempted to characterize (primarily static) features of dissection that are associated with a greater risk of mortality, adverse events, or need for intervention. Such work has elucidated parameters such as false lumen size

[48, 50] and thrombosis [47, 49, 51, 57, 59, 65, 125], tear size, tear location, and tear number [50, 56] as indicators for outcomes in patients with uncomplicated dissection. However, these studies have ignored the fluid mechanics of individual patient dissections, which may vary widely and inform upon disease progression. Such functional features of an individual patient's dissection may play a role in the risk of developing aneurysm and other indications for super-medical intervention. In order to understand the hemodynamic heterogeneity that is thought to arise from anatomical differences between dissections, and identify potential risks based on said heterogeneity, we employed models of dissection with slight variations in intimal flap anatomy in our fluid flow study. We aimed to characterize differences in fluid dynamics between these models of varying dissection anatomy.

Aim 1: To determine the changes to normal aortic hemodynamics resulting from dissection of varying anatomy.

1.4.3 Calculation of wall shear rate for prediction of thrombosis

Thrombosis of the false lumen, which may occur as a natural consequence of altered hemodynamics in the dissected aorta, may also portend a more positive prognosis for patients [47, 48, 51]. As mentioned earlier, occlusion of the false lumen with thrombus may prevent flow within it, improving perfusion of tissues still supplied by the true lumen [46, 62, 126]. In addition, thrombosis of the vasculature can resolve over time leading to adequate remodeling of the given vessel, i.e. the false lumen. Reduction of false lumen caliber with its eventual resorption coupled with restoration of flow to the true lumen is considered a positive outcome in the resolution of disease. Thus, prediction of which patients will undergo natural thrombosis of the false lumen may aid in the previous aim of determining which patients are most in need of intervention. While techniques have been developed to image the presence of intraluminal thrombus more accurately, the ability to predict the evolution of false

lumen thrombosis over time does not yet exist. Such a technological advance would prove useful to the clinician not only in determining the need for intervention, but also in surgical planning by optimizing induced and natural thrombosis with a minimal number of devices.

Real-time assessment of thrombosis requires a knowledge of flows and biochemical species throughout space and time, a nearly impossible task. However, given our knowledge of the relationship between fluid mechanics and thrombosis, we may be able to provide general predictions of zones more or less likely to thrombose given oscillatory shear and shear magnitudes throughout the flow field. To this end, we aimed to develop a methodology to quickly estimate the order of magnitude of shear rates and stresses experienced at the aortic wall using a clinically-available imaging technique. In addition, we wished to use this methodology to assess the thrombotic potential of the dissection anatomies being investigated.

Aim 2: To identify regions of oscillatory and pathologic shear rate in the dissected aorta.

1.4.4 Hemodynamic effect of endovascular intervention

Despite over ten years of experience in endovascular repair of the dissected aorta, the effectiveness of this intervention in patients absent complications is unclear. As mentioned above, this is complicated by heterogeneities amongst the dissections and lack of understanding of which patients will benefit most from intervention. In addition, it is not clear whether the failings are due to inadequacies of the devices for the given indication or non-optimal deployment strategies. Currently, most prognostic, planning, and followup evaluation of the aorta is performed with static, structural imaging, which is insufficient in assessing the hemodynamic outcomes of a given procedure. Thus, it is unknown whether any hemodynamic advantage is achieved with deployment of endografts as purported.

Obvious ethical, technical, and scientific concerns prevent testing of deployment strategies in patients in controlled experimental conditions. With the use of an *in vitro* model, however, we can systematically deploy, retrieve, and redeploy devices with precise knowledge of their location in a controlled setting. Furthermore, MRI velocimetry affords us the ability to acquire the flow field throughout the aortic volume for comparison of hemodynamics across various experimental groups. An assessment of fluid flow changes resulting from stent-graft deployment, including proximity to normal flow patterns and regions of potential thrombosis, would be a useful adjunct to anatomical imaging typically used for procedural followup. In addition, it could determine whether apposition of the intimal flap to the external wall of the false lumen is sufficient in restoring aortic hemodynamics. To this end, we aimed to understand gross changes to the flow field resulting from endovascular exclusion of the proximal entry and subsequent tear sites.

Aim 3: To assess the restoration of normal hemodynamics to the dissected aorta following endovascular intervention.

CHAPTER 2
DEVELOPMENT AND TESTING OF A SILICONE *IN VITRO* MODEL OF DESCENDING AORTIC DISSECTION

2.1 Introduction

2.1.1 Pathophysiology and management of aortic dissection

Aortic dissection is a tearing of the aortic wall, typically between intimal and medial layers. This tearing may be due to ischemic injury and effacement of the normal lamellar structure of the aortic wall [4, 5]. Once a tear has been initiated, blood flows into the space between aortic layers creating two distinct flow lumina, propagating the dissection in various directions along the aorta. There is usually an "entry tear" at the start of the dissection and a variable number of "reentry tears" along the aorta that allow communication between the two lumina.

Patients with type B dissections are generally treated medically unless clinical suspicion prompts endovascular intervention. Such interventions include placement of thoracic stent grafts to occlude tear sites and obliterate false lumen flow, fenestration of intimal flaps to allow perfusion of occluded vessels, and branch vessel stenting [3-5] [44, 127, 128]. These various techniques may be combined, depending on the needs of the given patient.

Medically managed patients have poor long-term outcomes, however, with complications including false lumen aneurysmal dilation, need for aortic intervention, and significant mortality rates in the first 3 years [129–131]. Currently, there is limited understanding of the fluid mechanics underlying these clinical outcomes. Flow patterns, pressure, shear rates, and luminal volumes are difficult to measure. The effects of these variables on dynamic dissection flap movement, occlusion of distal branch

vessels, and long-term aneurysmal degeneration are not well described. This scarcity of data may be supplemented by use of a model system in which these parameters can be studied. We present initial data from a novel silicone model that replicate type B aortic dissections and use four-dimensional phase-contrast magnetic resonance imaging (4D PC-MRI) techniques to measure flow parameters.

2.1.2   Phase contrast MRI

Four dimensional PC-MRI is a technique for determining the velocity of moving fluid in an MR scan. When a proton spin is subjected to a magnetic field gradient, any motion in the direction of the gradient will induce a phase shift proportional to the in-plane velocity. A pair of magnetic field gradients is applied sequentially to the coil to provide a phase-differential image [113]. The differential mode signal eliminates static components of the MR image. Flow rates can then be calculated based on the measured velocity profiles. This technique is currently being used in patients to interrogate aortic flow dynamics without invasive procedures [132, 133].

2.1.3   Flow division model

Because of the flow division present in a dissected aorta, the pathology can be modeled as two flows in parallel initiating from a common node. This can be described in similar terms as an electric circuit with resistive elements, illustrated in Figure 2.1. Because mass, and hence flow rates, must be conserved, the individual flows in each branch of the conduit must add to the total flow entering the node, and the pressure drops across both branches must be equal. In addition, the branch resistances can be added together as resistances in parallel, yielding the following overall resistance:

$$R_{tot} = \left(\frac{1}{R_T} + \frac{1}{R_F} \right)^{-1} = \left(\frac{R_F}{R_T R_F} + \frac{R_T}{R_T R_F} \right)^{-1} = \left(\frac{R_F + R_T}{R_T R_F} \right)^{-1} = \frac{R_T R_F}{R_F + R_T} \ (2.1)$$
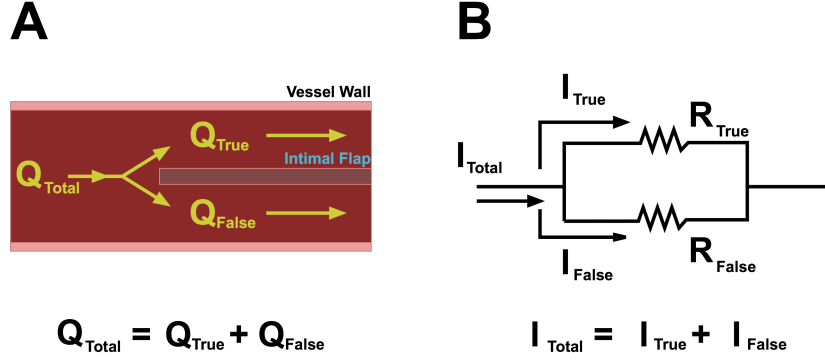
Figure 2.1: Flow division in flow loop (**A**) and analog electrical circuit (**B**).

where R_{tot} is the total resistance, R_F is the false lumen resistance, and R_T is the true lumen resistance. Because the pressure drop across the branches must equal the product of resistance and flow rate, expressions for the branch flow rates can be determined as follows:

$$\Delta P = Q_{tot} R_{tot} = Q_{tot} \frac{R_T R_F}{R_F + R_T} = Q_F R_F = Q_T R_T \tag{2.2}$$

$$\frac{Q_F}{Q_{tot}} = \frac{R_F R_T}{(R_F + R_T) R_F} = \frac{R_T}{R_F + R_T} \tag{2.3}$$

Furthermore, Poiseuille's law states that the resistance of a conduit of circular cross section is inversely proportional to the radius raised to the fourth power, and therefore, its area squared [85, 86]. Thus, assuming that the branches have circular cross section, and that the impedance of conduits are purely resistive (i.e., rigid), the flow ratios can be rewritten as follows:

$$\frac{Q_F}{Q_{tot}} = \frac{\frac{1}{A_T^2}}{\frac{1}{A_F^2} + \frac{1}{A_T^2}} = \frac{\frac{1}{A_T^2}}{\frac{A_T^2 + A_F^2}{A_F^2 A_T^2}} = \frac{A_F^2}{A_T^2 + A_F^2} \tag{2.4}$$

yielding an expression for the flow rate based on the cross-sectional areas of the respective branches.

2.1.4   Objectives and hypothesis

We seek to recapitulate human aortic anatomy and create a silicone model of a type B dissection. As opposed to previous work in the field [106, 107], this model possesses a compliant, mobile intimal flap and anatomically accurate entry tears and dimensions. It is predicted that this model will demonstrate basic flow conservation and that the PC-MRI data can be used to successfully interrogate flow dynamics in the dissected aorta.

2.2   Methods

2.2.1   Model fabrication

Clinical computed tomography images of human aorta were acquired, segmented, and reconstructed to form three- dimensional models *in silico*. These were subsequently used to rapidly prototype molds for fabrication of silicone models. A two-mold process was used to produce silicone models with intimal flaps that could be distended. First, a 0.5-mm intimal layer was cast on the true lumen mold with silicone. Once released from the initial mold, a polyvinyl alcohol mold release (TAP Plastics, Stockton, CA) was applied to an area on the external portion of the cast delineated as the flap. A second casting was performed over the initial cast using a different silicone product. Once demolded, the flap was incised along proximal and distal portions, which was then elevated from the second (outer) casting. The aortic model possessed a three-dimensional curvature but contained no branching vessels (Figure 2.2). The silicone used for this model has a reported stiffness in the range of 1-10 MPa [134, 135], similar to human aorta in normotensive strain 0.5-10 MPa) [136–138].
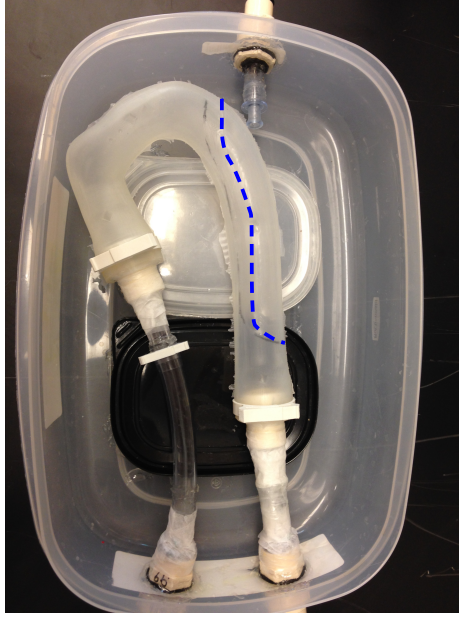
Figure 2.2: Silicone model of aortic dissection demonstrating anatomic morphology and intimo-medial flap (dashed blue line).

2.2.2   Flow loop setup

Medical-grade polyvinyl chloride tubing was connected to the model via appropriate fittings in a single closed loop. Model inlet and outlet were fitted with branched adapters to allow catheter access to the model. Both tubing and models were filled with 35% by volume glycerol in water to mimic the density and viscosity of human blood under physiologic flow conditions at room temperature. Fluid was added until an aortic arch pressure of 100 mm Hg was reached. The flow loop was placed on a positive displacement perfusion pump (COBE, Century Heart Lung; Medtronic, Inc., Minneapolis, MN) to achieve continuous flow at a rate of 5 L/min.

2.2.3   Imaging and analysis

The model was imaged in an MR scanner using a 4D PC-MRI protocol. These data were used to visualize particle streams using Siemens 4D Flow (Siemens Medical Solutions USA, Malvern, PA) and to measure velocity and calculate flow rate using custom-made analysis software (Matlab, The Mathworks, MA). Magnitude and phase

data from 4D PCMR scans were imported and used to visualize the aortic contour. Velocity profiles and cross-sectional areas were calculated in planes chosen perpendicular to the aortic wall, in which a given region of interest of vessel lumen was selected manually. Velocity vectors with components normal to the selection plane were calculated from the original velocities. These profiles were integrated over the cross-sectional area to determine volumetric flow rate. In planes passing through the dissected region, the true and false lumina were segmented and treated independently. Flow rates for each region of interest were averaged over 13 time points in the MR scan. Measurements were repeated five times per aortic level.

2.3 Results

2.3.1 Lumen cross section

The cross sections of both true and false lumen varied longi- tudinally along the dissection, as seen in Figure 2.3. In the proximal portion at the level of the entry tear, the false lumen assumed a nearly circular profile, whereas the true lumen had a crescent-like shape. However, in the mid-thoracic region and at the level of the exit tear, the true lumen was circular in shape, whereas the false lumen appeared crescent-like. The area percentage of false lumen increased from 35%-39% along the length of the dissection, whereas the true lumen area percentage decreased from 65%-61%.

2.3.2 Flow rates and ratios

A summary of the resultant flow rates, cross-sectional areas, and flow ratios is listed in Tables 2.1 and 2.2. True lumen flow rate was 3.1 ± 0.8 L/min and false lumen flow rate 1.4 ± 0.6 L/min (Table 2.1), which were significantly different when averaged over all levels of dissection (P < 0.05). The summed true and false lumen flow rates averaged 4.5 ± 1.2 L/min, comparable with the input flow. At the level of the entry tear, true lumen, false lumen, and total flows were 2.8 ± 0.6, 2.0 ± 0.6, 4.8 ± 1.2 L/
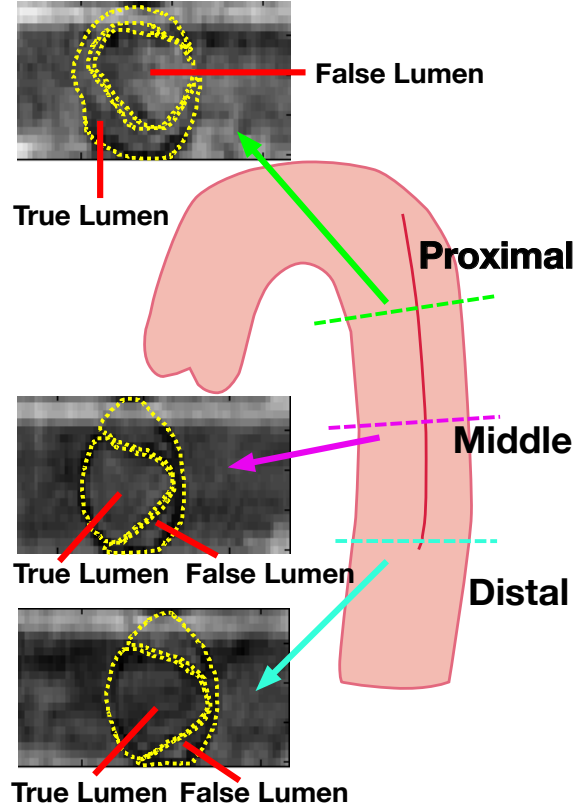
Figure 2.3: Location of plane sections along aortic model with representative axial plane images. True and false lumina are outlined in yellow.

min, respectively. In the middle of the dissection, these flow rates were measured to be 3.9 ± 0.3, 1.5 ± 0.2, and 5.4 ± 0.6 L/ min, respectively. Exit tear flow rates were 2.5 ± 0.4, 0.85 ± 0.1, and 3.3 ± 0.3 L/min for true, false, and total lumens, respectively.

Luminal flow rate ratios were controlled by the resistances that are proportional to the area ratios squared at the middle and exit tear levels (Table 2.2). Mid-dissection resistance weights were 71% and 29% for true and false lumen, with corresponding flow percentages of 72% and 28%, respectively. Furthermore, at the exit tear level, the true and false lumen resistance weights of 70% and 30% correspond to the measured flow divisions of 74% and 26%. Resistance weights of 76% and 24% corresponded to flow divisions of 59% and 41% for the true and false lumen at the level of the entry tear.

Table 2.1: Flow rates and ratios

Location	Q_T (L/min)	Q_F (L/min)	Q_{tot} (L/min)	$\dfrac{Q_T}{Q_{tot}}$ (%)	$\dfrac{Q_F}{Q_{tot}}$ (%)
Proximal	2.8	2.0	4.8	59	41
Middle	3.9	1.5	5.4	72	28
Distal	2.5	0.8	3.3	74	26
Overall					
Mean	3.1	1.4	4.5	74	26
Standard Deviation	0.8	0.6	1.2	5.3	5.3

Table 2.2: Relative cross-sectional area and resistance (squared area weights) for the true (T) and false (F) lumina

Location	$\dfrac{A_T}{A_T + A_F}$ (%)	$\dfrac{A_F}{A_T + A_F}$ (%)	$\dfrac{A_T^2}{A_T^2 + A_F^2}$ (%)	$\dfrac{A_T^2}{A_T^2 + A_F^2}$ (%)
Proximal	65	35	76	24
Middle	61	39	71	29
Distal	61	39	70	30
Overall				
Mean	61	39	73	27
Standard Deviation	2.3	2.3	6.0	6.0

2.4 Discussion

We describe the use of an elastic, true-scale silicone model of a dissected aorta based on actual computed tomography images of the anatomy of a patient presenting with flow through both true and false lumen. An aqueous glycerine solution with the viscosity of human blood was perfused through the model at physiologic flow rates. Local velocity was measured using phase-contrast MRI angiography. The MRI measurements were used to calculate the flow divisions and volume flow rates through each lumen with high reproducibility for a Stanford type B aortic dissection. The combination of PC-MRI and analysis software can be used to estimate local shear rates through the false

lumen. These tools may be used in future studies to further investigate hemodynamics of the dissected aorta in a systematic and thorough manner.

2.4.1 Flow division model and observation

As predicted by theory, flow in the true and false lumen was proportional to the resistances in the lumen, which can be estimated by the square of the cross-sectional area of each lumen. Resistance values may be more accurately computed using computational fluid dynamics studies to account for the abnormal shapes seen. In the more distal portion of the dissection, the area of the true lumen matched more closely the assumption of circular cross section. Our resistance-based approach assumed that the impedance of the division had no capacitive elements. Both native and silicone model aorta have a significant compliance that yield such a capacitive effect.

2.4.2 Limitations and future work

Though effective in establishing a framework for investigation, this work is limited by several fundamental shortcomings. The current model does not include the cephalic vessels that would likely cause significant skewing of velocity profiles toward the greater curvature of the arch. The addition of a branch vessel may allow for control of flow from the inlet to a specified amount at the proximal descending aorta. This modification may alter the flow profile at the arch, therefore, affecting the flow conditions into the dissection.

An additional limitation is that a single dissection geometry was created for this study. Nonetheless, the physical model may be used to generate alternative tear locations and sizes that can be controlled easily and systematically to generate additional conformations. Clinical evidence suggests that large proximal tears increase patients' risk of mortality and aorta-related complications [56]. The ability to adjust tear morphology in a consistent and controlled fashion will allow for study of flow variation

as a function of entry parameters. Furthermore, the number of tears has been shown to correlate with false lumen thrombosis as well as aortic growth and remodeling in long-term studies [139, 140]. The modularity of this model makes investigation of the fluid dynamic effects of tear number, morphology, and location feasible.

In the model, the false lumen exhibited a range of cross- sectional shapes, including a crescent shape seen in Figure 3, noted in the common clinical presentation of dissection in which the false lumen compresses the true lumen [10, 141, 142]. The intricacies of human blood flow may aid in opening and distension of the intimal flap along its extent.

One critical component to this study was the use of a roller pump for flow rather than a physiologic pulsatile flow waveform. Maintaining physiologic continuous flow rates in this pilot study was far less complicated but may omit dynamic variations in pressure and flow that impact dissection propagation. Additionally, pulsatile flow may have an influence on the flow profile seen in various locations throughout the aorta, ultimately affecting entry tear flow. Future work will develop and investigate a pulsatile flow system that can generate a physiologic waveform while maintaining physiologic flow rate or cardiac index.

Lastly, total flow rates calculated varied along the dissection (Table 2.1), with a mean of 4.5 L/min and standard deviation of 1.2 L/min. This may be the result of phase gradients encountered in PCMR sequences. However, relative luminal flow rates were conserved along the extent of dissection.

2.4.3   Clinical implications

We have demonstrated the ability to measure and direct flow through the true and false lumen in an in vitro model of a dissected aorta. The resultant velocity vectors may be used to determine flow in the different lumen and calculate shear rates relevant to likelihood of thrombosis. The ability to vary tear and flap geometries in an in

vitro model may allow for these principles to be applied to specific patient geometries. Future studies can quantify the alterations to flow in the dissected aorta with stenting. We will incorporate systematic variations in anatomic dissections in future models to develop general principles that may be used to guide clinical practice.

CHAPTER 3

PULSATILE FLOW LEADS TO INTIMAL FLAP MOTION AND FLOW REVERSAL IN AN *IN VITRO* MODEL OF TYPE B AORTIC DISSECTION

3.1 Introduction

3.1.1 Management of Type B aortic dissection

Thoracic aortic dissection is a potentially fatal condition of the aortic wall affecting between 3 to 4 people per 100,000 yearly [16, 17]. Tearing between the layers of the aorta diverts blood flow away from the true lumen into the newly created false lumen, which may result in critical malperfusion of the viscera. Overall in-hospital mortality for patients with Stanford Type B dissection, constrained to the descending aorta, remains at approximately 13% [143]. These patients are initiated on beta-blocker therapy, but may also undergo stent-graft repair of the aorta. In-hospital mortality for both populations remains at 10%, with a nearly 20% three-year mortality rate for those surviving hospital stay [27, 143]. It has been suggested that endovascular intervention in this patient population may promote improved remodeling (i.e. restoration of lumen caliber and flow) of the aorta [44, 45], mitigating long-term sequelae including aneurysm formation. However, it remains unclear why some patients progress to aneurysmal degeneration following endovascular therapy [27, 44], whereas others remain stable with medical therapy alone.

3.1.2 Consequences of hemodynamics

The fluid mechanics of the dissected aorta may be intimately tied to patient outcomes. False lumen thrombosis has emerged as a predictor of patient outcomes, and may

explain some of the observed variability in outcomes [46, 47]. Current understanding implicates pathologic fluid shear rate as a central mediator of thrombosis [71, 144]. In addition, low and oscillatory wall shear stress is implicated in atherogenesis [145, 146] and endothelial dysfunction [147, 148], ultimately contributing to unfavorable vascular remodeling [69, 148–151] and potential aneurysmal degeneration. A better understanding of these phenomena may lead to enhanced outcomes prediction, patient selection, and device design.

3.1.3   Computational and experimental models of dissection

Both computational and experimental approaches have been used to characterize the effects of dissection on aortic hemodynamics. Computational fluid dynamics (CFD) models based on patient-specific aortae have yielded flow fields and shear stresses throughout the aorta at high spatial resolution [97, 99, 152]. While CFD studies have identified foci of shear extrema, these models have assumed a rigid aortic wall and fixed intimal flap. Lumped parameter models of aortic dissection have shown significantly different hemodynamics between rigid and compliant aortae [103], with varying modes of flow across dissection tears, indicating a need for physiologically compliant models. More recent computational studies have looked to model fluid-structure interactions between the blood and aortic wall [92], but have yet to include a mobile intimal flap. Some in vitro models of dissection possess some compliant features, but have also assumed either rigid flap [106] or a non-anatomic aortic geometry [105, 106]. Full flow fields have not been measured in these physical models [107, 108], limiting the understanding of salient hemodynamic phenomena, namely flow reversal, secondary flows, and oscillatory shear rate.

3.1.4   Objectives and hypothesis

In order to study the effects of dissection on the hemodynamics of the aorta, we employed a compliant flow phantom of the aorta with a mobile intimal flap [153] subjected to pulsatile flow. By scanning the phantom using 4D phase contrast magnetic resonance imaging (PCMR), full flow fields were acquired throughout the thoracic aorta [113]. This study was aimed at determining changes to normal aortic hemodynamic indices, in particular flow rate and flow reversal, under physiologic flow conditions in the presence of a dissection. It is hypothesized that under these conditions, the dissected aorta will exhibit increased flow reversal and disruption of pulsatile blood flow as compared to normal.

3.2   Methods

3.2.1   Flow loop setup

Silicone models of aortic dissection were fabricated as previously described [153]. Briefly, aortic molds were rapid-prototyped from segmented patient CT images. Silicone was cast around the molds in a two-step process in order to form an independent dissection flap and aortic wall. Entry and exit tears (one each) were incised circumferentially along the flap on the lateral wall at the flexure of the lesser curvature of the aorta and at a distance four centimeters proximal to the distal lip of the model, respectively (Figure 3.1B). Models (one each of normal and dissected) were installed in a flow loop (Figure 3.1A) and filled with water to a mean arterial pressure (MAP) of 100 mmHg. Rigid, fiber-reinforced polyvinyl chloride (PVC) tubing was used on the inlet-side of the model to transmit pressure waveforms of 140/80 mmHg with high fidelity (Figure 3.2). Physiologic flow was initiated at a cardiac index of 4 L/min via a custom-made pulsatile positive-displacement pump and measured with a flow meter (Transonic, Ithaca, NY). The pump consisted of a rubber impeller (Oberdorfer

Pumps, Syracuse, NY) driven by a rotary servo motor and drive (Parker Hannifin, Charlotte, NC), and controlled externally via a custom Labview Virtual Interface (National Instruments, Austin, TX). Voltage-flow rate curves were generated to calibrate pump output with regards to the length of tubing necessary to reach from the control room to the MR scanner. Output waveforms were based on previously reported flow waveforms acquired from physiologic measurement [154]. A multipurpose access catheter (Cook Medical, Bloomington, IA) was advanced antegrade to the proximal ascending aorta and connected to a blood pressure transducer (Harvard Apparatus, Cambridge, MA) to record pressure in the model.
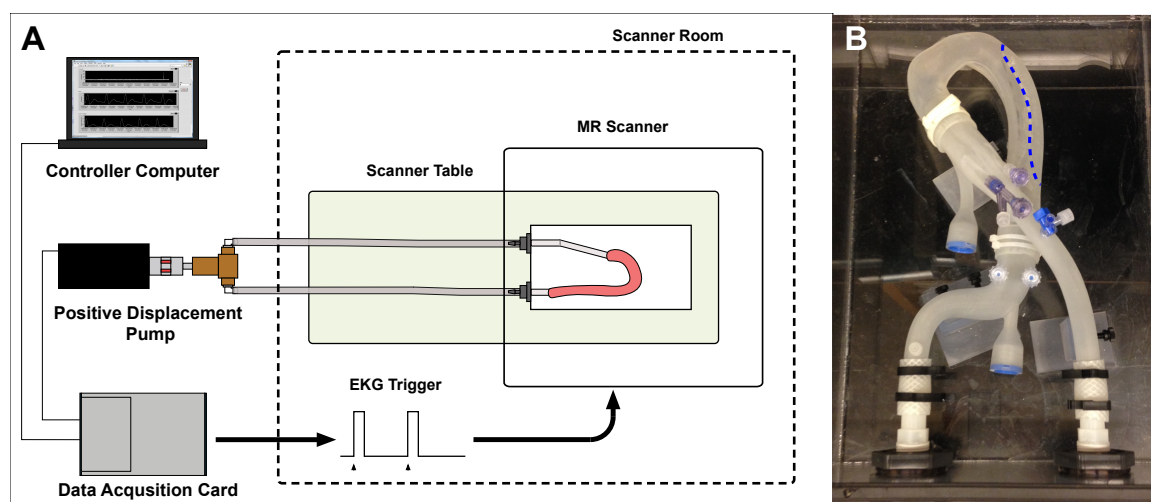
Figure 3.1: Experimental setup for PCMR imaging of aortic dissection model (A). Aortic dissection model (B) with intimal flap outlined (dashed blue)

3.2.2   PCMR Imaging

The magnetic resonance-compatible flow loop was set up in a 3 Tesla Prisma MR scanner (Siemens, Erlangen, Germany), and the model enclosure was filled with water. Tubing was tunneled out to the control room for connection to the pump (Figure 3.1). A trigger signal generated by the pump driver was used to provide EKG-gated image acquisition. Four-dimensional PCMR volumes (3 experiments per model) were acquired with a field of view of 250 x 250 mm and slab thickness of 52 mm, covering
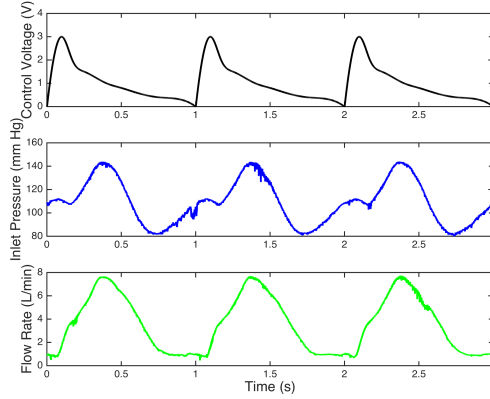
Figure 3.2: Pump driver voltage (top), central aortic pressure (middle), and model outlet flow rate (bottom) traces demonstrating physiologic pumping

the entire volume of the model from ascending aorta to the extent of the thoracic aorta, with in-plane resolution of 1.0 mm and slice thickness of 2.0 mm. A velocity encoding value of 80 cm/s in each direction was used to prevent phase-wrapping and optimize the dynamic range of the phases collected. The flip angle was set to 15°, with an echo time of 4.6 ms and repetition time of 59.2 ms. Fifteen phases were acquired over the cardiac cycle resulting in a cardiac period of approximately 888 ms.

3.2.3   Image processing and analysis

Aortic wall contours were segmented from magnitude images via a region-growing level-set segmentation algorithm using the Medical Imaging Interaction Toolkit (MITK, Heidelberg, Germany). Stereolithography (.stl) files were created from these contours and used to generate point-cloud representations of the aortic lumen. These stereolithography files were also imported into the Vascular Modeling Toolkit (www.vmtk.org) to extract centerlines of the entire aortic lumen. Centerlines, lumen contours, and 4D PCMR volumes were subsequently imported into custom processing software developed in Matlab (Mathworks, Natick, MA).

The segmented aortic contours were used to select data within the aortic lumen (Figure 3.3). Phase offset was calculated in each independent phase direction on a

slice-by-slice basis and corrected. Vectors tangent to each centerline point were calculated to derive planes normal to the aortic wall. Slices through the phase data were extracted at these planes for calculation of through-plane flow rates. In slices through the dissected portion of the aorta, the dissection flap was manually segmented, allowing for quantification of individual luminal flow rates and areas.
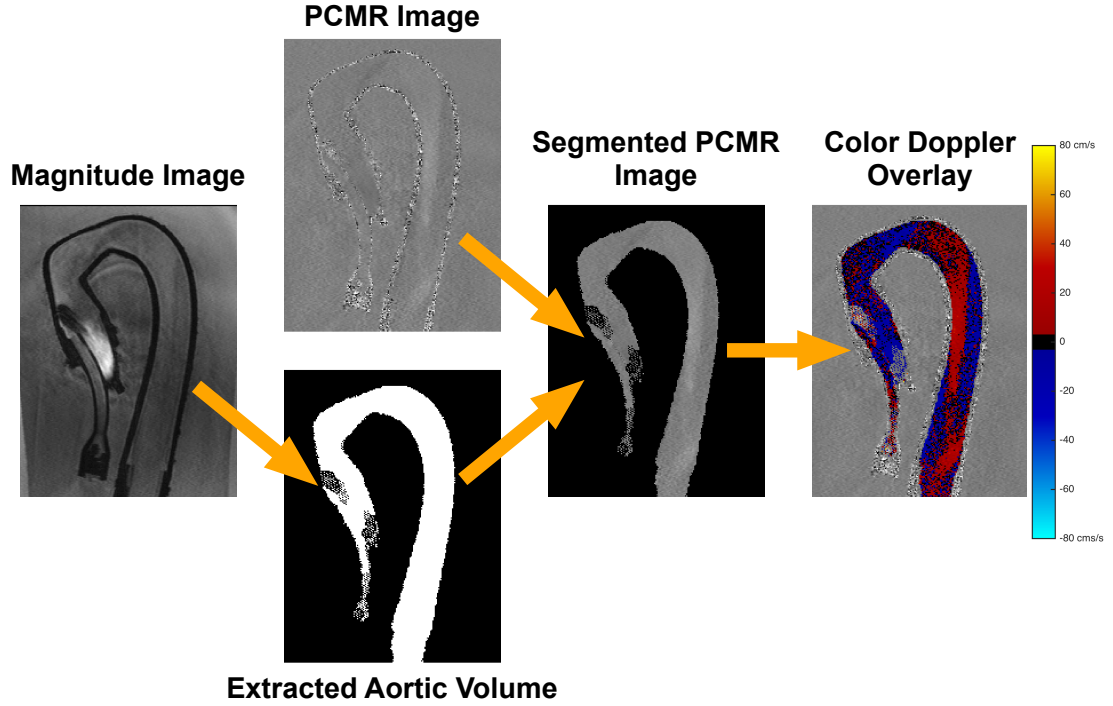
Figure 3.3: Image processing workflow for visualization and hemodynamic calculation. The full volume of the aortic lumen is extracted from the magnitude image, which is then used to segment out velocity data from the aorta alone for processing and visualization

3.2.4 Quantification of geometric and hemodynamic parameters

Geometric parameters were evaluated at 5 slices along the length of the descending aorta. Flap coordinates were parameterized in each slice to generate a spline interpolation in the transverse axis of the intimal flap. Subsequently, a second spline interpolation was performed in the longitudinal direction along the previously interpolated flap points from slice to slice. Flap displacement throughout the cardiac cycle was calculated relative to the initial state (time t = 0) as the Euclidean distance

between interpolated flap points at 15 equally spaced time points during the cardiac cycle.

Velocity profiles in each lumen were integrated across luminal cross-sections to calculate volumetric flow rate at each cardiac phase. Flow reversal was evaluated by calculating the Reverse Flow Index (RFI), defined as

$$\text{RFI} = 100\% \times \frac{\left| \int_0^T Q_{reverse}dt \right|}{\left| \int_0^T Q_{reverse}dt \right| + \left| \int_0^T Q_{forward}dt \right|} \tag{3.1}$$

where $Q_{reverse}$ and $Q_{forward}$ are the summed negative and positive flow rates at a given slice location, respectively, and T is the cardiac period. The RFI quantifies the percentage of blood volume ejected retrograde at a given slice normal to the aortic wall.

3.2.5 Flow visualization

Segmented PCMR image stacks for each direction were imported into ParaView (Kitware, Clifton Park, NY) for flow visualization [155]. Non-zero phase intensities (within the aortic contour) were thresholded and scaled according to the velocity encoding value of 80 cm/s in each phase direction. Velocity vectors were computed by summing unit normal vectors scaled by individual velocity components in the standard Cartesian directions. The resulting velocity vectors were iterated over three cardiac cycles, and slices were selected normal to the aortic wall for particle seeding. Particle paths were calculated across the cardiac cycle, interpolated by a factor of ten in time, and used to visualize flow changes.

3.2.6 Statistical analysis

Data are reported as mean ± standard deviation. The concordance correlation coefficient (CCC) was calculated to assess agreement [156] between measurements. One-way analysis of variance (ANOVA) tests were performed to compare hemodynamic parameters across normal models and true, false, and total dissected lumina at each individual position in the descending aorta. A p-value of 0.05 was set as the level of statistical significance. Pair-wise Tukey-Kramer tests were performed for individual comparisons among groups at each position along the aorta. All statistical analyses were performed in MATLAB (Mathworks, Natick, MA).

3.3 Results

3.3.1 Flow reversal along dissection

While true lumen RFI was similar to that of the normal aorta at varying planes through the dissection, the false lumen RFI was found to be significantly greater than that of normal in the middle of the dissected segment (Figure 3.4). At planes 25% and 50% of the distance between the entry and exit tear, false lumen RFI reached $21.1 \pm 3.8\%$ and $16.8 \pm 4.2\%$, respectively, as compared to RFI of $1.98 \pm 0.44\%$ and $5.0 \pm 1.6\%$ in the normal aorta (P<0.01 in both cases). False lumen RFI ($1.61 \pm 0.62\%$) was significantly lower than that of the normal aorta ($3.47 \pm 0.50\%$, P<0.05) at the level of the exit tear, while the true lumen had a significantly higher RFI ($5.98 \pm 0.55\%$, P<0.01) than that of the normal at this location, which may be a result of mixing between true and false lumen flows at this location. Reversed flow is observed to occur during diastole as the fluid decelerates and the distal false lumen is distended (Figure 3.5).
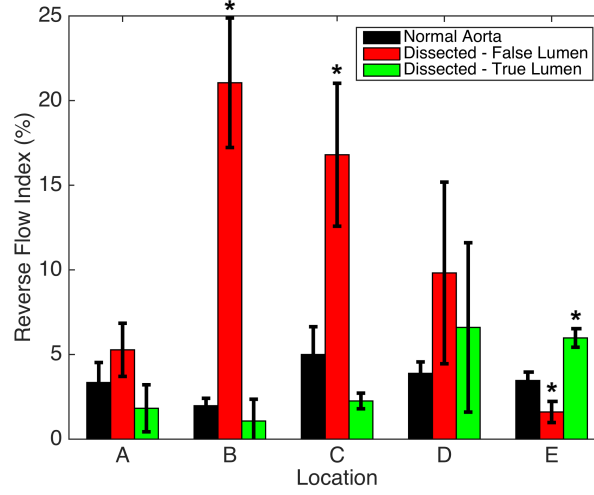
Figure 3.4: Reverse flow index (RFI) calculated in normal and dissected aortic lumina at five points along the descending thoracic aorta (asterisk indicates statistical difference from the normal model, $P<0.05$)

3.3.2 Vortex Formation

A vortex is observed to form in the dissected aorta around the exit tear (Figure 3.6, Supplemental Video 1). During diastole, reversed flows in the distal true lumen are accompanied by forward flow in the false lumen at the exit tear. This may be the result of the mixing of separate streams of varying velocity from each lumen at the exit tear. Shear gradients at such interfaces lead to vortices that evolve with time.

3.3.3 Dynamic flap motion

Though the shape of the intimal flap changed along the extent of the dissection, it mainly assumed a sinusoidal cross-sectional profile (Figure 3.5). Under pulsatile flow conditions, the intimal flap demonstrated large-scale motion over the course of the cardiac cycle. Greatest displacement of the flap was observed at entry and exit tears (Figure 3.7). A maximum displacement of 14.3 ± 0.5 mm, on the order of the aortic radius, was reached near the exit tear at 0.86 ± 0.07 s of the cardiac cycle, corresponding to mid-diastole. At peak systole (0.43 s), the distal portion of the flap near the exit tear remained collapsed onto the false lumen, achieving maximal true
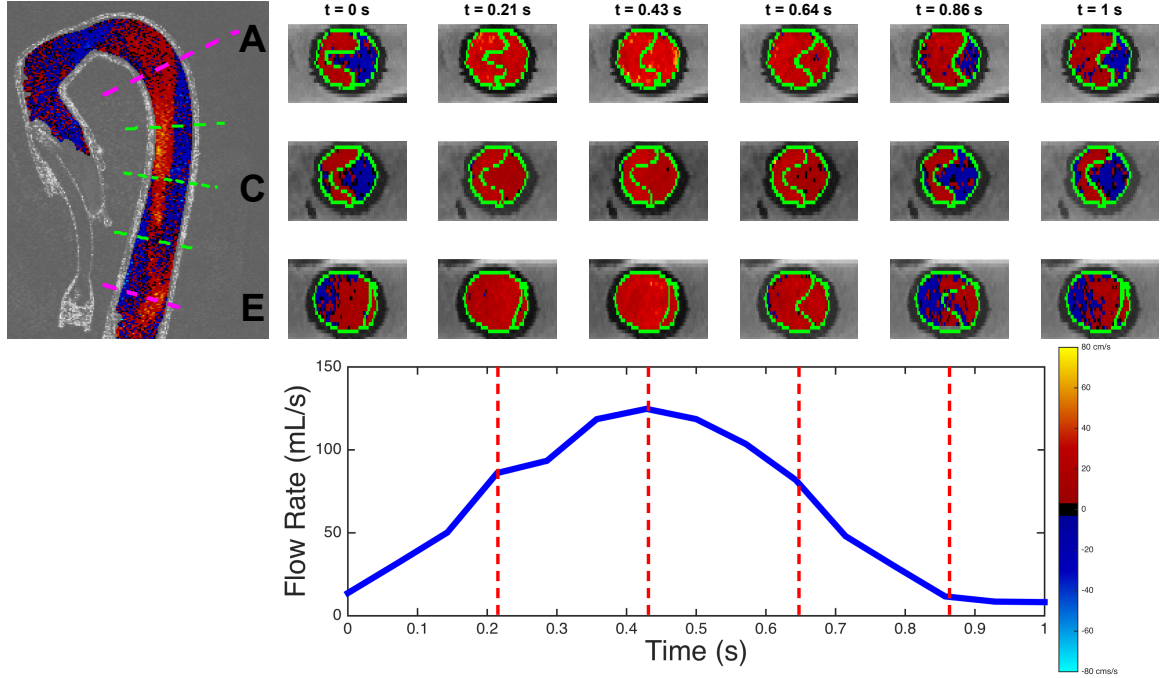
Figure 3.5: Axial slices through the dissection, taken at planes normal to the aortic wall at the level of the entry tear (slice location A), mid-dissection (slice location C), and exit tear (slice location E). Flap motion can be appreciated at all slice locations, but is most accentuated near the exit tear, with flap displacements approaching the aortic radius. Blue indicates retrograde (towards the head) and red antegrade (towards the systemic circulation) flow

lumen distension (Figure 3.5). However, during the deceleration phase and through diastole, the flap moved centrally, leading to a distension of the distal false lumen, up to the exit tear (slice location E), before closing at the end of the cycle. This opening coincided with forward flow in the false lumen near the exit tear, but was delayed in time relative to peak flow more proximally (Figure 3.8). Maximal false lumen distension was reached at 0.71 ± 0.07 s, while false lumen flow peaked at 0.38 ± 0.04 s at the entry tear (P<0.05), 0.43 ± 0.07 s at mid-dissection (P<0.05), and 0.52 ± 0.08 s at the level of the exit tear (P>0.05).

Closure of the distal false lumen may contribute to the reversed flows observed via modulation of the fluid flow resistance in this portion of the dissection. This high-resistance pathway may prevent outflow from the proximal false lumen during systole, leading to premature or increased fluid deceleration, and thus reversed flow.

40
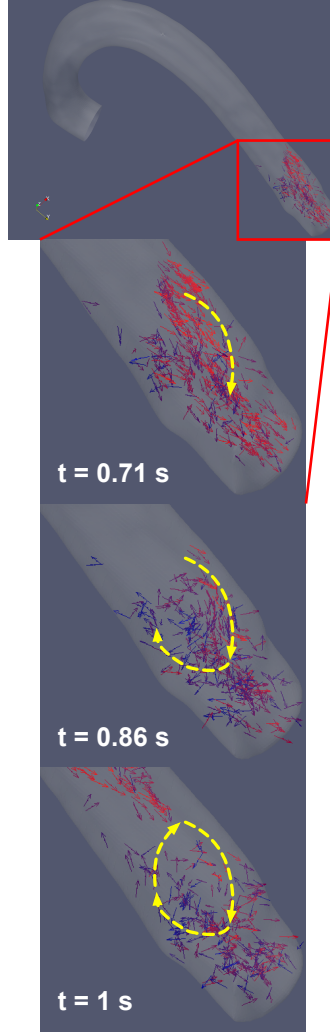
Figure 3.6: Computed flow visualization of MR data documents formation of vortex at exit tear in late diastole. Developing rotational components marked by dotted arrows

3.3.4   Changes to normal aortic velocity profile

Observation of the normal aortic model in the mid-thoracic descending segment revealed a virtually parabolic velocity profile (Figure 3.9) at peak systole. Maximum velocities reached 26.5 ± 2.9 cm/s at 0.45 ± 0.08 s into the cardiac cycle, with minimum velocities of -5.1 $\pm$ 1.3 cm/s reached at 0.93 ± 0.07 s. The peak of this profile diminished through the deceleration phase to the end of diastole. A small region of reversed flow was observed along the medial wall of the vessel in late diastole. This slight reversal of velocities near the wall is a consequence of the pulsatile aortic flow,
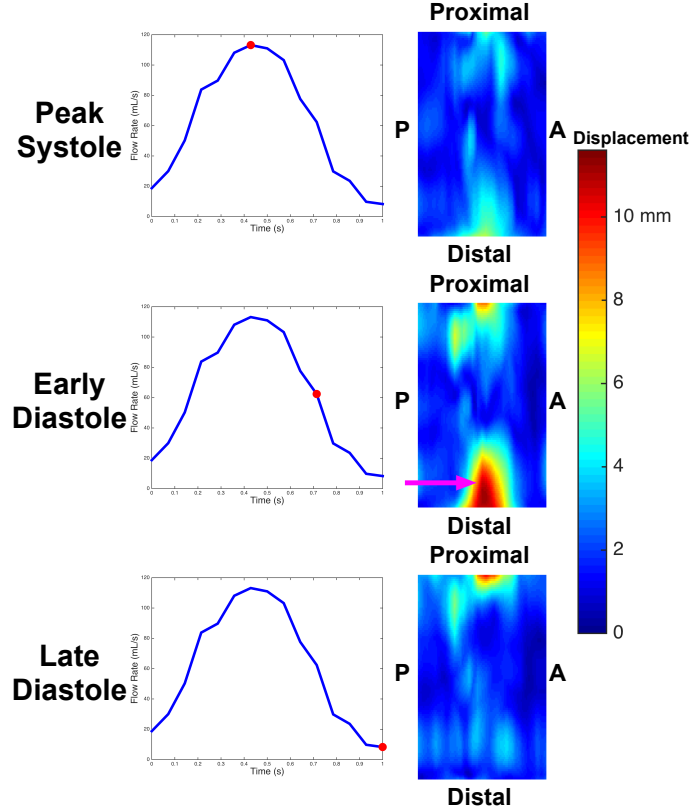
Figure 3.7: Transverse motion of the intimal flap at different points in the cardiac cycle. Note accentuated motion of the intimal flap at the level of the exit tear (arrow) during fluid deceleration

as predicted by Womersley [157]. The aortic curvature skews the velocity profile laterally, yielding lesser fluid momentum along the medial wall subject to changes in pressure gradient, leading to marginally reversed flow in this region.

Conversely, the velocity in the dissected aortic model consistently exhibited an eccentric profile. Accelerated flows were seen in the compressed true lumen, with peak velocities in the mid-dissection plane of 33.9 ± 4.4 cm/s located at the medial wall occurring at 0.43 ± 0 s, corresponding to peak systole, above. At this point in time, the well-demarcated false lumen possessed a more parabolic velocity profile, peaking at a velocity of 21.7 ± 1.6 cm/s. However, as the fluid decelerated, the false lumen fluid began to reverse, reaching complete luminal reversal, with a minimum velocity of -9.2 ± 1.1 cm/s by the end of diastole (0.90 ± 0.04 s), coinciding with maximal
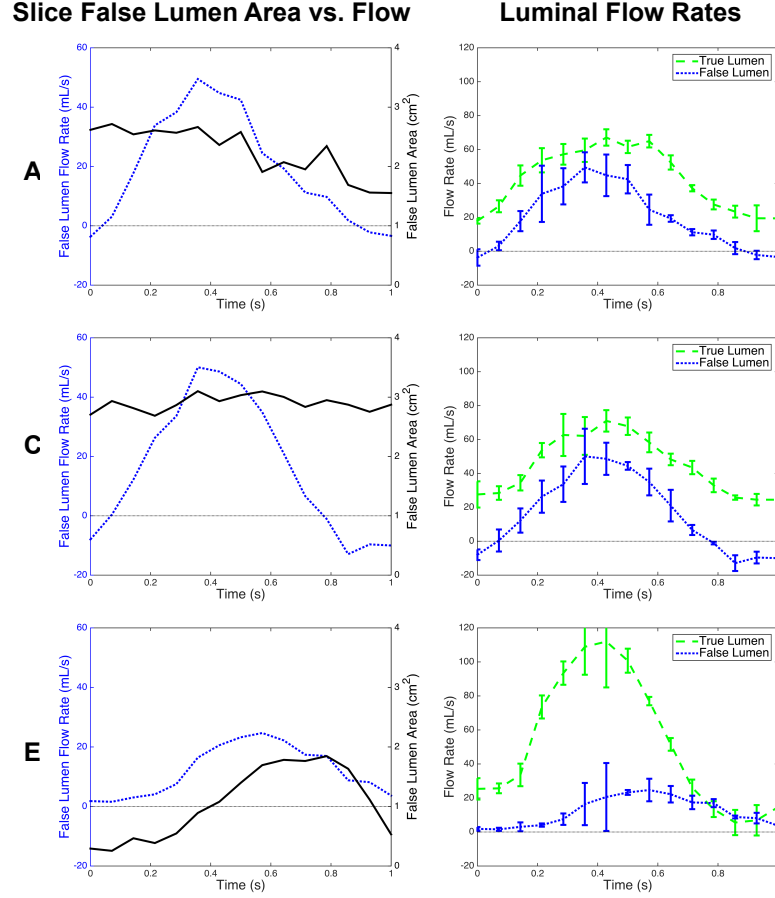
Figure 3.8: False lumen cross-sectional area at exit tear site and corresponding false lumen flow rates (left) and flow division between true and false lumen (right) along the extent of the dissection. Slice locations (A,C,E) correspond to those designated in Figure 3.5. Note forward flow in the false lumen in the proximal and middle dissection as the false lumen is collapsed near the exit tear (area approaches 0) during systole. The false lumen distends during diastole

false lumen distension along the exit tear. Collectively, these observations suggest a pumping-like action of flow in the false lumen (i.e. forward flow during systole, reversed flow at end-diastole). Fluid velocities remained positive and antegrade in the true lumen throughout the cardiac cycle, though a minimum velocity of -4.3 $\pm$ 2.3 cm/s was observed at a point of 0.83 $\pm$ 0.04 s within the cardiac period of 1 s.

Flow visualization in both normal and dissected aorta models revealed helical flows developing along the ascending aorta through the aortic arch (Figure 3.10), as seen physiologically [121]. These complex flows can be appreciated in reconstructed

43
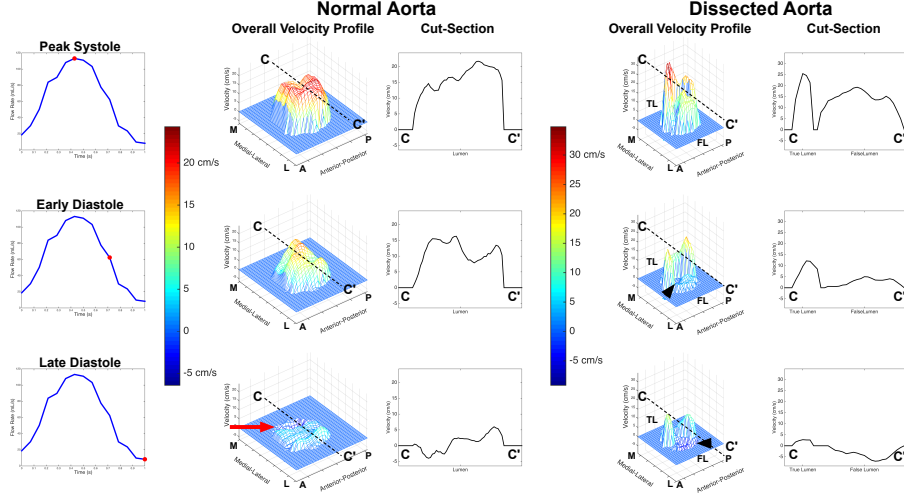
Figure 3.9: Three-dimensional velocity plots in the mid-thoracic descending aorta seen throughout the cardiac cycle. Two-dimensional velocity profiles are taken through the midline of the aortic cross-section along mediolateral cut plane C-C'. Reversed flow, a consequence of normal pulsatile flow, can be observed along the medial wall of the Normal aorta in late diastole (red arrow). Pathologic reversed flows in the Dissected aorta can be seen originating in the false lumen during the deceleration phase of the cardiac cycle, with fully reversed flow in the false lumen by end diastole (black arrowheads)

fluid motion (Supplemental Video 1).

3.3.5 Flow division and conservation

Overall flow rates were comparable between normal and dissected aortic models (Figure 3.11). In the descending aorta, flow rates of 4.0 ± 0.2 L/min and 3.8 ± 0.1 L/min were seen in the normal and dissected models, respectively (P>0.05 in comparisons at each slice location). These corresponded to calculated flow rates at model inlet of 4.2 ± 0.3 L/min and 4.1 ± 0.1 L/min (P=0.64) in the normal and dissected models, respectively. However, the flow was divided unequally among true and false lumina, with average flow rates of 2.9 ± 0.3 L/min in the true lumen and 1.0 ± 0.2 L/min in the false (P<0.001 in comparisons at each slice location), corresponding to a mean flow division of 74% to the true lumen with 26% to the false, which was consistent along the length of the dissection (P>0.05 in comparisons between slice locations). While flows peaked in both true and false lumen at 0.44 s in the middle of the dis-

44
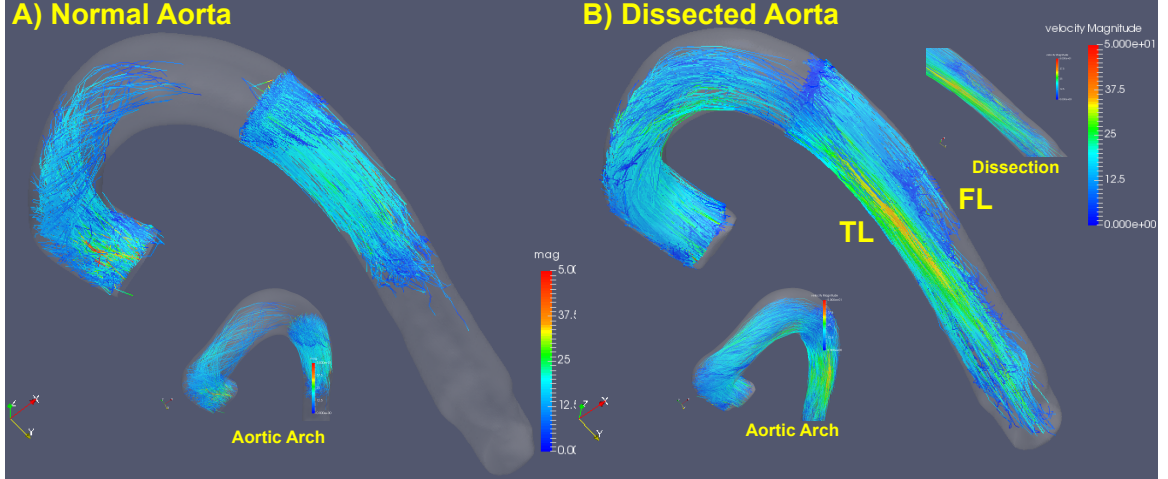
Figure 3.10: Pathline visualizations in both normal and dissected aortae. Physiological, helical flows can be noted throughout the aortic arch in both models, with significant skewing of velocity profile towards true lumen in the dissected case. Note filling of distal true lumen with cessation of flow partway down the false lumen

sected segment (Figure 3.8), their peak flow rates were significantly different (true lumen: 81 ± 18 mL/s, false lumen: 43 ± 11 mL/s, P<0.05).

3.3.6   Model reproducibility

Three imaging experiments were performed on the normal and dissected models. The pulsatile pump generated robust, consistent pressure (CCC = 0.94 ± 0.06) and flow (CCC = 0.91 ± 0.02) waveforms throughout experiments. Furthermore, flow rates calculated from PCMR data matched those of the flow meter used in the experimental setup (CCC = 0.96 ± 0.01), validating the flow quantification performed. Finally, calculated flow rates exhibited strong agreement across experiments (CCC = 0.98 ± 0.01, measured at ascending aorta) and all slice locations (Figure 3.11) along the aorta (CCC = 0.94 ± 0.01).
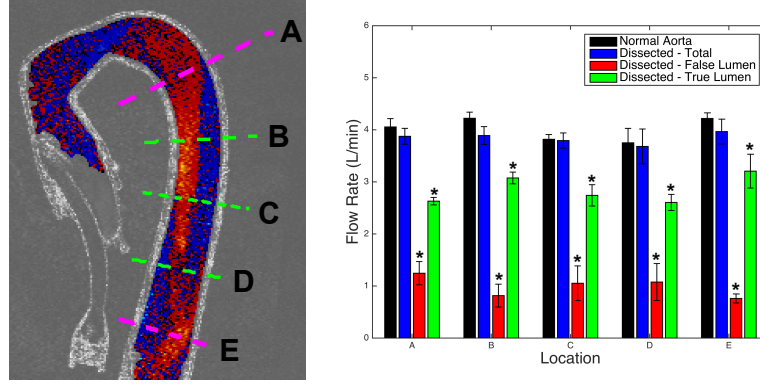
Figure 3.11: Luminal flow rates in normal (black) and dissected (colored) aorta. Slice locations on right correspond to slices designated on left (asterisks indicate significant difference from the Normal aorta at all slices, P<0.05)

3.4   Discussion

3.4.1   Hemodynamic alterations in dissected aorta

Disruptions to normal pulsatile aortic flow patterns, including flow reversal, luminal pumping, and vortex formation, were discovered in our compliant, anatomic model of aortic dissection, supporting our initial hypothesis. Significant flow reversal was demonstrated in the proximal false lumen of the dissected aorta when compared to normal controls, as quantified by RFI. Though retrograde flows have been reported in previous clinical studies of dissection [118, 132, 158], this phenomenon has not been demonstrated in the laboratory. Reverse flow indices of 20% seen in these regions may account for substantial inefficiency in forward transport of blood through the false lumen.

Pumping action of the false lumen is suspected to account for the observed flow reversal, as undulating motion of the intimal flap coincides with changes in false lumen flow. This action may force fluid retrograde, such that it reverses in the proximal segment by the end of the cycle. Furthermore, the closing motion of the distal flap may actively decrease the momentum of the blood in the mid-dissection segment, contributing to the observed flow reversal.

46

3.4.2 Implications of altered hemodynamics

Clinically, the reversed flow burden demonstrated in this study may contribute to pathological vascular remodeling leading to false lumen aneurysm formation, and may ultimately be both a prognostic marker and indication for more aggressive or earlier intervention. In humans, the diseased and weakened aortic wall of the false lumen may be more susceptible to aneurysmal degeneration than that of the true lumen. Earlier intervention in patients with uncomplicated Type B dissection who eventually develop dilatation of the aorta may prevent aneurysm formation. Thus initial identification of those most at risk of dilating is critical in optimizing treatment at index admission.

As these luminal streams of different velocity rejoin at the exit tear, a shear, or mixing, layer is formed. Velocity discontinuities at the interface lead to the formation of small, local, vortices. These mixing vortices may induce significant drag and stall, leading to decreased fluid energy and blood transport as a result. Clinically, this may exacerbate endothelial dysfunction promoted by reversed flow and may also contribute to deficient perfusion pressure distally.

3.4.3 Clinical utility of functional flow imaging

Whereas the workup of dissection has traditionally relied on structural imaging, we suggest the need for functional flow imaging in the assessment of these patients. Both MRI [118, 132] and transesophageal echocardiography (TEE) [158] can be used in an EKG-gated fashion to assess pulsatile aortic fluid mechanics. These modalities can be used to quantify flow reversal throughout the dissected aorta, which may prove a useful prognostic indicator. In addition, the identification of vortical structures with either modality may be used in the localization of tears in the intimal flap. These foci may be important landmarks requiring graft coverage to ensure complete false lumen obliteration.

3.4.4 Model validity and utility

As expected, flow rates were conserved in the dissection across true and false lumen, and along the longitudinal extent of the aorta. Though overall flow is maintained, the flow division across the intimal flap indicates significant loss, approximately 25%, to the false lumen with diminished branch vessel perfusion maintained by the true lumen. This perfusion deficiency may itself be an indication for stent-grafting.

We present an experimental model and processing framework for an elastic model of aortic dissection. The custom-built software allows for hemodynamic calculations of flow rates and flow reversal, via the RFI, in a reproducible fashion. These phenomena have not been studied in previous computational and experimental studies of rigid aortic dissection. In addition, this model allows for validation of calculated flow rates against those measured by flow meter, a feature unavailable in human studies employing 4D PCMR. Finally, these results demonstrate the need to make use of mobile flaps and pulsatile flow conditions for future modeling of dissection. These features contribute significantly to the fluid mechanics observed, which may be critical to understanding of the pathophysiology.

3.4.5 Limitations

Despite these novel findings, there are some limitations to this work. First, the aortic models used did not contain any branch vessels, namely the cephalic vessels originating from the aortic arch. In human physiology, these low-resistance vessels siphon off blood from the aorta to supply the high oxygen demands of the head, neck, and upper extremity. Therefore, these vessels may act as a sump for blood, especially during diastole, which would further accentuate the false lumen flow reversal observed in this study.

Furthermore, due to limitations of the pulsatile pump used, water, with a density of 1000 kg/m^3 and dynamic viscosity of 0.74 cP, was used as our working fluid as

opposed to blood, which possesses a density of 1060 kg/m^3 and dynamic viscosity of 3.5 cP. However, the Reynolds number was calculated to be in the laminar range of blood flow in the human aorta, and no transitions to turbulence were observed in the model. The Womersley number calculated for the fluid was in a range similar to that of human aorta, and the relevant effects of pulsatile flow on velocity profiles were observed as predicted.

3.5   Conclusions

In conclusion, we present an in vitro methodology and processing workflow to experimentally investigate the hemodynamics of the native and dissected aorta. With this work, we present physiologic flow in a normal aortic model that is contrasted with abnormal, reversed flow in a model of the dissected aorta. Vortex identification of tears and general flap motion are appreciated in the model. These differences may represent hemodynamic changes with pathologic consequences in human dissection. Future study of aortic dissection using this experimental setup may improve early, targeted selection of patients for endovascular intervention and may inform upon device design and deployment.

CHAPTER 4

INTERMEDIATE FENESTRATIONS RELIEVE FLOW REVERSAL IN A SILICONE MODEL OF STANFORD TYPE B AORTIC DISSECTION

4.1 Introduction

4.1.1 Current methods of management

Beta-blocker therapy remains the foundation of treatment for patients with aortic dissection [23]. Such treatment is aimed at decreasing the aortic impulse via vasodilatory, antihypertensive, and negative inotropic effects, and in so doing, decreasing the shear stresses on the aortic wall. While pressure control is considered a central goal for beta-blocker therapy, its effects on fluid flow patterns, and thus the overall hemodynamics, of the aorta remain unclear.

Endovascular intervention remains a useful modality in the treatment of uncomplicated Type B dissection, but has not been shown to be superior to medical management with beta blockers. Results from the INSTEAD trial, and its extension INSTEAD-XL, suggest that patients undergoing stent-graft intervention may have higher survival and event-free rates at 5 years following index evaluation [44, 45]. While these studies are not definitive, they demonstrate a significant difference in aortic dilatation between study groups, suggesting the role of stent-grafting in restoring normal aortic caliber and providing more favorable remodeling of the aorta. However, it is yet unclear why certain patients remain stable on medical therapy alone, while some patients undergoing endovascular intervention develop aneurysm in the long-term.

4.1.2 Anatomic heterogeneity and outcomes in aortic dissection

Part of the variability in outcomes among these patients is thought to result from variations in both dissection anatomy and hemodynamics [50, 56]. In addition, interactions between these two variables may account for unique conditions that favor aneurysmal degeneration. Thrombosis in the false lumen has been a factor of particular interest, with some studies touting the benefits of false lumen thrombosis, whether or not complete [47, 59, 61, 62], and others finding patients with partial thrombosis faring worse than those with a completely patent false lumen [46]. Though these studies may be flawed in their assessment of overall thrombosis, this discordance demonstrates that anatomy may only partially explain the variability in outcomes. Aortic function, as indicated by local hemodynamics, is posited to be a useful prognostic indicator [99, 159–161].

Saccular false lumen anatomy, as well as entry tear size greater than 10 mm and an entry located proximally along the descending aorta, were all found to be predictors of poorer outcomes [56, 139, 140, 162]. Alternatively, circular, non-elliptical true lumen cross-section and the presence of multiple tears, have been associated with better patient outcomes [139, 140]. These anatomic features are thought to lead to an accumulation of hydrostatic pressure within the false lumen, causing gradual distension and degeneration of the aortic wall.

4.1.3 Objectives and hypothesis

In order to understand the role of varying tear configurations on dissection hemodynamics, we employed a silicone model of the aorta with a mobile intimal flap subjected to physiologic flow conditions. Using 4-dimensional phase contrast magnetic resonance (4D PCMR) imaging, we obtained full flow fields throughout the aorta for quantification. We hypothesize that models with three and four tears will exhibit less flow reversal and more efficient forward transport of blood than those with two tears

alone, as the new fenestrations will allow for more low-resistance pathways for blood flow when luminal pumping is present. Further, we hypothesize that increased mean arterial pressure (MAP) will leave flow patterns unchanged as compared to normal MAP.

4.2 Methods

Mock circulation and imaging techniques were assembled and performed as described previously (Section 3.2.1). Briefly:

4.2.1 Flow loop and imaging setup

Silicone models of descending aortic dissection with a mobile intimal flap were fabricated, and entry and exit tears were incised at prescribed locations (Section 2.2.1). Additional fenestrations were subsequently added at locations 50% and 75% of the distance from entry to exit tear, affording models with two, three, and four tears (Figure 4.1). These models were installed in a flow loop and subjected to physiologic flow (4 L/min). Pressures were varied between normal (140/80 mm Hg), hypertensive (180/120 mm Hg) and extreme hypertensive (220/160 mm Hg) conditions in order to mimic pressure differences observed in patients before and after initiation of beta-blocker therapy.

During flow, EKG-gated MR image volumes were acquired using a 3 Tesla Prisma scanner (Siemens, Erlangen, Germany). Four-dimensional PCMR slabs were acquired across a field of view of 250 x 250 mm with 26 slices at a voxel size of 1.0 x 1.0 x 2.0 mm, totaling a depth of 52 mm. A velocity-encoding value of 80 cm/s in each Cartesian direction was selected to eliminate phase-wrap artifact and maximize dynamic range.
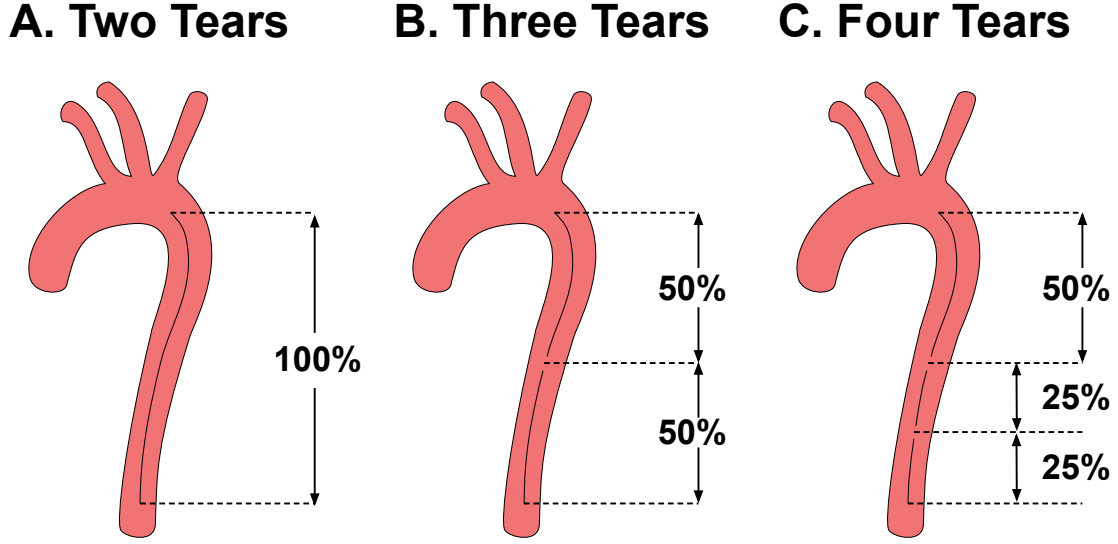
Figure 4.1: Varying dissection geometries tested with entry and exit tear only (**A**), entry, exit, and 50% flap length fenestration (**B**), and entry, exit, 50% and 75% flap length fenestrations (**C**)

4.2.2   Image processing

Magnitude images were segmented semi-automatically using a level-set algorithm (MITK, Heidelberg, Germany) in order to derive lumen contours. In addition, the segmentations were used to generate volumes for computation of aortic centerlines via the Vascular Modeling Toolkit (www.vmtk.org). Segmentations, centerlines, and PCMR data were imported into custom software for phase offset correction quantification of hemodynamics (Section 3.2.3).

4.2.3   Quantification of intimal flap dynamics

Planes at the levels of entry and exit tears, as well as at distances of 25%, 50% and 75% between the two, were interrogated. The intimal flap was segmented manually throughout the cardiac using the PCMR magnitude data. Coordinates along the flap were interpolated in each slice in order to ensure consistent numbers of points at each cardiac phase. A second spatial interpolation was performed between slices at each flap point. Thus, a constant number of points was obtained for comparison in both

longitudinal and transverse spatial directions. Flap displacement was calculated as the Euclidean distance between a point on the flap at a given phase and its initial position ($t = 0$).

4.2.4   Calculation of hemodynamic parameters

Individual velocity profiles were acquired for both true and false lumen. Flow rate in each lumen was calculated by integrating the through-plane velocity at a given slice across the luminal cross-section. In-plane pixel area was corrected for the angle of the plane in absolute coordinates. Relative retrograde flow over the course of the cardiac cycle was determined by calculating the reverse flow index (Section 3.2.4, Equation 3.1).

4.2.5   Flow visualization

Following segmentation, PCMR data was visualized in ParaView (Kitware, Clifton Park, NY) [155]. Velocities were interpolated in time and used to generate particle paths, which were subsequently contoured for gross visualization of flow patterns. Counts of particles passing through planes drawn at entry and exit tear were used to calculate efficiency of blood convection.

4.2.6   Statistical analysis

Statistical analyses were performed using MATLAB (Mathworks, Natick, MA), with a p-value of 0.05 set as the level of significance. Continuous data are reported as mean $\pm$ standard deviation. Two-way analysis of variance (ANOVA) tests were performed at each slice in order to determine overall differences between both pressure and tear-configurations. Individual one-way ANOVA tests were performed at each slice with data in opposing conditions stratified, i.e. ANOVA between tear configuration groups were performed at each pressure configuration and vice-versa. Post-hoc analysis of

individual comparisons was performed with pair-wise Tukey-Kramer tests.

4.3 Results

4.3.1 Vortices localized to exit tears

As reported previously (Section 3.3.2), vortical structures were seen to form at the location of the exit tear in all models, presumably the result of mixing of streams of varying velocity from each lumen. Additionally, with the introduction of intermediate fenestrations, additional vortices were observed to form at these sites (Figure 4.2). As with those seen in the distal dissection, the intermediate vortices may be the result of interaction between fluid streams of differing velocities at these locations. It should be noted that all of the vortices observed are right-handed with respect to the image stack anterior-posterior axis (Figure 4.3), suggesting a relative true lumen pressure defect.

4.3.2 Fenestrations relieve flow reversal

Fenestrations were found to reduce flow reversal as quantified by the reverse flow index (Equation 3.1) when compared to dissection without intermediate tears, most notably in the proximal false lumen (Figure 4.4D). These results held when RFI calculations were aggregated across pressure conditions (Table 4.1). The prominent flow reversal in the proximal and mid-dissection false lumen of the two tear dissection (19.2 ± 3.3%, 17.5 ± 5.7%, respectively) was significantly reduced in the three tear (4.67 ± 1.5%, 7.05 ± 0.40%, P<0.001) and four tear dissections (4.87 ± 1.7%, 7.45 ± 2.1%, P<0.001).
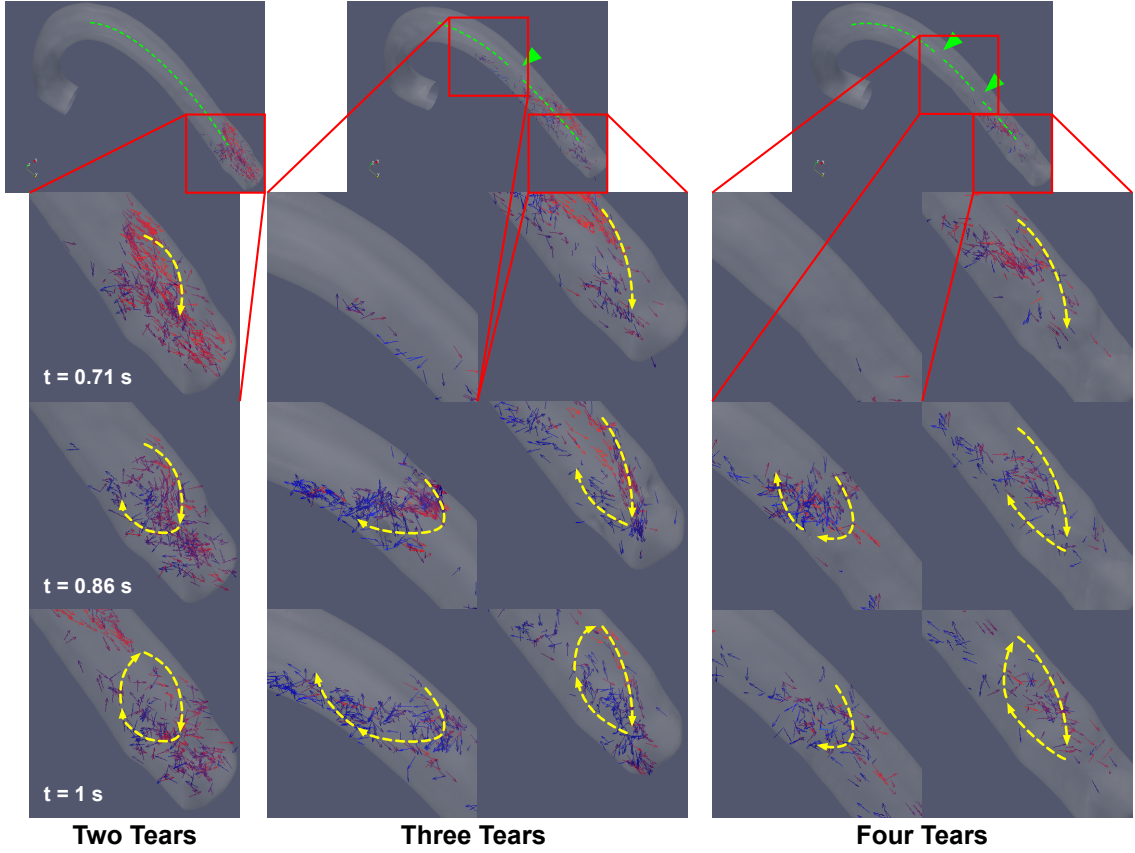
Figure 4.2: Evolution of diastolic vortices at tear sites in dissections with varying number of tears (yellow dashed arrows). Intimal flap is outlined in green dashed line, intermediate fenestrations denoted by green arrowheads

4.3.3   Transluminal fluid shift

Upon computed visualization, fluid was observed to traverse from false to true lumen in the locale of the intermediate fenestrations. This was noted in the change in distribution of flow between true and false lumen along the length of the dissection (Figure 4.5). While relative true and false lumen flow rates remained constant along dissection with entry and exit tears only, the introduction of intermediate fenestrations is seen to lead to an increase in relative true lumen flow rate longitudinally. As mass flow rate must be conserved, in the absence of any branch vessels, any change in relative flow rates must occur as a result of transfer of fluid from one lumen to the other. This transluminal fluid shift is also suggested by the vortices described
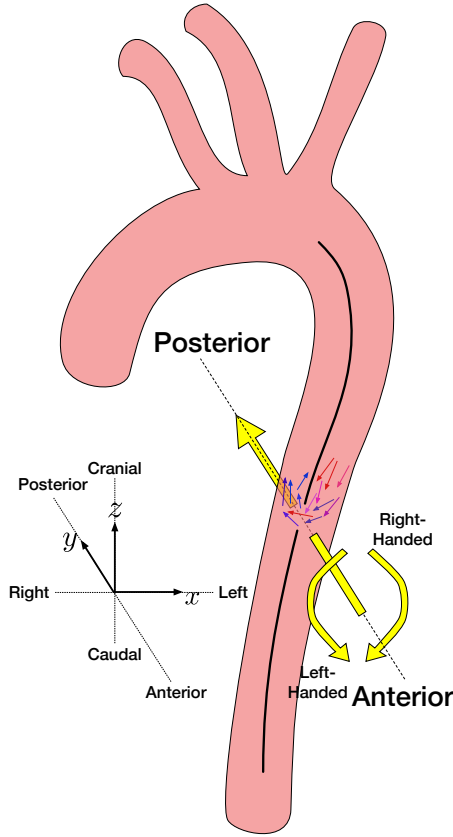
Figure 4.3: Right-handed convention for describing vortices, with positive (right-handed) rotational components rotating about anterior-posterior axis

previously (Section 4.3.1), which likely arise from the interaction of two distinct fluid streams.

4.3.4   Recapitulation of flap motion and flow velocities

As with the two-tear dissection, significant motion of the intimal flap was noted in models with further fenestrations. Similarly accentuated motion was notable at the most distal exit tear, with excursions of 14.9 ± 2.0 mm and 13.8 ± 3.8 mm at times of 0.59 ± 0.07 s and 0.66 ± 0.07 s during the cardiac period for three- and four-tear models, respectively. This action was conserved in smaller sections in which the most eccentric motion of the intimal flap was seen to occur at tear sites distal to the entry
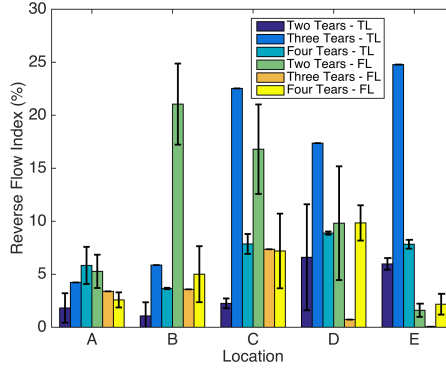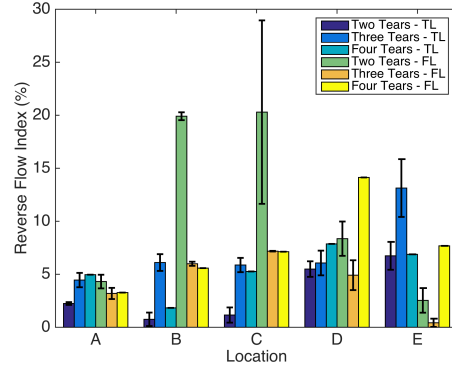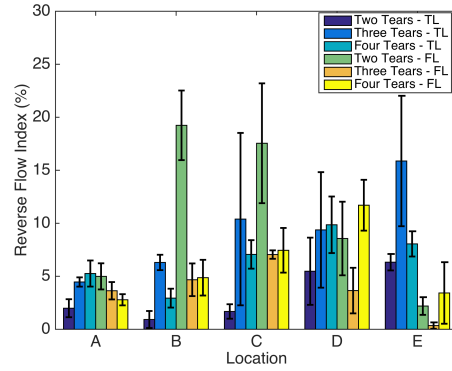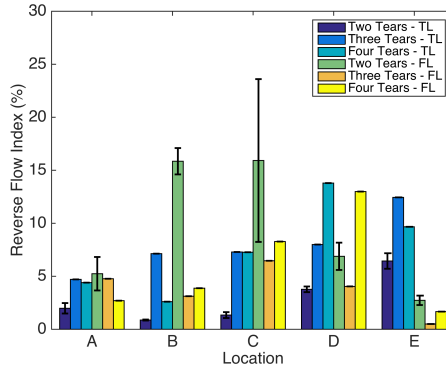
Figure 4.4: Differences in RFI calculated across varying tear configurations at normal (**A**), hypertensive (**B**), and extreme hypertensive (**C**) pressure conditions, as well as aggregated across pressure settings (**D**)

tear. At half the distance between entry and exit tear, maximal flap excursions of 13.7 ± 2.2 mm and 9.92 ± 2.5 mm at times of 0.52 ± 0.12 s and 0.54 ± 0.09 s for three- and four-tear models, respectively. In the four tear model, a maximum excursion of 12.4 ± 3.8 mm occurred at 0.64 ± 0.10 s in the cardiac cycle at the tear located 75% of the distance between entry and exit tears.

The distal false lumen was found to be collapsed during peak systole in the fenestrated case, as with the two-tear case. This preserved behavior may be due to the relative narrowing of the false lumen at this location, leading to accelerated velocities. In systole, as these velocities increase to maximum, the relative pressure along these streamlines decreases, which may lead to a Venturi effect, drawing in the flap to the wall of the outer aortic curvature. This approximation of the flap to the aortic

Table 4.1: Reverse flow index calculated across varying dissection anatomies

Location	Two Tears		Three Tears		Four Tears	
	True	False	True	False	True	False
Entry	1.99	4.99	4.46	3.64	5.26	2.79
25%	0.924	19.2	6.31	4.67	2.94	4.87
50%	1.68	17.5	10.4	7.05	7.06	7.45
75%	5.48	8.56	9.38	3.65	9.59	11.7
Exit	6.33	2.19	15.9	0.350	8.06	3.43
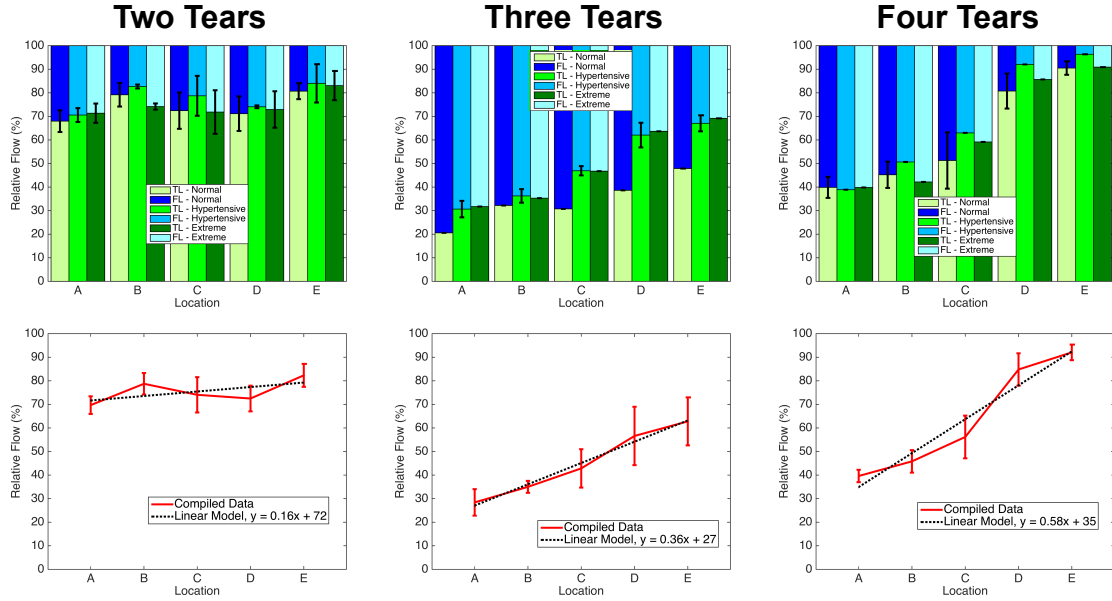
Figure 4.5: Increase in relative true lumen flow along length of dissection in the presence of fenestrations. Note no change in relative flows when no intermediate fenestrations are present

wall was observed at the most distal tear only, with patent false lumen found more proximally. Maximum velocities in both true and false lumen were consistent across varying tear configurations (Table 4.2).

4.3.5 Variations with pressure

While the fluid flow was found to vary with tear anatomy, with a given tear configuration, the fluid mechanics were conserved across varying pressure conditions (Figure

Table 4.2: Maximum true and false lumen velocities show consistency despite variations to number and location of intermediate tears. All units in cm/s

Location	Two Tears		Three Tears		Four Tears	
	True	False	True	False	True	False
Entry	22.5±2.3	3.18±2.0	15.6±5.7	3.67±2.5	19.5±5.1	4.52±3.2
25%	37.5±6.4	4.43±3.8	32.8±4.6	7.50±1.4	34.4±2.5	5.01±3.9
50%	40.4±8.5	5.17±3.9	32.6±5.4	4.7±1.4	31.0±6.3	6.10±1.7
75%	36.4±5.1	2.73±2.7	29.0±3.7	4.70±1.2	39.1±12	7.05±3.2
Exit	30.4±3.0	2.84±2.9	28.1±3.9	4.49±4.4	29.8±2.4	4.05±2.0

Table 4.3: P-values for one-way analysis of variance testing of true lumen flow rates (Q_T) and splits $\left(\dfrac{Q_T}{Q_{tot}}\right)$ for varying pressure conditions

Location	Two Tears		Three Tears		Four Tears	
	Q_T	$\dfrac{Q_T}{Q_{tot}}$	Q_T	$\dfrac{Q_T}{Q_{tot}}$	Q_T	$\dfrac{Q_T}{Q_{tot}}$
Entry	0.550	0.658	0.277	0.359	0.990	0.983
25%	0.0182	0.173	0.482	0.653	0.765	0.675
50%	0.526	0.670	0.243	0.140	0.818	0.762
75%	0.610	0.883	0.202	0.244	0.502	0.625
Exit	0.989	0.803	0.240	0.193	0.00731	0.498

4.6). Statistical analysis of both flow splits and RFI showed no significance differences across pressure conditions for a given tear configuration (Tables 4.3 and 4.4 respectively), save for a few individual cases (P<0.05).

4.4 Discussion

4.4.1 Fenestrations relieve flow reversal, allow for fluid shift

As hypothesized, the introduction of fenestrations between entry and exit tear leads to an overall reduction in flow reversal in both true and false lumen. The fenestrations appear to act as a low-resistance pathway for fluid flow, demonstrated by the lateral
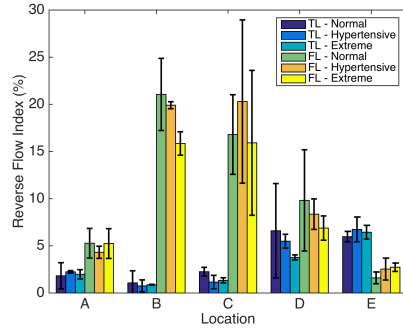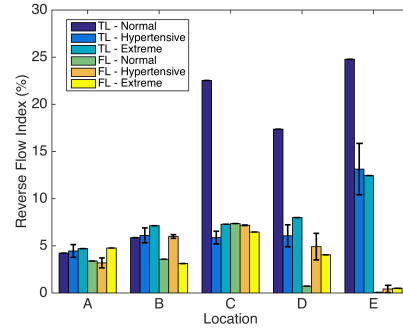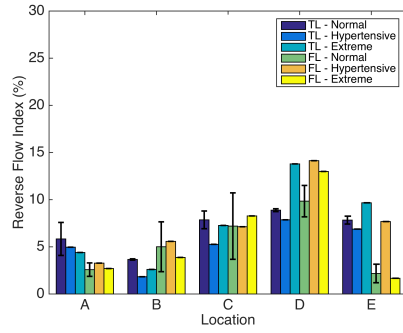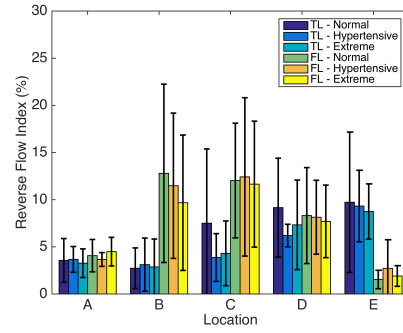
Figure 4.6: Differences in RFI calculated across varying pressure conditions in dissections with two tears (**A**), three tears (**B**), four tears (**C**), and aggregated amongst all tear configurations (**D**)

Table 4.4: P-values for one-way analysis of variance testing of true and false lumen reverse flow index for varying pressure conditions

Location	Two Tears		Three Tears		Four Tears	
	True	False	True	False	True	False
Entry	0.906	0.737	0.895	0.371	0.820	0.779
25%	0.934	0.229	0.630	0.0732	0.0437	0.906
50%	0.133	0.783	0.0478	0.0444	0.403	0.965
75%	0.707	0.732	0.123	0.378	0.0325	0.401
Exit	0.634	0.310	0.256	0.746	0.203	0.195

fluid velocities and changes in luminal flow rates seen longitudinally along the dissection. The lateral fluid shifts across the intimal flap indicate the presence of small, localized pressure gradients developing between true and false lumen. In the absence of intermediate fenestrations, i.e. the two-tear configuration, any pumping action of the false lumen expels fluid retrograde as it has no other path to follow. The flow reversal seen may lead to oscillatory shear and thus endothelial dysfunction, but it may also be indicative of stagnant or recirculating flow, which could lead to false lumen thrombosis. Thus further investigation is necessary to determine the prognosis associated with the flow changes observed. It is predicted, however, that due to the absence of retrograde flow, false lumen in highly fenestrated dissections is less likely to thrombose, portending a poorer outcome for patients.

In addition, the convective efficiency of the blood, as measured by the percentage of traced particles exiting after entering the dissection, decreased with increased fenestrations. This phenomenon may be due to vortices resulting from impingement of lateral fluid jets upon longitudinal streams, or a general conversion of axial flow to secondary flows. Further study is warranted to explain these changes. Clinically, this loss of efficiency may lead to ischemic symptoms as a result of decreased perfusion pressure and delivered blood to end-organs. In addition, decreases in the efficiency of blood transport may induce stresses on the heart as a result of increased afterload. Thus, dissection of the descending aorta may not be a solely vascular disease, but rather have long-term consequences for the patient's overall cardiac health.

Ultimately, the anatomy of aortic dissection, in particular the configuration of intimal flap tears, is seen to influence the hemodynamic changes seen with this condition. Small changes in the intimal flap may significantly alter the fluid flow and cardiac efficiency, and portend differences in outcomes, as reported clinically [61, 62, 139, 140].

4.4.2   Mean arterial pressure does not influence fluid flow

While pressure control is a cornerstone of the management of patients with aortic dissection, it does not appear to have an effect on flow patterns in the vessel, as per the initial hypothesis. This is corroborated by fluid mechanics theory, which suggests that fluid flow is driven by spatial gradients in pressure, such as those that exist between the heart and systemic vasculature, as opposed to absolute pressure or temporal pressure gradients [85, 86]. It is important to note that only small pressure gradients on the order of a few millimeters of mercury are required to drive blood flow in the body. Thus, we may consider pressure at a fixed location, such as a standard blood pressure reading, to be decoupled from flow rate and other flow phenomena. This eases requirements for experimental study, as a single pressure regime may be used. However, it indicates that pressure is indeed a poor surrogate for complex flow phenomena and cannot fully explain variations in fluid flow.

Alternatively, pressure may play a role in the solid mechanics of the aorta, as increased pressure increases vascular wall tension (See Section 1.2.2). While this tension may be mitigated to an extent by the compliance of the vessel, severe, cyclical pressure loading of the vessel may contribute to weakening and eventual failure of the wall, corresponding to aneurysmal degeneration and rupture, respectively. In addition, the decreased thickness of aortic wall of the false lumen contributes to a greater hoop stress in the wall. As a result, further study of the solid mechanics of this pathology is warranted.

4.4.3   Clinical need for functional imaging

Diagnosis of aortic dissection founded on clinical presentation, history, and physical is solidified traditionally with anatomic imaging, namely computed tomography (CT) imaging [10, 23]. Using 4D PCMR, we are able to report on the functional status of the aorta with regards to flow, which may be of use for individual patient prognosis

and in deciding on the use of endovascular intervention. Future correlation between the observed flow reversal and luminal thrombosis may help solidify this indication for flow imaging. In addition, upon the decision to intervene surgically, fluid vortices may be used to identify locations of fenestrations, a critical landmark for endovascular repair unavailable with standard anatomic imaging. Previous investigation has found CT to be insufficient for identification of tear sites due to limitations in resolution and orientation [9, 11]. Similar difficulties arise with the use of both trans-thoracic and trans-esophageal echocardiography [9]. However, with direct visualization of vortical and jet-like structures with 4D flow MR imaging, tears may be easily identified using this modality.

4.4.4 Limitations

Due to technical challenges in the fabrication process, branches were not included in this model. While these will have an impact on the resulting fluid mechanics, flow conditions were matched to inlet conditions beyond the cephalic vessels to approximate gross fluid dynamics alterations. Further, the working fluid used (water), has a kinematic viscosity that is different from that of the blood, resulting in different fluid dynamics conditions. However, two critical dimensional fluid mechanics parameters, the Reynolds and Womersley numbers, were calculated to be on the same of order of magnitude as those of the blood, and no transitions to turbulence were observed.

4.5 Conclusions

This study demonstrates a relationship between dissection tear configuration and fluid mechanics, providing a potential link from anatomy to outcomes. Increased fenestrations allow for fluid to pass relatively unimpeded across the dissection septum, preventing reversed and recirculating flow structures from accumulating within the false lumen. This may promote sustained canalization and pressurization of the false

lumen and therefore worse outcomes. Distal tears were most easily visualized via flow imaging, which revealed transverse fluid flow and vortices accompanying these fenestrations. Mean arterial pressure was not found to have an affect on fluid dynamics of the dissected aorta, but may influence the solid mechanics of the aortic wall. Future work is aimed at characterizing the influence of other anatomic parameters, such as the location and size of the entry tear, on aortic fluid mechanics.

CHAPTER 5

ESTIMATION OF ABNORMAL WALL SHEAR STRESS IN DISSECTED AORTA VIA MRI VELOCIMETRY

5.1 Introduction

5.1.1 False lumen thrombosis and outcomes in aortic dissection

To date, the natural history of Type B dissection has not been clearly elucidated, whether treated with adjunct endovascular intervention or medical therapy alone [44, 54, 163]. However, certain pathophysiologic processes have been identifed as useful prognostic indicators, chief among them false lumen thrombosis. In theory, thrombosis of the false lumen is expected to preclude further false lumen flow, restoring true lumen flow rate to normal. As false lumen flow rate decreases to nil, the true lumen has been shown to remodel to a more normal size as the false lumen thrombus and inflammation is resolved [50, 65, 66].

While complete false lumen thrombosis has been unequivocally linked to superior patient outcomes [51, 55, 56], the difference in prognosis between patients presenting without evidence of false lumen thrombus and those with partial thrombosis is unclear. Whereas some studies have shown a completely patent false lumen to portend the worst outcome [47], others have shown partial thrombosis to have the worst prognosis, contending that the buildup of hydrostatic pressure in a blind false lumen occluded by thrombus will lead to aneurysmal degeneration and ultimate rupture [46, 58]. As a result of these data, there is signficant ongoing interest in the use of false lumen status as a marker for patient prognosis and the need for intervention. Indeed, a surrogate for thrombosis and patient outcomes would be of great clinical utility.

5.1.2 Fluid mechanics and thrombosis

Traditional theories of thrombosis have focused on the coagulation pathway and proto-typical coagulative milieu as often (incorrectly) attributed to the 19th century pathologist Rudolf Virchow [77, 164]. More recent investigation has led to the recognition of platelet adhesion and aggregation as a process separate from the canonical activation of coagulation factors and fibrinogen [70, 73, 74]. In fact, these phenomena have been found to differ not only in biological substrate but also in the local flow regime [144]. When subjected to high shear rate, von Willebrand Factor (vWF) elongates, facilitating its adhesion to both endothelium and platelets [71, 75, 80]. In this fashion, vWF acts to capture flowing platelets, initiating the process of thrombosis in high shear conditions, as seen with active arterial hemorrhage.

With this knowledge, thrombosis can be understood to result from aberrant fluid mechanics when the appropriate biological substrate is present. Under normal physiologic conditions, blood flows throughout the vascular tree with a resultant shear rate on the order of 100 - 1500 s^{-1} [73, 74]. Pathologically low shear, less than 50 s^{-1}, corresponds to relative stasis, invoking the canonical coagulation pathway as per Virchow's Triad [164]. Alternatively, at shear rates exceeding approximately 2000 s^{-1}, platelet aggregation via vWF adhesion is known to occur. Shear rates have been used in this manner to predict the possibility of natural thrombosis in different fluid environments.

5.1.3 Calculation of shear rate

Despite its utility as a measure of thrombotic potential, shear rate is not a commonly reported measure in the clinical literature. This is largely a result of the difficulty in quantifying shear rate *in vivo*. Shear rate, as well as shear stress, cannot be directly measured, and must be calculated with knowledge of the flow field. Shear stresses are

simply the non-normal, i.e. non-diagonal, components of the fluid stress tensor, τ_{ij}:

$$\tau_{ij} = -P\delta_{ij} + \sigma_{ij} \tag{5.1}$$

which results from pressure forces, $-P\delta_{ij}$, and viscous forces σ_{ij}. The viscous forces can be further described as a sum of strain (S_{ij}) and dilatation ($\Delta\delta_{ij}$) rates:

$$\sigma_{ij} = 2\mu S_{ij} + \lambda\Delta\delta_{ij} \tag{5.2}$$

Combining [82, 83], and taking into account only the non-diagonal components, i.e. $i \neq j$:

$$\tau_{ij} = \mu\frac{\partial u_i}{\partial x_j} = \mu\dot{\gamma} \tag{5.3}$$

in which the shear rate $\dot{\gamma}$ is equal to the partial derivative of the ith-direction velocity in the jth direction. As thrombosis results from interactions of humoral factors with the vascular wall, calculation of this quantity along the wall is of particular interest.

As a result of this spatial derivative, accurate calculation of shear rates and stresses is incumbent upon acquiring the velocity field at sufficiently high spatial resolution. This is compounded by the difficulty in determining analytical solutions for the velocity field given the complex geometries and boundary conditions found in biological flows. Consequentially, computational fluid dynamics (CFD) has been used extensively in the field of biofluids in order to quantify shear rates in various different flow environments. Such approaches have been used to quantify shear rates in the dissected aorta [88, 96, 98, 99, 152] and to predict locations of thrombus formation [97, 101, 102] and aneurysmal degeneration [100]. While the fine computational meshes used in these studies yield flow fields with high resolution [90], they fail to capture some of the most salient features of dissection hemodynamics. Though some models have incorporated moving walls [90, 92, 165], they have been unable to include

68

the motion of the intimal flap, which has been seen to have a significant effect on the fluid mechanics of the dissected aorta, as mentioned in prior chapters. Furthermore, the computational intensity and offline pre-processing required for such models prohibit their use in the acute clinical setting. Therefore, we propose the use of four-dimensional phase contrast magnetic resonance (4D PCMR) flow imaging to estimate wall shear stress (WSS) in the dissected aorta. Past studies have employed fitting methods to calculate WSS via MRI velocimetry [166–170] Though time and imaging system limitations restrict the maximal spatial resolution, this resolution is sufficient for order-of-magnitude computation of wall shear stress [171]. It is important to note that there exists no gold standard for the measurement of shear rate and shear stress, barring the calculation of true accuracy of results.

5.1.4 Objectives and hypothesis

The purpose of this study was to develop and evaluate the use of MRI-based computation of shear rate along the wall of normal and dissected aorta and to quantify differences between these cases. To this end, we used data from velocity fields acquired from models of the aorta in both dissected and normal cases via 4D PCMR. Wall shear rates and stresses were calculated via polynomial and first difference methods for comparison. It is hypothesized that the false lumen of dissected aorta will exhibit higher oscillatory shear and lower overall wall shear stress as compared to normal aorta that will be mitigated by intermediate fenestration.

5.2 Methods

5.2.1 Aortic flow imaging

Silicone models of dissected aorta were fabricated and installed in a flow loop, as described previously [153]. Fluid flow was established at 4 L/min via a custom-built positive displacement pump, and imaged in a 3 Tesla Prisma magnetic resonance

scanner (Siemens, Erlangen, Germany). All images were acquired with a phase encoding velocity of 80 cm/s in all three directions, voxel size of 1.0 x 1.0 x 2.0 mm, field of view of 250 x 250 mm, slab thickness of 52 mm, flip angle of 15°, echo time of 4.6 ms, and repetition time of 59.2 ms.

5.2.2   Image processing and analysis

Magnitude images were segmented semi-automatically via a region-growing level set algorithm in the Medical Imaging Interaction Toolkit (MITK, Heidelberg, Germany). Segmentations were saved as stereolithography (.stl) files and imported into the Vascular Modeling Toolkit (`www.vmtk.org`) in order to extract aortic centerlines. Additionally, these segmentations were used to mask the aortic velocity data for phase offset correction. Phase images, centerlines, and aortic segmentation contours were imported into custom software developed in Matlab (Mathworks, Natick, MA) for further processing.

5.2.3   Discrete shear computation

Redefining local coordinate system

In order to calculate wall shear rate $\dot{\gamma}$, a coordinate system transformation must be performed in order to utilize Equation 5.3 in the directions relevant to the fluid flow (Figure 5.1). A vector tangent to the fluid flow, $\vec{t}$, is defined at each centerline point m by subtracting the coordinates of the previous point, $m-1$ from the following point $m+1$:

$$\begin{aligned} \vec{t_m} &= \langle \Delta x, \Delta y, \Delta z \rangle \\ &= \langle x_{m+1} - x_{m-1}, y_{m+1} - y_{m-1}, z_{m+1} - z_{m-1} \rangle \end{aligned} \quad (5.4)$$

In such a way, a true tangent independent of the discontinuities of discrete spatial points is calculated. This vector is calculated by nearest neighbors as opposed to neighbors at each of the end points of the centerline. Next, in order to calculate
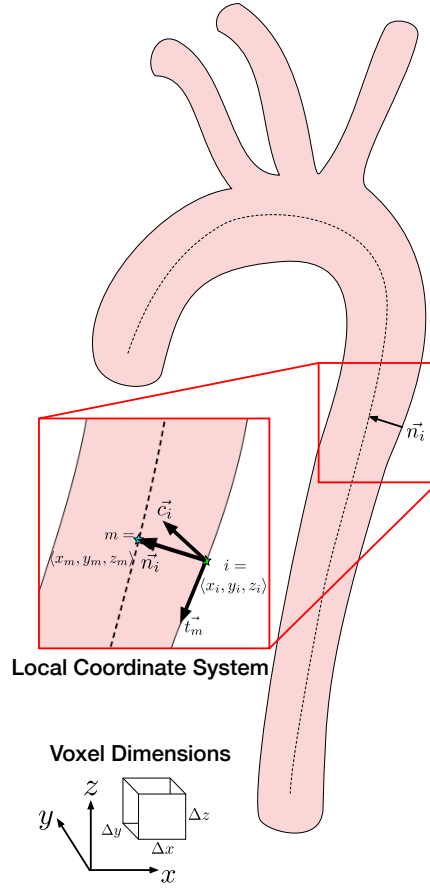
Figure 5.1: A local coordinate system must be defined for each point along the aortic wall for calculation of wall shear rate

vector $\vec{n}$ normal to the fluid flow, the centerline point closest to each point on the aortic contour is determined. A Euclidean distance between each contour point and each centerline point is calculated, and the centerline point associated with the minimum distance is chosen for every point along the contour. The normal vector can then be calculated by subtracting the given contour point (i) from the corresponding centerline point (m):

$$\vec{n_i} = \langle x_m - x_i, y_m - y_i, z_m - z_i \rangle \tag{5.5}$$

resulting in an inward pointing normal vector. The final orthogonal axis, representing the circumferential direction, $\vec{c}$, is found by normalizing the tangent and normal

vectors for the given contour point and finding their cross product:

$$\vec{c_i} = \bar{t_m} \times \bar{n_i}$$

$$= \frac{\vec{t_m}}{\|t_m\|} \times \frac{\vec{n_i}}{\|n_i\|}$$

(5.6)

This collection of unit normal vectors define the coordinate system for shear cal-culation. Both tangential (u_t) and circumferential (u_c) velocity components can be determined by projecting velocities in the standard x-, y-, and z-directions along the respective normal vectors:

$$u_t = \frac{\vec{u_i} \cdot \vec{t_m}}{\|t_m\|}, u_c = \frac{\vec{u_i} \cdot \vec{c_i}}{\|c_i\|}$$

(5.7)

and a general form for the desired shear rates in tangential and circumferential direc-tions can be derived:

$$\dot{\gamma}_t = \frac{\partial u_t}{\partial x_n}, \dot{\gamma}_c = \frac{\partial u_c}{\partial x_n}$$

(5.8)

in which velocities will be interrogated along the normal (n) direction.

Polynomial fit method

In order to accommodate both plug-like and approximately parabolic velocity profiles, velocity data were fit with fourth-order polynomials, which are capable of approximat-ing flat profiles (Figure 5.2). Using this type of model also reduces the possibility of instabilities and over-fitting associated with higher-order polynomials. This is accom-plished by fitting four points along the inward pointing normal vector, $\vec{n}$, excluding a fifth point at the aortic wall, requiring artificial oversampling of the velocity field via spline interpolation of x-, y-, and z-coordinates as well as their respective velocity components (u, v, and w). Sample points are determined by advancing in a discrete fashion along $\vec{n}$, setting the velocity at the wall to 0, and fit using the Matlab `polyfit`
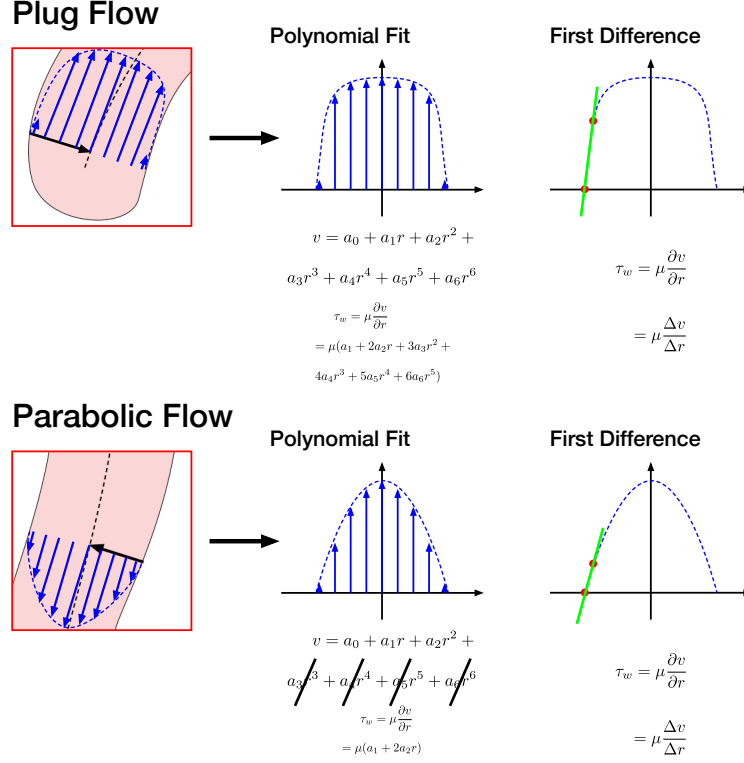
Figure 5.2: A fourth-order polynomial can be used to approximate numerous velocity profiles, principally parabolic and plug flows

subroutine:

$$v = a_0 + a_1 r + a_2 r^2 + a_3 r^3 + a_4 r^4 \tag{5.9}$$

yielding a vector of coefficients:

$$\mathbf{a} = \begin{bmatrix} a_0 \\ a_1 \\ \vdots \\ a_4 \end{bmatrix} \tag{5.10}$$

in which v is the velocity component of interest derived previously (Equation 5.7), and r is the Euclidean distance between the sample point and the given centerline point, m. The partial derivative of the resultant velocity profile can be calculated symbolically:

$$\frac{\partial}{\partial r} v = a_1 + 2a_2 r + 3a_3 r^2 + 4a_4 r^3 \tag{5.11}$$

Thus, by multiplying the coefficient vector 5.10 by the respective index and truncating after the first entry, a new coefficient vector for facile calculation of the derivative is acquired:

$$\mathbf{a}' = \begin{bmatrix} a_1 \\ 2a_2 \\ \vdots \\ 4a_4 \end{bmatrix} \tag{5.12}$$

and the derivative at the wall can be calculated by passing the Matlab command `polyval` coefficient vector $\mathbf{a}'$ and distance r from centerline point m to contour point i. In the event of a truly parabolic (second-order) polynomial velocity profile, the coefficient vector is further reduced.

Finite difference method

The finite difference method is based upon a discretization of the spatial derivative representing the shear rate:

$$[\dot{\gamma}] = \frac{\Delta v}{\Delta r} \tag{5.13}$$

In contrast to the polynomial method, the finite difference method requires velocity sampling at only one point removed from the wall, with the velocity at the wall considered zero-valued. As with the polynomial fit method, a spline interpolation is performed on the individual x-, y-, and z-coordinate and u, v, and w velocity component matrices to artificially oversample and increase near-wall resolution. Thus, by considering values at the wall, denoted w, and those immediately interior to it, $w - 1$, the discrete shear becomes

$$[\dot{\gamma}] = \frac{v_{w-1}}{\sqrt{(x_w - x_{w-1})^2 + (y_w - y_{w-1})^2 + (z_w - z_{w-1})^2}} \tag{5.14}$$

obviating the need for polynomial fitting, differentiation, and evaluation, thus shortening computational times.

Voxel method acceleration

In addition, calculation of fluid-wall distance can be performed more quickly by projecting the point-normal unit vector $\vec{n_i}$ onto a basis consisting of vector representations of voxel dimensions Δx, Δy, Δz (Figure 5.1)

$$\Delta r = \frac{\vec{n_i}}{\|\vec{n_i}\|} \cdot \begin{bmatrix} \Delta x \\ \Delta y \\ \Delta z \end{bmatrix} \tag{5.15}$$

This method is an extension of the finite difference method, employing a discrete calculation of velocity gradient, with an accelerated method for determining the distance between sample points. In this way, sampling of coordinates at the wall, and just interior to it, is unnecessary, as the distance between interior and wall is estimated by this projection (Figure 5.3). Computational time can be significantly reduced by eliminating such need for sampling the two points spatially. Furthermore, projection of the unit normal onto the voxel basis vector bounds the radial distance by two finite values, $\underset{\Delta x, \Delta y, \Delta z}{\arg\max}$ and $\sqrt{\Delta x^2 \Delta y^2 \Delta z^2}$.

Finite Difference Method:
$$[\dot{\gamma}] = \frac{u_1 - u_0}{r_1 - r_0}$$

Voxel Approximation:

$$[\dot{\gamma}] = \frac{u_1}{r_1 - r_0} = \frac{u_1}{\frac{\vec{n_i}}{\|\vec{n_i}\|} \cdot \begin{bmatrix} \Delta x \\ \Delta y \\ \Delta z \end{bmatrix}}$$
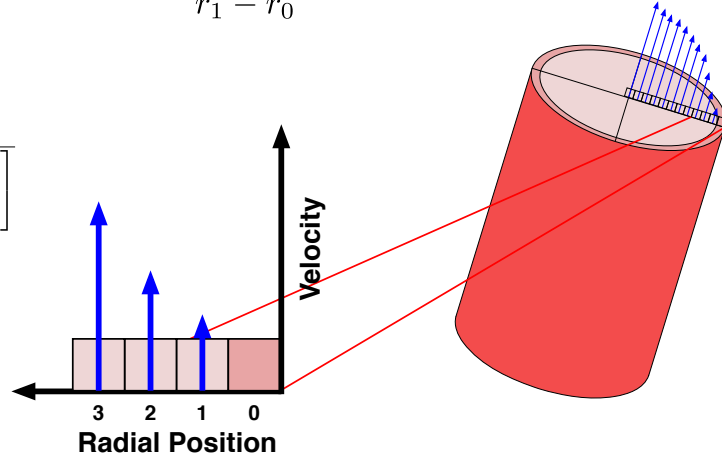
Figure 5.3: Differences in sampling for finite difference method and finite difference method with voxel method acceleration applied

Time variation

To account for evolution of the shear rate over the course of the cardiac cycle, the oscillatory shear index (OSI) was calculated:

$$\text{OSI} = \frac{\left| \int_0^T \tau_w^* dt \right|}{\int_0^T |\tau_w| \, dt} \tag{5.16}$$

with τ_w^* denoting shear stresses oriented against the direction of fluid flow as defined by the local centerline tangent vector $\vec{t_m}$. This quantity has been defined previously in the fluid mechanics literature and has been shown clinically to correlate to locations of atherogenesis in the carotid artery and abdominal aorta [145, 146, 172].

Finally, the time-averaged wall shear stress (TAWSS) was calculated for each point along the aortic contour. This quantity is an overall measure of the magnitude

of shear stress experienced at each point along the wall and is defined as:

$$\text{TAWSS} = \frac{1}{T} \int_0^T |\tau_w| \, dt \qquad (5.17)$$

5.2.4 Comparison and statistical analysis

Unwrapping of vessel along longitudinal axis

In order to perform direct comparisons between shear quantities across aortic volumes of varying spatial position, an unwrapping method was developed to perform a virtual section of the aortic volume along the greater curvature, allowing for unraveling of the shear data into a planar sheet. This is accomplished by establishing normal vectors along the centerline pointing to the greater curvature of the aorta as well as a binormal vector, grouping all wall points by closest centerline point m, determining position along the aortic wall via normal and binormal vectors, sorting these points, and performing two spatial interpolations.

Given the centerline tangent vectors, the appropriate normal and binormal vectors can be calculated with an initial input vector. The opposite of the unit normal vector in the imaging left-right direction, $-n_{L \to R}^-$ is used in this case in order to follow along the outer curvature of the aorta. A second-order tangent vector, $\vec{t'_m}$, is calculated by applying Equation 5.4 to the tangent vector components. As this vector is likely coplanar with $\vec{t_m}$, the cross product will yield the estimated binormal vector $\bar{p}_m$:

$$\bar{p}_m = \frac{\vec{t_m}}{\|\vec{t_m}\|} \times \frac{\vec{t'_m}}{\|\vec{t'_m}\|} \qquad (5.18)$$

with which the normal vector to the centerline curve can be calculated via cross product:

$$\bar{n}_m = \bar{p}_m \times \frac{\vec{t_m}}{\|\vec{t_m}\|} \qquad (5.19)$$

Once these unit normals have been established, the curve normal $\bar{n}_m$ is compared to the initial guess normal $-n_{L \to R}^-$ via dot product

$$proj_{\mathbf{n_{L \to R}}}\mathbf{\bar{n}_m} = \bar{n}_m \cdot -n_{L \to R}^- \tag{5.20}$$

If this value is below a threshold of 0.99, the guess vector $-n_{L \to R}^-$ will be used as the curve normal for that point along the centerline, otherwise the newly calculated normal vector $\bar{n}_m$ will be used as the curve normal vector. This condition ensures smooth evolution of the curve normal along the length of the centerline. New binormal and curve normal vectors are re-calculated via cross product:

$$\bar{p}_m' = \bar{n}_m \times \frac{\vec{t_m}}{\|\vec{t_m}\|}, \bar{n}_m' = \frac{\vec{t_m}}{\|\vec{t_m}\|} \times \bar{p}_m' \tag{5.21}$$

The new curve normal vector $\bar{n}_m'$ is then used as the initial guess as this process is looped through all subsequent centerline points. Once the three orthogonal vectors are calculated for each point along the centerline, the points along the wall are grouped by nearest centerline point. Then, looping through each centerline point group, the polar coordinates of each point along the wall relative to the plane defined by the tangent vector $\vec{t_m}$ are calculated. First, the projection of the wall-centerline vector $\vec{n_i}$ (5.5) onto the plane normal to the curve is found by subtracting the component of the vector in the tangent vector direction from the vector:

$$\vec{n_i'} = \vec{n_i} - \vec{n_{im}}$$
$$= \vec{n_i} - proj_{\mathbf{t_m}}\mathbf{n_i} \cdot \vec{t_m} \tag{5.22}$$
$$= \vec{n_i} - \frac{\vec{n_i} \cdot \vec{t_m}}{\|\vec{t_m}\|} \cdot \vec{t_m}$$

The projected vector $\vec{n_i'}$ can then be resolved into its in-plane components via abcissa

and ordinate defined by $\bar{n_m}'$ and $\bar{p_m}'$, respectively:

$$\mathbf{n_i}_n = \vec{n_i'} \cdot \bar{n_m'}, \mathbf{n_i}_p = \vec{n_i'} \cdot \bar{p_m'} \tag{5.23}$$

from which the polar coordinates

$$\begin{bmatrix} r \\ \theta \end{bmatrix} = \begin{bmatrix} \|\vec{n_i'}\| \\ \tan^{-1}\left(\frac{\mathbf{n_i}_p}{\mathbf{n_i}_n}\right) \end{bmatrix} \tag{5.24}$$

can be computed. Points along the aortic wall are then sorted by their computed angle θ for each centerline point, m. The aforementioned quantities (OSI, TAWSS) are then interpolated linearly along the wall in angles ranging from 0° to 360°. A second linear interpolation is performed in the longitudinal direction from the start of the centerline to its end. This process yields a map of the calculated shear parameters in a planar format with fixed dimensions for direct comparison.

5.3 Results

5.3.1 Comparison of computational methods

The three methods for shear computation (polynomial fit, finite difference, and accelerated finite difference method) were found to vary by order of magnitude in computational time required. The polynomial method required 0.249 ± 0.011 hours of computational time, whereas the normal finite difference method was computed in 2.62 ± 0.86 hours, and the accelerated finite difference method in $0.000344 \pm 4.9 \times 10^{-5}$ hours.

Visual inspection of OSI maps calculated with each method revealed no gross differences between the methods used. Despite flattening of OSI volumes into two-dimensional maps, direct statistical comparison between volumes proved difficult. Due to redundant sampling along aortic centerlines, certain centerline points pos-

sessed concentrations of sampling points in discrete segments of the aortic circum-ference. As a result, numerous zero-valued points were included in two-dimensional interpolation, preventing proper calculation of the mean value across space.

5.3.2 Variation of shear rate within experimental groups

Using the various computation methods, no gross differences were found qualitatively between the OSI maps within multiple runs of any given experimental condition (Figure 5.4).
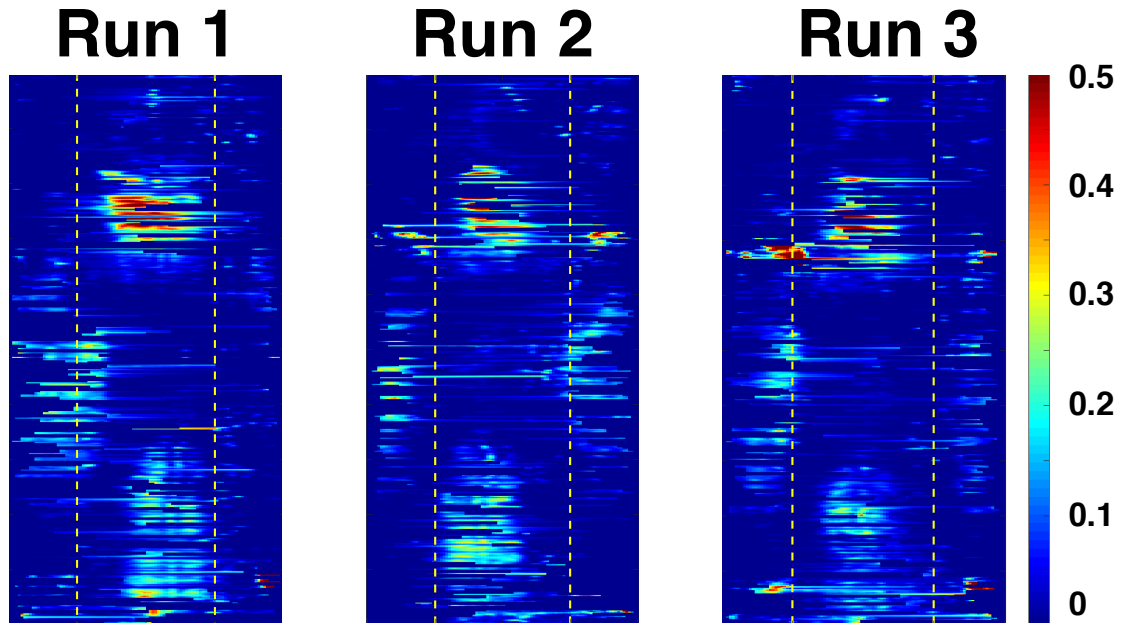
Figure 5.4: Visual inspection reveals qualitatively similar unwrapped OSI maps across experimental runs of a given dissection geometry (in this case, dissected aorta with entry and exit tear only)

5.3.3 Shear rate differences between dissection anatomies

Both normal and dissected aortae demonstrated a region of relatively high OSI in the proximal descending portion of the lesser curvature (Figure 5.5). This is con-sistent with regions of reverse flow predicted by Womersley, and reported previously in this experimental model. However, with the addition of a dissection with entry

and exit tear only, a significant elevation in OSI (maximum of approximately 0.6) was found along the greater curvature in a region corresponding to the proximal- to mid- false lumen. With the addition of a fenestration midway between entry and exit tear, this reversal region was reduced in OSI magnitude (approximately 0.5). A subsequent fenestration 75% of the distance entry and exit tear was accompanied by a disappearance of the reversed region to normal levels (OSI<0.2).
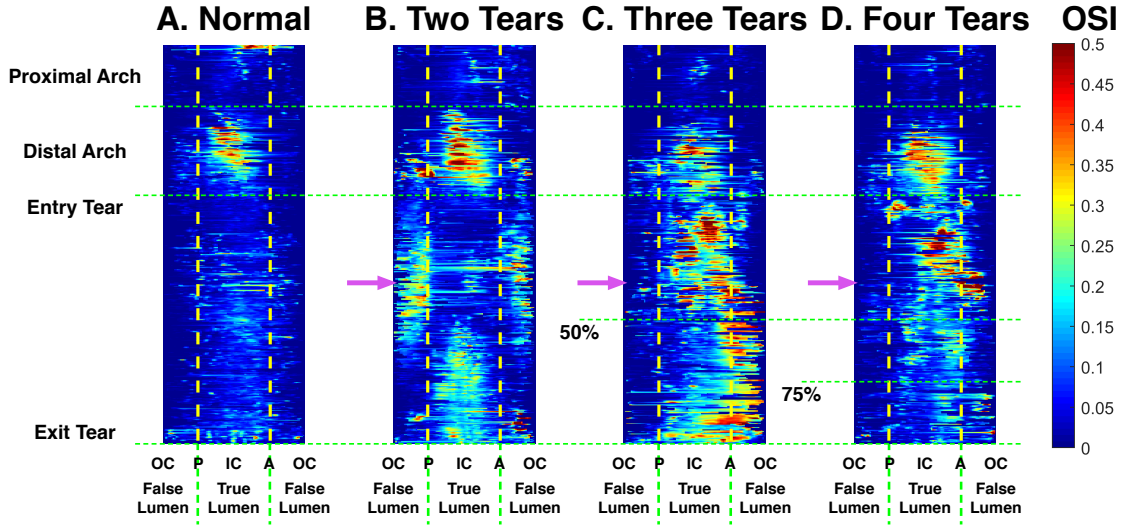
Figure 5.5: Maps of maximum oscillatory shear index across experimental runs of normal (**A**), two-tear (**B**), three-tear (**C**), and four-tear (**D**) models. Reversed flow seen in distal arch of all models due to Womersley flows along inner curvature. Significant false lumen reversal seen proximally in two tear model (purple arrow, **B**), with clearance of this zone with the addition of fenestrations (purple arrows, **C**, **D**). **OC** = outer curvature, **P** = posterior, **IC** = inner curvature, **A** = anterior

5.4 Discussion

5.4.1 Variations in shear amongst aortic dissection anatomies

As hypothesized, the presence of dissection induced regions of relatively low WSS and higher OSI than compared to normal. This effect was most pronounced in dissections with two tears (entry and exit only). However, with the addition of fenestrations, this effect was significantly reduced to the point that wall shear rates were nearly identical between normal aorta and dissected aorta possessing four tears.

5.4.2 Clinical prediction of false lumen thrombosis and prognostic implications

While the connection between any hemodynamic measure and thrombosis remains tenuous, shear rate, shear stress, and oscillatory shear index can be used to develop an intuition regarding the presence of low and recirculating flow zones. Thus, by these measures, it appears that a dissection with only entry and exit tears (no intermediate fenestrations) will exhibit significantly reversed or recirculating flows, and may be more likely to thrombose than one with many fenestrations. This reversed flow phenomenon has been described previously [153], but without treatment of the shear rate. The calculation of OSI in this case suggests that dissections with greater than two tears may fare worse given that they are subjected to less oscillatory shear and thus less likely to thrombose. Future clinical imaging of patients with varying dissection anatomies may be useful in further elucidating the relationship between anatomy, hemodynamics, and luminal thrombosis.

5.4.3 Utility of MR methdology

The methodology presented herein may prove useful in determining patient prognosis and risk as well as for planning of endovascular intervention. From the time of image acquisition, subsequent processing and computation of wall shear values can be accomplished within approximately three hours. This computational time may be significantly reduced with a few basic assumptions and use of the finite difference method and voxel dimensions (Section 5.2.3, Equation 5.15). Thus, in the absence of complications, a mapping of potential thrombogenetic foci from the patient's index imaging may be generated by the time the operator reaches the interventional room. Additionally, sufficient thrombotic potential of the false lumen as assessed by shear mapping may contraindicate the need for intervention before conclusive management is chosen. Furthermore, locations with no visible low or oscillatory shear zones may be of particular interest for the interventionist for precise deployment of endovascular

devices.

Previous methods for computation of shear rate and stress from MR velocity mapping have employed both fitting and finite difference approaches. Early methods prior to the advent of 4D PCMR made use of two-dimensional slices through vessel segments, with phase encoded in the through-plane direction [173–175]. Such methodology required manual segmentation of vessel contours, imposing intrapixel borders within the plane. With knowledge of such borders, an approximation for the velocity relationship near the wall could be calculated, accounting for partial volume effects within the phase data of a given pixel [173, 174]. Alternatively, pixels abutting the segmented aortic wall could be used to generate a paraboloid model of the velocity profile in two dimensions [175]. While the former is more generally applicable to velocity profiles of non-paraboloid shape, the latter is less susceptible to partial volume effects and inaccuracies resulting from limited in-plane resolution. Unlike the methods proposed in this study, these past methodologies are unable to account for strange aortic anatomies across a full flow field.

Similar to the methodology presented herein, recent studies make use of 4D flow PCMR, and present computations using the whole of the aortic volume acquired [166, 168, 176, 177]. These studies make use of a fitted spline of velocity values near the wall, but were limited to cases of uniluminal aorta. In the case of the dissected aorta, spline fitting may incur significant error, as the resultant cross-sections and velocity profiles of true and false lumen are often eccentric, and not amenable to smooth curve-fitting. Furthermore, while longitudinal velocities may have a somewhat parabolic profile, this is often not the case with circumferential velocities, prohibiting the use of this methodology to study non-axial shear components. Thus, despite their application towards study of healthy (and potentially aneurysmal) aorta, these methods are inadequate for study of the dissected aorta. The finite difference methodology we have developed is expected to yield a more accurate estimate of wall shear rate and stress

in the dissected aorta.

5.4.4   Limitations

Calculation of shear rates and stresses is limited by the resolution of velocities near the given boundary of interest. Thus both the spatial resolution of the images acquired, as well as the segmentation performed, may have an effect on the calculated shear quantities. Future work will be aimed at quantifying any resulting variation as well as mitigating any variations. However, as we are concerned with orders of magnitude as well as gross behavior of the fluid, and given that there exists no gold standard for comparison, an increase in perceived accuracy of these methods may not yield much improved benefit.

MRI velocity mapping is also limited by partial volume effects as a result of the finite dimensions of each phase-encoding voxel. Due to spatio-temporal averaging, the true distribution of fluid velocities within a given voxel is unknown, resulting in a singular averaged value. While a linear velocity regime may be approximated within this finite space, the precise locations of boundaries cannot be determined. This may be mitigated by manual drawing of vessel boundaries through voxels, as reported in earlier literature. However, the current approach, which relies on a level-set segmentation of the full aortic volume, imposes sharp boundaries between voxels. With this method, the aortic wall was manually identified on segmentation, and its velocity set to zero. Future attention may be aimed at modeling and adjusting boundary locations within voxels for more accurate calculation of shear at the vessel wall.

In addition, the pathophysiologic connection between fluid mechanics and biology is not fully established. Though correlations do exist, it is not clear whether measures of shear magnitude and oscillations are sufficient for prediction of thrombosis. Further clinical study is necessary in understanding whether these parameters have meaning

in the classification and risk stratification of patients with Stanford Type B dissection.

5.5 Conclusions

We demonstrate the feasibility and use of a rapid method for computing shear rate and stress from phase contrast MR images. This methodology was applied in an initial study to the treatment of oscillatory shear in a model of aortic dissection. Regions corresponding to previously described flow reversal exhibited elevated oscillatory shear index, and may represent areas of potential thrombosis. Future refinement of the methodology, as well as correlation with regions of false lumen thrombosis in patients may bolster its use for the clinical setting. The rapid deployment of the described method may also aid in its adoption for clinical use.

CHAPTER 6

ENDOGRAFT EXCLUSION OF THE FALSE LUMEN RESTORES LOCAL HEMODYNAMICS IN A MODEL OF TYPE B AORTIC DISSECTION

6.1 Introduction

6.1.1 Endovascular intervention for Type B dissection

With the advent of **T**horacic **E**ndo**V**ascular **A**ortic **R**epair (**TEVAR**), and advances in catheter-based technologies, endovascular repair has emerged as a useful treatment modality for the management of patients with Type B aortic dissection [178–180]. As an adjunct to impulse control with beta-blocker therapy, TEVAR has been proposed as a method to collapse the false lumen, allowing for distension of, and redirection of blood flow through, the true lumen [36, 181, 182]. Exclusion of the primary entry tear is thought to prevent distal filling of the false lumen, eventually leading to its depressurization and thrombosis, preventing future aneurysmal degeneration and rupture. Despite its promise, this therapy is not without complication, primarily the occlusion of branch vessels originating directly from the aorta. This is of particular concern in the region of the abdominal aorta, which contains the vital celiac axis, superior mesenteric, and renal arteries. Spinal artery occlusion may also occur, leading to paresthesia and even paralysis. As such, TEVAR is only considered standard-of-care in patients with overt complications, primarily any malperfusion syndrome, shock or sign of rupture, and aortic dilatation above 5.5 cm in diameter. In addition, superfluous device deployment is avoided in order to prevent unnecessary device- and procedure-related complications (chiefly migration, puncture [183, 184], dissection [185, 186]).

The role of endovascular intervention in the management of patients absent the aforementioned complications is yet unclear. To date, two randomized controlled trials (**ADSORB** [187, 188] and **INSTEAD/INSTEAD-XL**) [44, 45] have shown some positive remodeling of the aorta (increased true lumen diameter with decreased false lumen diameter) following stent-graft deployment in this patient population. However, at two years, no differences were seen in mortality and freedom-from-intervention rates between those receiving TEVAR and those receiving medical therapy alone. Some of the results may be confounded by not taking into account variations in structural and functional differences between the dissections of varying patients. This is compounded by a lack of understanding with regards to the effect of endovascular stent-graft deployment on the aorta.

6.1.2   Hemodynamic and structural goals of therapy

Though TEVAR has been shown clinically to have some effect on the structural mechanics of the aorta, little is known regarding its impact on the fluid mechanics of the dissected aorta. Of particular interest are the hemodynamics of aortic segments distal to the stent-graft site that contain residual dissection. Entry tear coverage via stent-graft may help reduce blood flow into the false lumen, but may be insufficient in preventing canalization via downstream fenestrations, and may prove to benefit aortic structure and function only at a local level.

6.1.3   Objectives and hypothesis

Thus, to study the hemodynamic effects of endovascular stenting, including varying deployment strategies, we deployed stent-grafts in silicone models of aortic dissection. Full flow fields were acquired via magnetic resonance velocimetry and analyzed for several hemodynamic features. It is hypothesized that deployment of endograft will restore local hemodynamics to normal, but will leave distal segments of dissection

unchanged. Further deployment of grafts along the dissection is expected to bring about complete restoration of the normal hemodynamic milieu of the aorta.

6.2 Methods

6.2.1 Stent-graft selection and deployment

A model of the thoracic aorta was fabricated with a descending dissection originating at the flexure of the lesser curvature, extending 20 cm along the longitudinal extent of the aorta. An exit tear was formed at the distal extent of the dissection flap, which possessed a span of 50% of the aortic circumference. Secondary fenestrations were added at locations 50% (10 cm) and 75% (15 cm) of the distance from entry to exit tear in order to mimic dissections with multiple flow pathways. Despite the wide heterogeneity in dissection anatomies and tear locations, a single configuration of tears was used to control for variations due to anatomy. Four total tears were choosen in order to mimic human dissections, which generally possess multiple fenestrations. In addition, prior analysis indicates that highly fenestrated dissections are least likely to exhibit pro-thrombotic flow reversal and oscillatory shear, and thus at highest risk for maintaining patency. Two units each of 80-mm and 60-mm Valiant™ thoracic stent grafts with Freeflo™ extension (Medtronic, Santa Rosa, CA) were obtained from the manufacturer. Stent-grafts were deployed in sequential fashion between MR flow imaging studies. An initial 60 mm graft was deployed to exclude the entry tear and provide coverage of 60% of the initial dissection segment, totaling 60 mm (Figure 6.1A). Each subsequent graft was inset in the previous in order to provide continuous coverage of the dissection: an 80 mm graft was deployed with a 10 mm overlap inside the first device (Figure 6.1B), followed by another 80 mm graft interposed 30 mm within the previous (Figure 6.1C), with a final 60 mm graft inset 20 mm within the previous device (Figure 6.1D). In this manner, each subsequent device covered the next immediate tear site with a consistent 60% coverage of the residual dissection

segment.
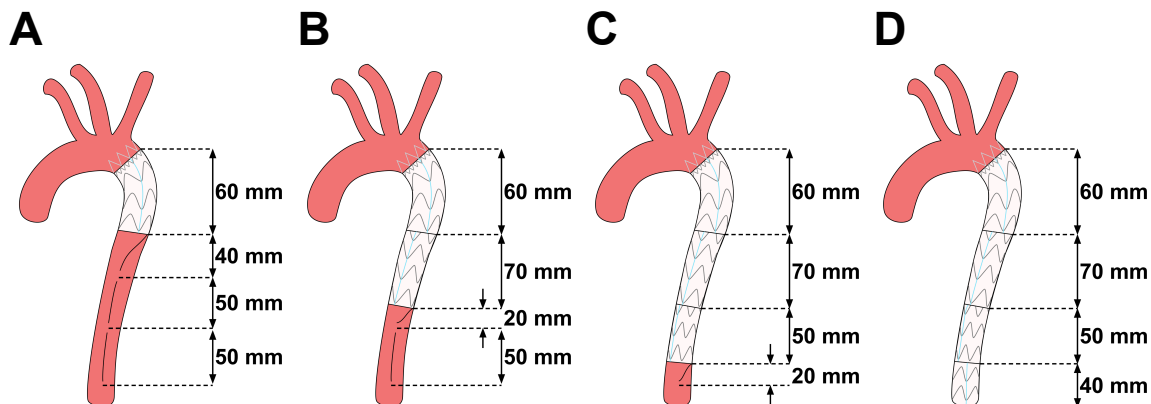
Figure 6.1: Configurations of sequential device deployments in aortic dissection model

6.2.2 Flow loop and imaging setup

Once stented, the model was installed in a flow loop, as described previously (Section 3.2.1), and connected via PVC tubing to a pulsatile positive-displacement pump (Figure 3.1). Full flow fields throughout the aortic volumes were acquired with a four-dimensional PCMR protocol (Section 3.2.2) and exported for processing and analysis.

6.2.3 Image processing and analysis

As described previously, five slice locations were chosen along the extent of the dissected aorta (Section 3.2.3) following segmentation and centerline calculation. Absolute and relative luminal flow rates, as well as reverse flow index, were calculated for each slice (Section 3.2.4, Equation 3.1). Segmentations and centerlines were subsequently used to compute wall shear rate and shear stress, as well as oscillatory shear index for each point along the aortic wall (Section 5.2.3). OSI maps were unwrapped and compared (Section 5.2.4) across device configurations relative to normal aorta.
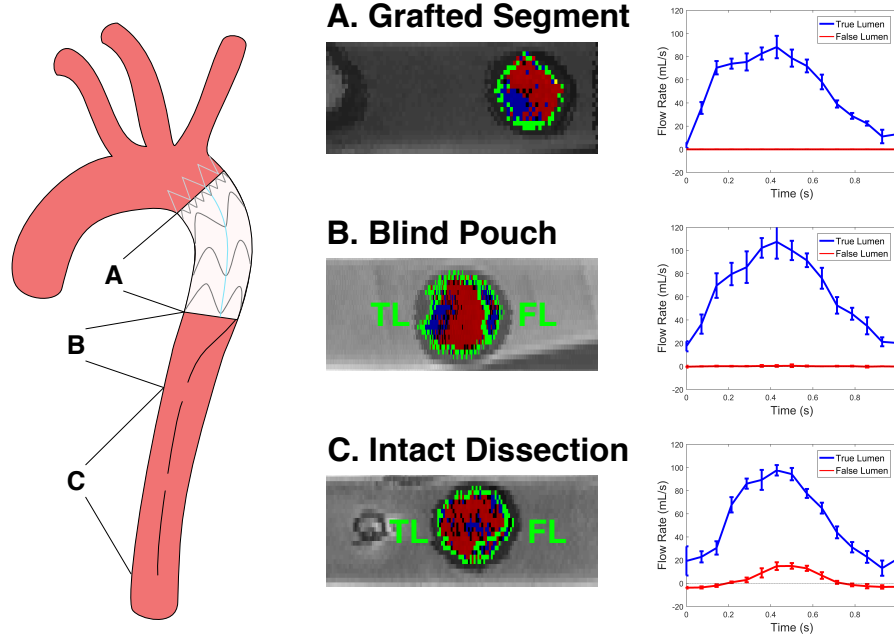
Figure 6.2: Demonstrative late diastolic axial Doppler images and true and false lumen flow waveforms in grafted dissection **A**, blind pouch regions **B**, and peristent dissection **C**

6.3   Results

6.3.1   Normalization of fluid flow in grafted region

Computed visualization of the flow in grafted aortae revealed a normal, parabolic velocity profile through aortic regions covered by stent-graft. In these segments, false lumen could not be identified, and true lumen flow remained positive throughout the cardiac cycle (Figure 6.2A). Cross-sectional imaging confirmed the presence of a parabolic velocity profile in the presence of endograft with maximum velocities of 30.4 ± 8.4 cm/s occurring at 0.333 ± 0.16 s within the cycle in the presence of a single graft. As with normal aorta, a region of reversed flow was seen at the proximal descending aorta along the lesser curvature, resulting from the oscillatory Womersley flow.

Table 6.1: Maximum true and false lumen velocities of various graft strategies along the dissection. All velocities reported as cm/s

Region	Single Graft		Two Grafts		Three Grafts		Four Grafts	
	True	False	True	False	True	False	True	False
Entry	24.6±3.3	-	23.7±2.9	-	20.8±3.2	-	25.3±1.5	-
25%	30.4±8.4	-	26.6±0.9	-	28.8±2.8	-	27.3±1.8	-
50%	28.4±1.3	5.8±2.7	27.7±3.3	-	29.1±4.4	-	26.4±2.2	-
75%	30.3±3.2	7.0±2.1	34.1±7.4	5.6±2.4	27.0±3.9	-	31.6±6.1	-
Exit	26.4±3.8	5.9±4.1	24.4±1.1	4.1±1.9	25.1±3.1	8.4±6.2	25.5±2.9	-

6.3.2   Low velocity, oscillatory flows in immediate post-graft region

Just distal to implanted endografts, a blind pouch was formed from the distal extent of the graft to the subsequent fenestration. While the false lumen could be visualized in these sections, these areas of residual false lumen were characterized by low velocity flows (maximum velocity 5.8 ± 2.7 cm/s in single-graft condition) with decreased flow rates and increased oscillatory shear. False lumen flow waveforms demonstrate low flow rate oscillating about 0 combined with a high reverse flow index (Table 6.2). However, the true lumen in these regions maintained forward flow and a parabolic velocity profile, with maximum velocities approaching 28.4 ± 1.3 cm/s at 0.452 ± 0.087 s of the cardiac cycle.

Table 6.2: True and false lumen reverse flow index (RFI) calculated along grafted and ungrafted segments of dissected aorta with increasing number of devices

Region	Single Graft		Two Grafts		Three Grafts		Four Grafts	
	True	False	True	False	True	False	True	False
Entry	5.06	-	4.32	-	4.18	-	3.36	-
25%	4.50	-	2.21	-	4.84	-	3.77	-
50%	2.63	31.9	4.31	-	5.28	-	3.16	-
75%	4.05	33.1	4.81	28.8	3.93	-	3.07	-
Exit	4.92	24.0	4.64	3.31	4.25	21.9	4.38	-

6.3.3   Distal recapitulation of dissection hemodynamics

In the regions of free-standing intimal flap (i.e. segments with no endograft present, possessing tears on two ends), false lumen flow was maintained as in the absence of endograft. While the false lumen possessed a crescent-like cross-section with a dominant true lumen in these regions, velocities were comparable to those seen in the un-stented case (maximum velocity 7.0 ± 2.1). This true-dominant configuration maintained the parabolic velocity profile seen more proximally, with maximal luminal velocities of 30.3 ± 3.2. Vortices were observed to form in computed visualizations at tear sites not covered by devices. Unlike those observed previously, when grafts were deployed, these vortices were left-handed in orientation with respect to the anterior-posterior axis.

6.3.4   Variations with varying number of endografts

As devices were added to the model, fewer regions of false lumen were visualized, with subsequent loss of flow data in these regions. Trends seen in the different regions (grafted, blind pouch, persistent dissection) were maintained in their respective areas as grafts were added. Blind pouch regions exhibiting high OSI (Figure 6.3A, purple arrow) were eliminated when covered by stent-graft (Figure 6.3B). Small foci of elevated OSI were observed in the proximal true lumen when completely covered by stent-graft, with concomitant reduction in the region corresponding to Womersley reversal. This may represent a migration of the Womersley focus distally.

6.4   Discussion

6.4.1   Local restoration of flow with endovascular intervention

As hypothesized, endografts were found to restore normal parabolic velocity profiles in the segments that were in fact stented. In addition, complete obliteration of the
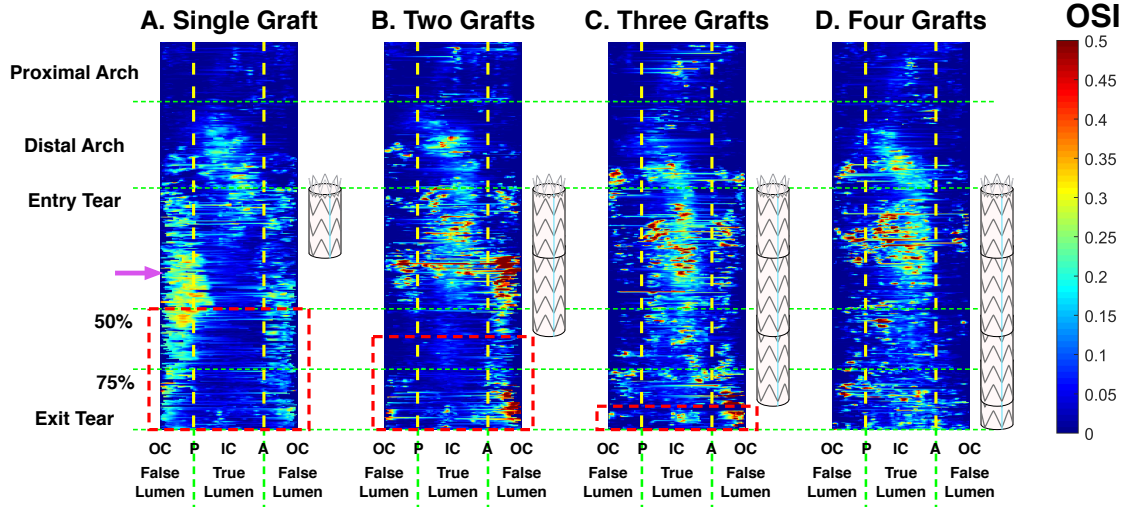
Figure 6.3: Changes in oscillatory shear index seen with additive device deployment in four-tear dissections possessing a single (**A**), two (**B**), three (**C**) and four (**D**) devices. Note prominent zone of oscillatory shear in blind false lumen pouch in presence of single graft (purple arrow). Non-oscillatory shear observed in the intact false lumen distal to the most distal grafting site (red box)

false lumen was achieved wherever endograft was deployed. Blind pouch segments resulted from bare dissection segments between distal extents of grafts and subsequent fenestrations, and exhibited low-velocity, reversed flows that are suspect for coagulative thrombosis. However, distal segments with adjoining fenestrations were found to contain normal velocity flows and shear rates with minimal reversal, and may therefore be protected from thrombosis. Distal to the trailing edge of the endograft, fluid was seen to traverse transluminally at exit tear sites, leading to left-handed diastolic vortices about the anterior-posterior axis (i.e. oriented from true to false lumen at fenestration sites, Figure 4.3). These vortices form in a direction opposite to those observed in the absence of stenting (Section 4.3.1) and indicate the presence of local, transient pressure defects in the false lumen at fenestration sites.

6.4.2 Recommendations for treatment

Endograft exclusion of the most proximal entry tear with concomitant false lumen obliteration is essential in preventing filling and patency of the false lumen from

central aortic fluid flow, and is considered a foundational principle in endovascular intervention for patients with Type B dissection. However, given these results, it may be insufficient in eliminating unfavorable hemodynamics downstream of the initial site of deployment (Figure 6.4A). In fact, the transluminal fluid shift observed indicates that without continued stenting, the true lumen may aid in repressurizing and re-canalizing the false lumen. As such, we suggest two strategies in order to restore normal fluid flow to the dissected aorta.

A   **B**   **C**   **D**   **E**

Proximal Only   Long Segments Only   Alternating Tears   Extend and Alternate   PETTICOAT

Fewer Devices   More Devices
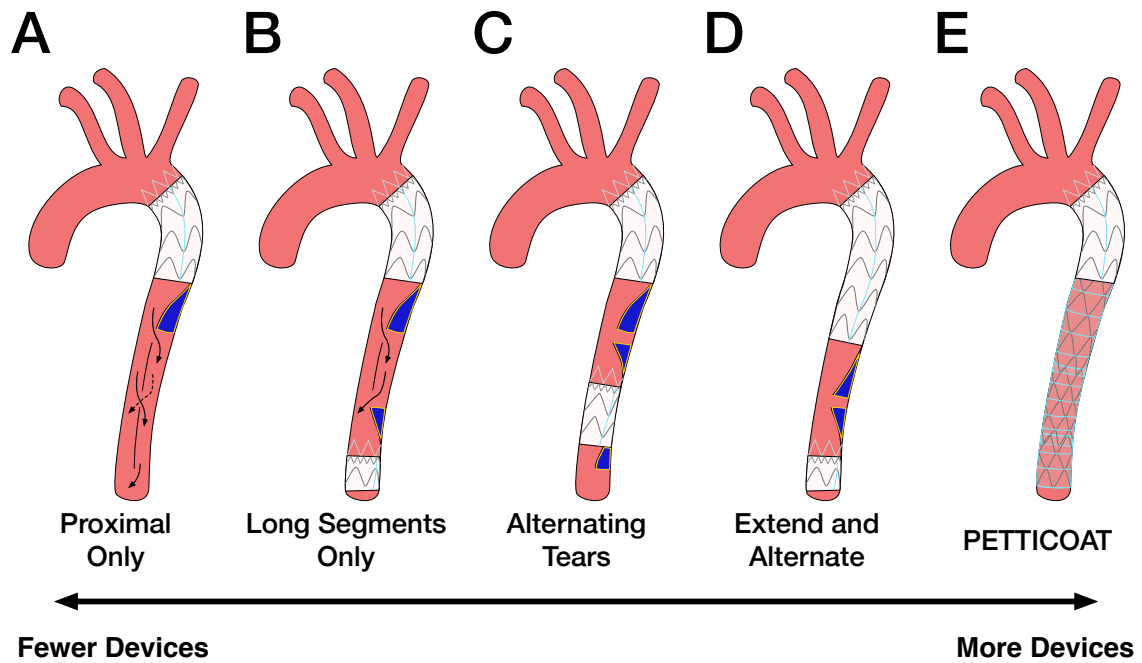
Figure 6.4: Various deployment strategies for optimum false lumen obliteration and restoration of true lumen. Sites of expected thrombus colored in deep blue.

First is the strategy described above, the "full-metal jacket" method, in which sequential endografts are deployed along the length of the dissected aorta until all fenestrations are excluded. Popularized as the PETTICOAT (**P**rovisional **ExT**ension **T**o **I**nduce **CO**mplete **AT**tachment) concept, which has been studied in several series from varying clinical groups [127, 189]. In addition, the STABLE (**S**tudy of **T**horacic **A**ortic Type **B** Dissection Using Endo**L**uminal R**E**pair) randomized control trial evaluated the use of a commercial composite device consisting of a covered stent graft for

proximal tear coverage and a distal bare-metal component, allowing for false lumen obliteration with branch vessel occlusion (Figure 6.4E). While the results of these strategies have been promising, they require a significant amount of hardware to be deployed within the patient, increasing the risk of device- and procedure-related complications. In addition, despite favorable changes to the aortic anatomy (i.e. relative increase of true lumen area with concomitant decrease in false lumen area), functional, hemodynamic assessments were not performed in these studies.

A second possibility, the "divide and conquer" strategy, is to deploy stent grafts solely at tear sites to prevent canalization of the corresponding segments of dissection. This technique would include exclusion of the primary entry tear along with stent-graft coverage of subsequent re-entry tears. Shorter segments containing less than a critical length of free intimal flap could be ignored (Figure 6.4B) or included in the grafting of the previous segment (Figure 6.4D). Another variation of this technique is to exclude alternating tear sites, creating blind pouches emanating from the stent-graft edges (Figure 6.4C). As these pouches are seen to induce low velocity, reversing flows, they are likely to thrombose naturally. Combined, these strategies balance the need for induced thrombosis and restoration of true lumen caliber with a reduced device burden.

Additionally, positioning of the devices to exclude more proximal tears of each segment is expected to provide a more favorable hemodynamic environment than coverage of distal tears. While both strategies are hypothesized to induce low and stagnant flow zones within the false lumen, the former will likely reduce false lumen filling. In order to reach blind pouch segments with proximal coverage, fluid is required to sharply change flow direction to enter the fenestration and propagate retrograde towards the proximal end of the pouch. This direction change requires an expenditure of fluid kinetic energy, making entry of fluid into this site less likely. Coverage of tears of the distal end of a given segment allow for fluid entry via simple

flow division mechanisms. This may prompt filling and pressurization of the false lumen, which has been hypothesized as a mechanism for false lumen dilatation.

6.4.3   Need for diagnostic and followup functional imaging

Selection of appropriate devices and deployment strategies may make use of the imaging techniques employed herein. By calculating fluid velocities and oscillatory shear index throughout the aortic volume, the physician may have some intuition as to which zones of the dissection are most likely to thrombose naturally. If the decision is made to intervene by endovascular means, functional imaging may give a more precise indication of zones that may remain patent unless appropriate obliteration is achieved via stent-graft. Flow imaging may also play a crucial role in immediate postoperative evaluation of the success of the procedure as well as long-term followup of the patient. In fact, while standard anatomical imaging techniques may assess relative luminal calibers, they are inadequate in describing the restoration of normal aortic hemodynamics. While the anatomy and solid mechanics of the aorta play a crucial in the long-term survival and freedom from reintervention in patients, the fluid dynamics may determine functional outcomes, as well as contribute to the solid mechanics.

6.4.4   Limitations

Whereas the PETTICOAT method makes use of a proximal covered stent-graft with distal bare metal stents, we employed stent-grafts throughout the aorta for this study. While the stent-grafts may provide superior sealing via tear exclusion, they achieve the common goal of obliterating the false lumen. Furthermore, while branch vessel occlusion is a concern with covered grafts, this model did not possess branches, obviating the issue. Future study of branch vessel perfusion with varying grafting strategies is recommended in order to understand the interaction between interven-

tion and complications.

In addition, MR imaging of the aorta may be affected by the presence of graft materials in the vessel. The nitinol stent-grafts used did not appear to induce phase artifacts within the dissected segment of aorta. However, redundant graft material involuted upon itself, creating zones within the aortic lumen devoid of fluid. This formed a scalloped pattern along the contour of the grafted aorta, and may have lead to errors in the calculation of wall shear stress (WSS).

6.5   Conclusions

We report the first study of its kind to systematically test deployment of varying numbers of endografts in a model of aortic dissection with corresponding hemodynamic assessment. This work reveals inadequate collapse of false lumen distal to the extent of the grafted region, suggesting that sole coverage of the primary entry tear is insufficient in restoring true lumen area and flow along the whole of the dissection. However, the formation of blind pouch regions in the false lumen promoted low-velocity, oscillatory flows that are expected to cause thrombosis. These results suggest a need for more aggressive device deployment if absolute restoration of aortic anatomy and hemodynamics is desired. Further study of varying deployment locations and relevant effects on branch vessel perfusion are critical in developing an understanding of both risks and benefits of endovascular intervention in patients with Type B aortic dissection.

CHAPTER 7

CONCLUSIONS

7.1 Original hypotheses and goals

7.1.1 Dissection anatomy, hemodynamics, and risk

This work has initiated systematic study of the unique fluid mechanics of aortic dissection in a model with a mobile dissection septum. As predicted, controlled variation of the dissection anatomy resulted in stereotyped changes to fluid flow in our *in vitro* model. In the absence of secondary fenestrations between entry and exit tear, an unexpected pumping action of the false lumen was observed, in which the motion of the intimal flap appeared to push false lumen fluid in a retrograde fashion towards the entry tear. Further experimentation found that intermediate fenestrations reduced this pumping action and resultant flow reversal in the false lumen. These results lend credence to current thought that certain dissection anatomies may have a higher propensity for aneurysm formation and need for intervention. Though the pathophysiologic mechanisms resulting from altered hemodynamics are yet to be fully elucidated, this work suggests that the anatomy indirectly affects outcomes via its effect on fluid flow. As a surrogate for the underlying fluid mechanics, anatomy may thus have a role in predicting the natural history of disease and individual patient prognosis. While only a limited number of anatomies were investigated, it is hoped that this will instigate further study of the relationship between dissection anatomy and fluid mechanics.

7.1.2 Thrombosis prediction via MRI velocimetry

As originally desired, a methodology for computing shear rate, oscillatory shear index, and time-averaged wall shear stress from PCMR images was developed. The speed of these calculations and the minimal pre-processing required (segmentation and centerline calculation) may allow for rapid computation in the clinical setting. While the prediction of thrombosis from these data is not yet attempted, this important use is feasible, and is a subject of future study. Serial PCMR studies of patients with dissection may be used to determine the effectiveness of this methodology for predicting the formation of thrombus. Further refinement of the processing may reduce computational times and allow for direct implementation in standard MR analysis software.

7.1.3 Endografts and dissection hemodynamics

The described study of endograft deployment is to our knowledge the first of its kind to systematically deploy endovascular devices and acquire flow fields in dissection. The use of these devices did show an improvement in aortic hemodynamics, as originally hypothesized. However, this effect was concentrated in the grafted segment, with persistent canalization of the false lumen distal to this point. Complete stent-graft exclusion of the false lumen achieved intimal flap apposition and restored true lumen flow to normal for the length of the aorta, at the cost of four devices used. Future investigation aimed at minimizing the need for unnecessary devices is warranted. Additionally, the replication of the hemodynamics of patients with poor outcomes despite receiving endovascular intervention may be useful in determining what kind of fluid mechanics outcomes are undesirable following graft deployment.

7.2 Future modeling of aortic dissection

7.2.1 Experimental and computational approaches

While numerical solutions have been used in numerous studies of aortic dissection, they largely failed to capture the motion of the intimal flap and the resulting fluid flow. With the use of an experimental model possessing such a flap, we have demonstrated the inclusion of movement of this structure as essential to the study of dissection. This is compounded by the need for understanding of the fluid mechanics of the acute phase of dissection, during which intervention is imminent, as within this period the flap is thought to be most mobile. The hemodynamic consequences of this behavior may contribute to the outcomes of patients as well as contribute to the symptomatology and presentation of these patients. This does not disqualify the use of computational fluid dynamics from future research in this field. It does, however, emphasize the need for more complex models incorporating fluid-structure interactions if computational approaches are to be used. Alternatively, the use of experimental models may yield more realistic results via a simpler approach. Such models also facilitate the study of endovascular intervention in a controlled and systematic fashion, as seen in our study. Models with greater clinical fidelity are under investigation, and a realizable goal for the near future. In addition, refinements to the processing techniques will allow for more in-depth study of the complete flow field acquired via PCMR. As such, experimental models are suggested as the system of choice for studying acute dissection. The rich hemodynamics seen with a mobile intimal flap and physiologic inlet conditions are necessary for understanding the range of behaviors possible in the dissected aorta. While patient-specific models of dissection may allow for precise knowledge of the hemodynamics of individual patients under varying conditions, this approach is time-consuming and unfit for clinical practice. Ultimately, comparison of index hemodynamic measurements to a look-up table of various fluid parameters and

structures would provide rapid recommendations for clinical practice. Further rigorous study of the pathophysiological consequences of various dissection hemodynamics are necessary to validate such clinical methodology.

7.2.2 Translation to clinical practice

As our intuition of aortic hemodynamics in the presence of dissection expands, one must keep an eye towards translation of these principles to the clinic. Despite the complex flow patterns seen in these models, validation with clinical imaging is of utmost importance in the eventual extrapolation to clinical dissection. This is made difficult by the wide variety of dissection anatomies and flow patterns seen clinically, which may not exhibit the repeatable, stereotyped flows seen in our models. However, gross similarity of septal motion and fluid flow to that of the model may be considered sufficient for more widespread adoption of these results. The intuition developed from this model, in particular the influence of flap motion on dissection fluid mechanics, will guide imaging and study of patients in the future. Equipped with our new understanding and awareness of potential flow phenomena, study may be focused in the appropriate direction. In particular, investigation of abnormal features such as reversed flows, transluminal jets, and vortical structures may prove critical in understanding the natural history of aortic dissection.

The radial pressures and disturbed flows resulting from impingement of transluminal jets on the free aortic wall may contribute significantly to the development of aneurysm in certain fenestrated segments of the dissection. These features appear periodic, which would lead to sustained oscillations to the far wall shear stress, as well as cyclic fatigue loading of the media and adventitia. Preious studies have shown that sites and orientations of jet impingement on the aortic wall correspond to areas of dilatation in the setting of bicuspid aortic valve [161, 190]. Vortices, especially those observed from violent mixing of false and true lumen flows at the exit tear,

are seen to contribute to increased oscillations in shear, and may also contribute to endothelial and sub-endothelial dysfunction and eventual aneurysm. In addition to these gross flow features, the divided and compressed luminal compartments may create an apparent stenosis. In vivo studies have shown that disturbed, and perhaps turbulent, flows distal to vascular stenoses may lead to vessel dilatation and aneurysmal degeneration [191]. The combination of vortical fluid structures and relative luminal stenosis with distal expansion zones (i.e. undissected, normal-caliber aorta) are likely to contribute to formation of aneurysm at these locations. All of these flow features (jets, vortices, and stenoses) can be induced in vivo, and should be tested in the setting of experimental aortic dissection to determine their role in aneurysm formation. In addition, systematic imaging of patients in acute, subacute, and chronic phases will help elucidate the prevalence and evolution of these flow features over time, and can then be correlated to disease progression and outcomes. In particular, the development of false lumen and thrombosis and aneurysmal degeneration may be closely tied to these features and showed be tracked along with the hemodynamics. Those fluid structures leading to dilatation can then be considered a focus for targeted hemodynamic intervention.

7.3 Clinical recommendations

7.3.1 Hemodynamic risk and indications for intervention

Patient anatomy has traditionally been the standard imaging feature used to determine an individual's need for endovascular intervention in the absence of clinical symptoms consistent with complicated dissection. While this approach addresses pressing and readily-visualized consequences of dissection, it ignores the impact of blood flow, which is the ultimate arbiter of adequate tissue perfusion. In addition, abnormal anatomy is most likely the sequela of prolonged alterations in aortic hemodynamics, as the solid mechanics, and thus structural integrity, of the vessel are

largely dependent on the fluid dynamics. The hemodynamic precursors to aortic degradation may be imaged and used to characterize a patient's risk in advance of structural changes.

As previously mentioned, certain fluid mechanics may raise suspicion due to their interaction with the solid mechanics of the aortic wall. While the jets observed in our fenestrated models were oriented from false to true lumen, it is possible that they may be directed in reverse in the patient. As jets interact with the opposing false lumen wall, they may subjugate it to undue radial stress, leading to eventual degeneration and formation of aneurysm. A similar mechanism is postulated for the formation of aneurysm of the ascending aorta in patients with bicuspid aortic valve. Studies have shown a correlation between zones of stereotyped jet impingement and location of ascending aortic aneurysm. Should this correlation hold in the setting of aortic dissection, interventional strategy should be shifted towards elimination of these jets as they may actively contribute to aneurysmal degeneration of the aorta. Rapid identification of jet locations can be performed via visualization of flow imaging data, and cannot be obtained from typical anatomic imaging. Intentional underestimation of encoding velocity in the left-right or anterior-posterior direction may be used provide sharp contrast at jet locations due to phase aliasing.

Vortices may also be visualized with either MRI or ultrasound modalities, and may serve to identify fenestrations. Based on our study of the effects of intermediate fenestrations on dissection hemodynamics, this identification of anatomy based on flow features may be useful for categorizing a given patient's risk of maintaining false lumen patency. Though basic science research has not fully established the role of reversed flow and oscillatory shear on endothelial dysfunction and thrombosis, this feature of dissection flow may be of utmost importance and should be considered in future study. Characterization of this type of flow with serial imaging may be correlated to areas of thrombosis or aneurysmal degeneration even in the absence of

an elucidated pathophysiological mechanism.

Eventually, correlations between aberrant hemodynamics and patient outcomes will aid in determining a patient's prognosis and may prove useful in selecting patients for intervention. Furthermore, as the specific hemodynamics outlined above are correlated to certain dissection anatomies, the use of anatomic imaging in prognosis and surgical planning will be amplified.

7.3.2   Novel endovascular techniques and devices

Despite the hemodynamic improvements observed with endovascular intervention in this work, it is not clear why intervention does not show a marked benefit in mortality or freedom-from-events compared to medical therapy alone. The results of our work suggests that while aortic fluid mechanics may be improved in the grafted regions, distal fluid flow remains disrupted due to persistent false lumen canalization. This may in fact promote degeneration of the abdominal aorta as fluid dynamic alterations seen originally in the thoracic aorta may be concentrated in the abdominal region following intervention. A distal migration of aortic hemodynamics is further suggested by the descent of the Womersley reversal region in the stented aorta. Though approaches such as PETTICOAT attempt to mitigate such issues by extensive intervention along the aorta, these strategies have failed to show improved outcomes. Such strategies ignore the potential perfusion of end organs via the false lumen as well as dynamic obstruction of visceral branches by the mobile dissection septum. In such situations, selective maintenance of false lumen patency may be crucial for patient survival.

We therefore argue for more judicious use of endovascular intervention to be tailored to the hemodynamic needs of individual patients. Some patients may indeed need complete enodgraft and stent coverage of the aorta from left subclavian artery to the iliac bifurcation, while others may be sufficiently treated with a single device or beta-blockers. This is also incumbent on a reassessment of the goals of inter-

vention and their respective outcomes. While clinical outcomes such as mortality, freedom from aortic events, and freedom from reintervention are the standard for success, the usefulness of secondary endpoints such as true and false lumen areas is unclear. Hemodynamic indicators for the potential of the dissected aorta to develop aneurysm is of critical importance in this regard. In addition, flow to the visceral and peripheral vasculature must be preserved and assessed for evaluation of the success of intervention.

More formally, fenestrations at which jets are seen should be considered immediate sites of intervention, as this fluid flow is suspicious for future aneurysmal degeneration. In addition, if not supplying visceral branches, areas of false lumen with high enough flow should be considered for stenting. If, on post-deployment imaging, these jets are relieved and false lumen flows reversed, the outcome may be deemed sufficient. In the event of branches (i.e. renal arteries) in close proximity to the intervention site, guidewires may be placed for protection, followed by deployment of appropriately-sized stents to maintain luminal patency. Complete restoration of aortic hemodynamics and prevention of aneurysm will require aggressive and extensive stent-graft deployment along the length of the dissected aorta. A residual blind pouch with distal opening, which would be expected to thrombose naturally, can be left at the exit tear site. Completion and eventual followup imaging should be performed in both thoracic and abdominal aortic segments in order to ensure elimination of aberrant flow patterns throughout the aorta.

7.3.3   Clinical impact of functional fluid imaging

Above all, this work supports the need for functional imaging in the workup of aortic dissection, which should be considered an integral component in assessing cardiovascular disease. As of this publication, functional imaging is already used consistently in the workup for carotid disease (Duplex ultrasound) as well as coronary (angiography,

fractional flow reserve) and valvular (Doppler echocardiography) heart disease. While structural changes may aid in description of deviation from the normal anatomy, they are insufficient in characterizing the functional impact on a given patient's physiology. In addition, though approximation of normal anatomy is desired following intervention, it does not directly inform upon the functional improvement achieved with intervention, which is a more specific and clinically useful endpoint. Thus functional imaging is essential in determining individual patient risk, performing preoperative planning, and assessing the overall hemodynamic outcome of a procedure.

Currently, 4D flow MRI is not a widely-established clinical protocol. Clinical adoption for aortic dissection workup is further complicated by the acuity and urgency of disease. A conservative estimate accounting for patient transportation, scan setup, and running of the protocol would require an hour of time. All relevant processing could be subsequently performed within another hour while a procedural room is being prepared. Such execution is feasible, but does not allow for rapid performance and assessment by the provider. Some of the hemodynamic features described herein, however, could be translated to transesophageal echocardiography (TEE). This modality is already in widespread clinical use, in particular for the assessment of Type B dissection [158, 192–195]. Unlike 4D PCMR, TEE does not afford the reconstruction of the full velocity field, but rather tomographic slices acquired in a plane parallel to an array of acoustic elements. Doppler techniques can be used to determine the presence of areas of reversed and recirculating flow, as with our MRI methodology. However, Doppler TEE can acquire only those fluid velocity components directed along the imaging plane. Thus, significant functional aspects of the dissection may be missed due to incomplete scanning along the extent of the aorta, as well as acquisition of images and velocities in suboptimal planes. These limitations demonstrate the need for a more comprehensive imaging modality such as 4D PCMR. Clinical series relating these fluid mechanics phenomena would be invaluable

for future study and management of dissection.

Therefore, we recommend performing magnetic resonance angiography (MRA) and 4D PCMR on patients with stable Type B dissection. As patients absent acute complications of aneurysm, malperfusion, or rupture do not require immediate intervention, the time required to run a 4D flow protocol can be taken. MR angiography can provide the clinician with structural images whose quality rivals that of computed tomography (CT). In addition, as MRA operates on non-ionizing radiation, time-resolved scans can be performed, allowing for assessment of the dynamics of aortic wall and intimal flap, which would require high radiation doses for similar CT imaging. With 4D flow protocols, an overview of the patient's hemodynamics can be obtained without concern for missing anatomy or velocity components. Unlike with CT imaging, the flow of blood, not simply its presence, can be assessed, and used to determine whether the viscera are sufficiently perfused and through which lumen they are receiving blood. Precise localization of suspicious fluid structures such as impinging jets, vortices, and lumen flow reversal may be used during preoperative planning. With new techniques in image volume registration and co-localization [196], preoperative flow MRI images could be merged with intraoperative fluorescence angiography used for endovascular intervention. Followup PCMR imaging can then be used to assess whether or not appropriate hemodynamic outcomes were achieved with the procedure.

BIBLIOGRAPHY

1. Kumar, V., Abbas, A. K., Aster, J. C. & Fausto, N. *Robbins and Cotran Pathologic Basis of Disease* 8th edition (Saunders, 2009).

2. Glagov, S. & Wolinsky, H. Aortic Wall as a 'Two-phase' Material. *Nature* **199,** 606–608 (1963).

3. Wolinsky, H. & Glagov, S. A Lamellar Unit of Aortic Medial Structure and Function in Mammals. *Circulation Research* **20,** 99–111 (1967).

4. Zatina, M. A., Zarins, C. K., Gewertz, B. L. & Glagov, S. Role of medial lamellar architecture in the pathogenesis of aortic aneurysms. *Journal of Vascular Surgery* **1,** 442–448 (1984).

5. Masuda, H. *et al.* Adaptive Remodeling of Internal Elastic Lamina and Endothelial Lining During Flow-Induced Arterial Enlargement. *Arteriosclerosis, Thrombosis, and Vascular Biology* **19,** 2298–2307 (1999).

6. Koullias, G. J., Ravichandran, P., Korkolis, D. P., Rimm, D. L. & Elefteriades, J. A. Increased Tissue Microarray Matrix Metalloproteinase Expression Favors Proteolysis in Thoracic Aortic Aneurysms and Dissections. *The Annals of Thoracic Surgery* **78,** 2106–2110 (2004).

7. Ishii, T. & Asuwa, N. Collagen and Elastin Degradation by Matrix Metalloproteinases and Tissue Inhibitors of Matrix Metalloproteinase in Aortic Dissection. *Human Pathology* **31,** 640–646 (2000).

8. Sangiorgi, G. *et al.* Plasma levels of metalloproteinases-9 and -2 in the acute and subacute phases of type A and type B aortic dissection. *Journal of Cardiovascular Medicine* **7,** 307–315 (2006).

9. Nienaber, C. A. *et al.* The Diagnosis of Thoracic Aortic Dissection by Noninvasive Imaging Procedures. *The New England Journal of Medicine* **328,** 1–9 (1993).

10. LePage, M. A., Quint, L. E., Sonnad, S. S., Deeb, G. M. & Williams, D. M. Aortic Dissection: CT Features that Distinguish True Lumen from False Lumen. *American Journal of Roentgenology* **177,** 207–211 (2001).

11. Dinsmore, R. E. *et al.* MRI of Dissection of the Aorta: Recognition of the Intimal Tear and Differential Flow Velocities. *American Journal of Roentgenology* **146,** 1286–1288 (1986).

12. Karmonik, C. *et al.* Preliminary findings in quantification of changes in septal motion during follow-up of Type B aortic dissections. *Journal of Vascular Surgery* **55,** 1419–1426 (2012).

13. Ganten, M.-K. *et al.* Motion characterization of aortic wall and intimal flap by ECG-gated CT in patients with chronic B-dissection. *European Journal of Radiology* **72,** 146–153 (2009).

14. Yang, S. *et al.* Abdominal Aortic Intimal Flap Motion Characterization in Acute Aortic Dissection: Assessed with Retrospective ECG-Gated Thoracoabdominal Aorta Dual-Source CT Angiography. *PLoS ONE* **9,** e87664 (2014).

15. Murayama, T., Funabashi, N., Uehara, M., Takaoka, H. & Komuro, I. New classification of aortic dissection during the cardiac cyle as pulsating type and static type evaluated by electrocardiogram-gated multislice CT. *International Journal of Cardiology* **142,** 177–186 (2010).

16. Lemaire, S. A. & Russell, L. Epidemiology of thoracic aortic dissection. *Nature Reviews Cardiology* **8,** 103–113 (2011).

17. Mészaros, I. *et al.* Epidemiology and Clinicopathology of Aortic Dissection: A Population-Based Longitudinal Study Over 27 Years. *Chest* **117,** 1271–1278 (2000).

18. Cooley, D. A. & DeBakey, M. E. Surgical Considerations of Intrathoracic Aneurysms of the Aorta and Great Vessels. *Annals of Surgery* **135,** 660–680 (1952).

19. Hagan, P. G. *et al.* The International Registry of Acute Aortic Dissection (IRAD): New Insights Into an Old Disease. *The Journal of the American Medical Association* **283,** 897–903 (2000).

20. Criado, F. J. Aortic Dissection: A 250-Year Perspective. *Texas Heart Institute Journal* **38,** 694–700 (2011).

21. Januzzi, J. L. *et al.* Comparison of Aortic Dissection in Patients With and Without Marfan's Syndrome (Results from the International Registry of Aortic Dissection). *The American Journal of Cardiology* **94,** 400–402 (2004).

22. Albornoz, G. *et al.* Familial Thoracic Aortic Aneurysms and Dissections - Incidence, Modes of Inheritance, and Phenotypic Patterns. *The Annals of Thoracic Surgery* **82,** 1400–1406 (2006).

23. Clough, R. E. & Nienaber, C. A. Management of acute aortic syndromes. *Nature Reviews Cardiology* **12,** 103–114 (2015).

24. Elefteriades, J. A. *et al.* Management of Descending Aortic Dissection. *The Annals of Thoracic Surgery* **67,** 2002–2005 (1999).

25. Ince, H. & Nienaber, C. A. Diagnosis and Management of Patients with Aortic Dissection. *Heart* **93,** 266–270 (2007).

26. Khan, I. A. & Nair, C. K. Clinical, Diagnostic, and Management Perspectives of Aortic Dissection. *Chest* **122,** 311–328 (2002).

27. Nienaber, C. A. & Clough, R. E. Management of acute aortic dissection. *Lancet* **385,** 800–811 (2015).

28. Tsai, T. T., Nienaber, C. A. & Eagle, K. A. Acute Aortic Syndromes. *Circulation* **112,** 3802–3813 (2005).

29. Cohn, L. & Adams, D. H. *Cardiac Surgery in the Adult* 5th ed. (McGraw-Hill Education, 2017).

30. Cooley, D. A. Surgical Management of Aortic Dissection. *Texas Heart Institute Journal* **17,** 289–301 (1990).

31. Cronenwett, J. L. & Johnston, K. W. *Rutherford's Vascular Surgery* 8th edition (Saunders, 2014).

32. Bozinovski, J. & Coselli, J. S. Outcomes and Survival in Surgical Treatment of Descending Thoracic Aorta With Acute Dissection. *The Annals of Thoracic Surgery* **85,** 965–971 (2008).

33. Fattori, R. *et al.* Complicated Type B Dissection: Is Surgery Still the Best Option? A report from the International Registry of Acute Aortic Dissection. *JACC: Cardiovascular Interventions* **1,** 395–402 (2008).

34. Cambria, R. P. Surgical Treatment of Complicated Distal Aortic Dissection. *Seminars in Vascular Surgery* **15,** 97–107 (2002).

35. Lansman, S. L. *et al.* Acute Type B Aortic Dissection: Surgical Therapy. *The Annals of Thoracic Surgery* **74,** S1833–1835 (2002).

36. Trent, M. S. *et al.* A balloon-expandable intravascular stent for obliterating experimental aortic dissection. *Journal of Vascular Surgery* **11,** 707–717 (1990).

37. Nienaber, C. A. *et al.* Nonsurgical reconstruction of thoracic aortic dissection by stent-graft placement. *The New England Journal of Medicine* **340,** 1539–1545 (1999).

38. Dake, M. D. *et al.* Endovascular Stent-Graft Placement for the Treatment of Acute Aortic Dissection. *The New England Journal of Medicine* **340,** 1546–1552 (1999).

39. Chavan, A. *et al.* Endoluminal treatment of aortic dissection. *European Radiology* **13,** 2521–2534 (2003).

40. Buffolo, Ê., da Fonseca, J. H., de Souza, J. A. & Alves, C. M. Revolutionary Treatment of Aneurysms and Dissections of Descending Aorta: The Endovascular Approach. *The Annals of Thoracic Surgery* **74,** S1815–S1817 (2002).

41. Van Bogerijen, G. H., Williams, D. M. & Patel, H. J. TEVAR for complicated acute type B dissection with malperfusion. *Annals of Cardiothoracic Surgery* **3,** 423–427 (2014).

42. Doss, M. *et al.* Emergent Endovascular Stent Grafting for Perforated Acute Type B Dissections and Ruptured Thoracic Aortic Aneurysms. *The Annals of Thoracic Surgery* **76,** 493–498 (2003).

43. Duebener, L. F. *et al.* Emergency Endovascular Stent-Grafting for Life-Threatening Acute Type B Aortic Dissections. *The Annals of Thoracic Surgery* **78,** 1261–1267 (2004).

44. Nienaber, C. A. *et al.* Randomized Comparison of Strategies for Type B Aortic Dissection: The INvestigation of STEnt Grafts in Aortic Dissection (INSTEAD) Trial. *Circulation* **120,** 2519–2528 (2009).

45. Nienaber, C. A. *et al.* Endovascular Repair of Type B Aortic Dissection: Long-term Results of the Randomized Investigation of Stent Grafts in Aortic Dissection Trial. *Circulation Cardiovascular Interventions* **6,** 407–416 (2013).

46. Tsai, T. T. *et al.* Partial Thrombosis of the False Lumen in Patients with Acute Type B Aortic Dissection. *The New England Journal of Medicine* **357,** 349–359 (2007).

47. Akutsu, K. *et al.* Effects of the patent false lumen on the long-term outcome of type B acute aortic dissection. *European Journal of Cardio-thoracic Surgery* **26,** 359–366 (2004).

48. Tanaka, A. *et al.* Influence of the false lumen status on clinical outcomes in patients with acute type B aortic dissection. *Journal of Vascular Surgery* **59,** 321–326 (2014).

49. Sakaguchi, G. *et al.* Patency of distal false lumen in acute dissection: extent of resection and prognosis. *Interactive Cardiovascular and Thoracic Surgery* **6,** 204–208 (2007).

50. Blount, K. J. & Hagspiel, K. D. Aortic Diameter, True Lumen, and False Lumen Growth Rates in Chronic Type B Aortic Dissection. *American Journal of Roentgenology* **192,** W222–W229 (2009).

51. Bernard, Y. *et al.* False Lumen Patency as a Predictor of Late Outcome in Aortic Dissection. *The American Journal of Cardiology* **87,** 1378–1382 (2001).

52. Eggebrecht, H. *et al.* Endovascular stent-graft treatment of aortic dissection: determinants of post-interventional outcome. *European Heart Journal* **26,** 489–497 (2005).

53. Trimarchi, S. *et al.* Importance of false lumen thrombosis in type B aortic dissection prognosis. *The Journal of Thoracic and Cardiovascular Surgery* **145,** S208–S212 (2013).

54. Durham, C. A. *et al.* Aneurysmal degeneration of the thoracoabdominal aorta after medical management of type B aortic dissections. *Journal of Vascular Surgery* **62,** 900–906 (2015).

55. Huptas, S. *et al.* Aortic Remodeling in Type B Aortic Dissection: Effects of Endovascular Stent-Graft Repair and Medical Treatment on True and False Lumen Volumes. *Journal of Endovascular Therapy* **16,** 28–38 (2009).

56. Evangelista, A. *et al.* Long-Term Outcome of Aortic Dissection With Patent False Lumen: Predictive Role of Entry Tear Size and Location. *Circulation* **125,** 3133–3141 (2012).

57. Qin, Y.-L., Deng, G., Li, T.-X., Jing, R.-W. & Teng, G.-J. Risk factors of incomplete thrombosis in false lumen after endovascular treatment of extensive acute type B aortic dissection. *Journal of Vascular Surgery* **56,** 1232–1238 (2012).

58. Park, K.-H. *et al.* Midterm Change of Descending Aortic False Lumen After Repair of Acute Type I Dissection. *The Annals of Thoracic Surgery* **87,** 103–108 (2009).

59. Sueyoshi, E., Sakamoto, I. & Uetani, M. Growth Rate of Affected Aorta in Patients With Type B Partially Closed Aortic Dissection. *The Annals of Thoracic Surgery* **88,** 1251–1257 (2009).

60. Sueyoshi, E., Sakamoto, I., Hayashi, K., Yamaguchi, T. & Imada, T. Growth Rate of Aortic Diameter in Patients With Type B Aortic Dissection During the Chronic Phase. *Circulation* **110,** (2004).

61. Onitsuka, S. *et al.* Long-Term Outcome and Prognostic Predictors of Medically Treated Acute Type B Aortic Dissections. *The Annals of Thoracic Surgery* **78,** 1268–73 (2004).

62. Ueki, C., Sakaguchi, G., Shimamoto, T. & Komiya, T. Prognostic Factors in Patients With Uncomplicated Acute Type B Aortic Dissection. *The Annals of Thoracic Surgery* **97,** 767–773 (2014).

63. Kim, K. M. *et al.* Aortic remodeling, volumetric analysis, and clinical outcomes of endoluminal exclusion of acute complicated type B thoracic aortic dissections. *Journal of Vascular Surgery* **54,** 316–326 (2011).

64. Yang, C.-P. O. *et al.* Aortic remodeling after endovascular repair with stainless steel-based stent graft in acute and chronic type B aortic dissection. *Journal of Vascular Surgery* **55,** 1600–1610 (2012).

65. Hirotani, T., Nakamichi, T., Munakata, M. & Takeuchi, S. Routine Extended Graft Replacement for an Acute Type A Aortic Dissection and the Patency of the Residual False Channel. *The Annals of Thoracic Surgery* **76,** 1957–1961 (2003).

66. Kusagawa, H. *et al.* Changes in False Lumen After Transluminal Stent-Graft Placement in Aortic Dissections: Six Years' Experience. *Circulation* **111,** 2951–2957 (2005).

67. Schoder, M. *et al.* Endovascular Repair of Acute Type B Aortic Dissection: Long-Term Follow-Up of True and False Lumen Diameter Changes. *The Annals of Thoracic Surgery* **83,** 1059–1066 (2007).

68. Xie, J., Zhou, J. & Fung, Y. C. Bending of Blood Vessel Wall: Stress-Strain Laws of the Intima-Media and Adventitial Layers. *Journal of Biomechanical Engineering* **117,** 136–145 (1995).

69. Cecchi, E. *et al.* Role of hemodynamic shear stress in cardiovascular disease. *Atherosclerosis* **214,** 249–256 (2011).

70. Furie, B. & Furie, B. C. Mechanisms of Thrombus Formation. *The New England Journal of Medicine* **359,** 938–949 (2008).

71. Jackson, S. P. The growing complexity of platelet aggregation. *Blood* **109,** 5087–5095 (2007).

72. Wellings, P. J. & Ku, D. N. Mechanisms of Platelet Capture Undery Very High Shear. *Cardiovascular Engineering and Technology* **3,** 161–170 (2012).

73. Casa, L. D. C. & Ku, D. N. High Shear Thrombus Formation under Pulsatile and Steady Flow. *Cardiovascular Engineering and Technology* **5,** 154–163 (2014).

74. Casa, L. D. C., Deaton, D. H. & Ku, D. N. Role of high shear rate in thrombosis. *Journal of Vascular Surgery* **61,** 1068–1080 (2015).

75. Ruggeri, Z. M. Von Willebrand factor: Looking back and looking forward. *Thrombosis and Haemostasis* **98,** 55–62 (2007).

76. Triplett, D. A. Coagulation and Bleeding Disorders: Review and Update. *Clinical Chemistry* **46,** 1260–1269 (2000).

77. Davì, G. & Patrono, C. Platelet Activation and Atherothrombosis. *The New England Journal of Medicine* **357,** 2482–2494 (2007).

78. Firbas, C., Siller-Matula, J. M. & Jilma, B. Targeting von Willebrand factor and platelet glycoprotein Ib receptor. *Expert Review of Cardiovascular Therapy* **8,** 1689–1701 (2010).

79. Leebeek, F. W. G. & Eikenboom, J. C. J. Von Willebrand's Disease. *The New England Journal of Medicine* **375,** 2067–2080 (2016).

80. Mazzucato, M., Cozzi, M. R., Pradella, P., Ruggeri, Z. M. & de Marco, L. Distinct roles of ADP receptors in von Willebrand factor-mediated platelet signaling and activation under high flow. *Blood* **104,** 3221–3227 (2004).

81. Nachman, R. L. & Rafii, S. Platelets, Petechiae, and Preservation of the Vascular Wall. *The New England Journal of Medicine* **359,** 1261–1270 (2008).

82. Panton, R. L. *Incompressible Flow* 4th ed. (Wiley, 2013).

83. White, F. M. *Viscous Fluid Flow* 3rd ed. (McGraw-Hill Education, 2005).

84. Caro, C. G., Pedley, T. J., Schroter, R. C. & Seed, W. A. *The Mechanics of the Circulation* 2nd ed. (Cambridge University Press, 2012).

85. Sutera, S. P. & Skalak, R. The History of Poiseuille's Law. *Annual Review of Fluid Mechanics* **25,** 1–20 (1993).

86. Pfitzner, J. Poiseuille and his law. *Anaesthesia* **31,** 273–275 (1976).

87. Martufi, G., Forneris, A., Appoo, J. J. & Martino, E. S. D. Is there a Role for Biomechanical Engineering in Helping to Elucidate the Risk Profile of the Thoracic Aorta? *The Annals of Thoracic Surgery* **101,** 390–398 (2016).

88. Doyle, B. J. & Norman, P. E. Computational Biomechanics in Thoracic Aortic Dissection: Today's Approaches and Tomorrow's Opportunities. *Annals of Biomedical Engineering* **44,** 71–83 (2016).

89. Suo, J., Oshinski, J. N. & Giddens, D. P. Effects of Wall Motion And Compliance on Flow Patterns in the Ascending Aorta. *Journal of Biomechanical Engineering* **125,** 347–354 (2003).

90. Naim, W. N. W. A. *et al.* A Perspective Review on Numerical Simulations of Hemodynamics in Aortic Dissection. *The Scientific World Journal* **2014** (2014).

91. Qiao, A., Yin, W. & Chu, B. Numerical simulation of fluid-structure interaction in bypassed DeBakey III aortic dissection. *Computer Methods in Biomechanics & Biomedical Engineering* **18,** 1173–1180 (2015).

92. Alimohammadi, M. *et al.* Aortic dissection simulation models for clinical support: fluid-structure interaction vs. rigid wall models. *BioMedical Engineering Online* **14,** 1–16 (2015).

93. Ahmed, S. B., Dillon-Murphy, D. & Figueroa, C. A. Computational Study of Anatomical Risk Factors in Idealized Models of Type B Aortic Dissection. *European Journal of Vascular and Endovascular Surgery* **52,** 736–745 (2016).

94. Cheng, S. W. K. *et al.* A computational fluid dynamic study of stent graft remodeling after endovascular repair of thoracic aortic dissections. *Journal of Vascular Surgery* **48,** 303–310 (2008).

95. Karmonik, C. *et al.* Computational Study of Haemodynamic Effects of Entry- and Exit-Tear Coverage in a DeBakey Type III Aortic Dissection: Technical Report. *European Journal of Vascular and Endovascular Surgery* **42,** 172–177 (2011).

96. Cheng, Z., Juli, C., Wood, N. B., Gibbs, R. G. J. & Xu, X. Y. Predicting flow in aortic dissection: Comparison of computational model with PC-MRI velocity measurements. *Medical Engineering & Physics* **36,** 1176–1184 (2014).

97. Karmonik, C. *et al.* Longitudinal computational fluid dynamics study of aneurysmal dilatation in a chronic DeBakey type III aortic dissection. *Journal of Vascular Surgery* **56,** 260–263 (2012).

98. Cheng, Z. *et al.* Initial findings and potential applicability of computational simulation of the aorta in acute type B dissection. *Journal of Vascular Surgery* **57,** 35S–43S (2013).

99. Cheng, Z., Wood, N. B., Gibbs, R. G. J. & Xu, X. Y. Geometric and Flow Features of Type B Aortic Dissection: Initial Findings and Comparison of Medically Treated and Stented Cases. *Annals of Biomedical Engineering* **43,** 177–189 (2014).

100. Shang, E. K. *et al.* Use of computational fluid dynamics studies in predicting aneurysmal degeneration of acute type B aortic dissections. *Journal of Vascular Surgery* **62,** 279–284 (2015).

101. Menichini, C. & Xu, X. Y. Mathematical modeling of thrombus formation in idealized models of aortic dissection: initial findings and potential applications. *Journal of Mathematical Biology* **73,** 1205–1226 (2016).

102. Menichini, C., Cheng, Z., Gibbs, R. G. J. & Xu, X. Y. Predicting false lumen thrombosis in patient-specific models of aortic dissection. *Journal of the Royal Society Interface* **13,** 20160759 (2016).

103. Rudenick, P. A., Bijnens, B. H., Segers, P., García-Dorado, D. & Evangelista, A. Assessment of Wall Elasticity Variations on Intraluminal Haemodynamics in Desceding Aortic Dissections Using a Lumped-Parameter Model. *PLoS ONE* **10,** e0124011 (2015).

104. Berguer, R., Parodi, J. C., Schlicht, M. S. & Khanafer, K. Experimental and Clinical Evidence Supporting Septectomy in the Primary Treatment of Acute Type B Thoracic Aortic Dissection. *Annals of Vascular Surgery* **29,** 167–173 (2015).

105. Rudenick, P. A., Bijnens, B. H., García-Dorado, D. & Evangelista, A. An in vitro phantom study on the influence of tear size and configuration on the hemodynamics of the lumina in chronic type B aortic dissections. *Journal of Vascular Surgery* **57,** 464–474 (2013).

106. Tsai, T. T. *et al.* Tear size and location impacts false lumen pressure in an ex vivo model of chronic type B aortic dissection. *Journal of Vascular Surgery* **47,** 844–851 (2008).

107. Chung, J. W. *et al.* True-Lumen Collapse in Aortic Dissection: Part II. Evaluation of Treatment Methods in Phantoms with Pulsatile Flow. *Radiology* **214,** 99–106 (2000).

108. Chung, J. W. *et al.* True-Lumen Collapse in Aortic Dissection: Part I. Evaluation of Causative Factors in Phantoms with Pulsatile Flow. *Radiology* **214,** 87–98 (2000).

109. Veger, H., Westenberg, J. & Visser, M. The Role of Branch Vessels in Aortic Type B Dissection: An *in vitro* study. *European Journal of Vascular and Endovascular Surgery* **49,** 375–381 (2015).

110. Dziodzio, T. *et al.* Experimental Acute Type B Aortic Dissection: Different Sites of Primary Entry Tears Cause Different Ways of Propagation. *The Annals of Thoracic Surgery* **91,** 724–727 (2011).

111. Faure, E. M. *et al.* Assessment of abdominal branch vessel patency after bare-metal stenting of the thoracoabdominal aorta in a human ex vivo model of acute type B aortic dissection. *Journal of Vascular Surgery* **61,** 1299–1305 (2015).

112. Lee, V. S. *et al.* Flow Quantification Using Fase Cine Phase-Contrast MR Imaging, Conventional Cine Phase-Contrast MR Imaging, and Doppler Sonography: In Vitro and In Vivo Validation. *American Journal of Roentgenology* **169,** 1125–1131 (1997).

113. Markl, M., Frydrychowicz, A., Kozerke, S., Hope, M. & Wieben, O. 4D Flow MRI. *Journal of Magnetic Resonance Imaging* **36,** 1015–1036 (2012).

114. Persson, M., Solem, J. E., Markenroth, K., Svensson, J. & Heyden, A. Phase Contrast MRI Segmentation Using Velocity and Intensity. *International Conference on Scale-Space Theories in Computer Vision* (2005).

115. Van Pelt, R. *et al.* Exploration of 4D MRI Blood-Flow Using Stylistic Visualization. *IEEE Transactions on Visualization and Computer Graphics* **16,** 1339–1347 (2010).

116. Van Pelt, R. *et al.* Interactive Virtual Probing of 4D MRI Blood-Flow. *IEEE Transactions on Visualization and Computer Graphics* **17,** 2153–2162 (2011).

117. Bissell, M. M., Dall'Armellina, E. & Choudhury, R. P. Flow vortices in the aortic root: *in vivo* 4D-MRI confirms predictions of Leonardo da Vinci. *European Heart Journal,* ehu011 (2014).

118. François, C. J. *et al.* Four-dimensional, flow-sensitive magnetic resonance imaging of blood flow patterns in thoracic aortic dissections. *The Journal of Thoracic and Cardiovascular Surgery* **145,** 1359–1366 (2013).

119. Allen, B. D. *et al.* Thoracic Aorta 3D Hemodynamics in Pediatric and Young Adult Patients With Bicuspid Aortic Valve. *Journal of Magnetic Resonance Imaging* **42,** 954–963 (2015).

120. Jung, B. *et al.* Investigation of hemodynamics in an in vitro system simulating left ventricular support through the right subclavian artery using 4-dimensional flow magnetic resonance imaging. *The Journal of Thoracic and Cardiovascular Surgery* **150,** 200–207 (2015).

121. Kilner, P. J., Yang, G. Z., Mohiaddin, R. H., Firmin, D. N. & Longmore, D. B. Helical and Retrograde Secondary Flow Patterns in the Aortic Arch Studied by Three-Directional Magnetic Resonance Velocity Mapping. *Circulation* **88,** 2235–2247 (1993).

122. Oechtering, T. H. *et al.* Time-resolved 3-dimensional magnetic resonance phase contrast imaging (4D Flow MRI) analysis of hemodynamics in valve-sparing aortic root repair with an anatomically shaped sinus prosthesis. *The Journal of Thoracic and Cardiovascular Surgery* **152,** 418–427 (2016).

123. Ziganshin, B. A., Dumfarth, J. & Elefteriades, J. A. Natural history of Type B aortic dissection: ten tips. *Annals of Cardiothoracic Surgery* **3,** 247–254 (2014).

124. Baliga, R. R. *et al.* The Role of Imaging in Aortic Dissection and Related Syndromes. *JACC: Cardiovascular Imaging* **7,** 406–424 (2014).

125. Takahara, Y., Sudo, Y., Mogi, K., Nakayama, M. & Sakurai, M. Total Aortic Arch Grafting for Acute Type A Dissection: Analysis of Residual False Lumen. *The Annals of Thoracic Surgery* **73,** 450–454 (2001).

126. Suzuki, T. *et al.* Clinical Profiles and Outcomes of Acute Type B Aortic Dissection in the Current Era: Lessons from the International Registry of Aortic Dissection (IRAD). *Circulation* **108,** II312–II317 (2003).

127. Melissano, G. *et al.* Evaluation of a new disease-specific endovascular device for type B aortic dissection. *The Journal of Thoracic and Cardiovascular Surgery* **136,** 1012–1018 (2008).

128. Williams, D. M. *et al.* The Dissected Aorta: Percutaneous Treatment of Ischemic Complications - Principles and Results. *Journal of Vascular and Interventional Radiology* **8,** 605–625 (1997).

129. Jia, X. *et al.* The results of stent graft versus medication therapy for chronic type B dissection. *Journal of Vascular Surgery* **57,** 406–414 (2013).

130. Umaña, J. P., Miller, D. C. & Mitchell, R. S. What Is the Best Treatment for Patients With Acute Type B Aortic Dissections - Medical, Surgical, or Endovascular Stent-Grafting? *The Annals of Thoracic Surgery* **74,** S1840–S1843 (2002).

131. Umaña, J. P. *et al.* Is medical therapy still the optimal treatment strategy for patients with acute type B aortic dissections? *The Journal of Thoracic and Cardiovascular Surgery* **124,** 896–910 (2002).

132. Clough, R. E., Waltham, M., Giese, D., Taylor, P. R. & Schaeffter, T. A new imaging method for assessment of aortic dissection using four-dimensional phase contrast magnetic resonance imaging. *Journal of Vascular Surgery* **55,** 914–923 (2012).

133. Clough, R. E. *et al.* A new method for quantification of false lumen thrombosis in aortic dissection using magnetic resonance imaging and a blood pool contrast agent. *Journal of Vascular Surgery* **54,** 1251–1258 (2011).

134. Tiwari, A. & Soucek, M. D. *Concise Encyclopedia of High Performance Silicones* (John Wiley & Sons, 2014).

135. *Characteristic properties of Silicone Rubber Compounds* Online. http://www.shinetsusilicone-global.com/catalog/pdf/rubber_e.pdf, 2005.

136. Vorp, D. A. *et al.* Wall Strength and Stiffness of Aneurysmal and Nonaneurysmal Abdominal Aorta. *Annals of the New York Academy of Science* **800,** 274–276 (1996).

137. Akhtar, R. *et al.* Nanoindentation of histological specimens: Mapping the elastic properties of soft tissues. *Journal of Materials Research* **24,** 638–646 (2009).

138. Haskett, D., Johnson, G., Zhou, A., Utzinger, U. & Geest, J. V. Microstructural and biomechanical alterations of the human aorta as a function of age and location. *Biomechanics and modeling in mechanobiology* **9,** 725–736 (2010).

139. Tolenaar, J. L. *et al.* Importance of entry tears in Type B aortic dissection prognosis. *Annals of Cardiothoracic Surgery* **2,** 631–632 (2013).

140. Tolenaar, J. L. *et al.* Number of Entry Tears is Associated with Aortic Growth in Type B Dissections. *The Annals of Thoracic Surgery* **96,** 39–42 (2013).

141. Slonim, S. M. *et al.* True Lumen Obliteration in Complicated Aortic Dissection: Endovascular Treatment. *Radiology* **201,** 161–166 (1996).

142. Nienaber, C. A. & Eagle, K. A. Aortic Dissection: New Frontiers in Diagnosis and Management: Part I: From Etiology to Diagnostic Strategies. *Circulation* **108,** 628–635 (2003).

143. Tsai, T. T., Trimarchi, S. & Nienaber, C. A. Acute Aortic Dissection: Perspectives from the International Registry of Acute Aortic Dissection (IRAD). *European Journal of Vascular and Endovascular Surgery* **37,** 149–159 (2009).

144. Ruggeri, Z. M. Platelet Adhesion under Flow. *Microcirculation* **16,** 58–83 (2009).

145. Ku, D. N., Giddens, D. P., Zarins, C. K. & Glagov, S. Pulsatile Flow and Atherosclerosis in the Human Carotid Bifurcation: Positive Correlation between Plaque Location and Low and Oscillating Shear Stress. *Arteriosclerosis, Thrombosis, and Vascular Biology* **5,** 293–302 (1985).

146. Jr, J. E. M., Xu, C., Glagov, S., Zarins, C. K. & Ku, D. N. Fluid wall shear stress measurements in a model of the human abdominal aorta: oscillatory behavior and relationship to atherosclerosis. *Atherosclerosis* **110,** 225–240 (1994).

147. Chatzizisis, Y. *et al.* Role of Endothelial Shear Stress in the Natural History of Coronary Atherosclerosis and Vascular Remodeling. *Journal of the American College of Cardiology* **49,** 2379–2393 (2007).

148. Ranjan, V., Xiao, Z. & Diamond, S. L. Constitutive NOS expression in cultured endothelial cells is elevated by fluid shear stress. *American Journal of Physiology,* H550–H555 (1995).

149. Davies, P. F. Hemodynamic shear stress and the endothelium in cardiovascular pathophysiology. *Nature Clinical Practice* **6,** 16–26 (2009).

150. Hwang, J. *et al.* Oscillatory Shear Stress Stimulates Endothelial Production of O_2^- from p47^{phox}-dependent NAD(P)H Oxidases, Leading to Monocyte Adhesion. *The Journal of Biological Chemistry* **278,** 47291–47298 (2003).

151. Sorescu, G. P. *et al.* Bone Morphogenic Protein 4 Produced in Endothelial Cells by Oscillatory Shear Stress Stimulates an Inflammatory Response. *The Journal of Biological Chemistry* **278,** 31128–31135 (2003).

152. Chen, D. *et al.* A patient-specific study of type-B aortic dissection: evaluation of true-false lumen blood exchange. *BioMedical Engineering Online* **12,** 1–16 (2013).

153. Birjiniuk, J. *et al.* Development and testing of a silicone *in vitro* model of descending aortic dissection. *Journal of Surgical Research* **198,** 502–507 (2015).

154. Reymond, P., Merenda, F., Perren, F., Rüfenacht, D. & Stergiopulos, N. Validation of a one-dimensional model of the systemic arterial tree. *American Journal of Physiology - Heart and Circulatory Physiology* **297,** H208–H222 (2009).

155. Ahrens, J., Geveci, B. & Law, C. in *Visualization Handbook* (eds Hansen, C. D. & Johnson, C. R.) 1st ed., 717–731 (Elsevier, 2005).

156. Lin, L. I.-K. A Concordance Correlation Coefficient to Evaluate Reproducibility. *Biometrics* **45,** 255–268 (1989).

157. Womersley, J. R. Method for the Calculation of Velocity, Rate of Flow and Viscous Drag in Arteries When the Pressure Gradient is Known. *Journal of Physiology* **127,** 553–563 (1955).

158. Mohr-Kahaly, S. *et al.* Ambulatory Follow-Up of Aortic Dissection by Transesophageal Two-Dimensional and Color-Coded Doppler Echocardiography. *Circulation* **80,** 24–33 (1989).

159. Clough, R. E., Zymvragoudakis, V. E., Biasi, L. & Taylor, P. R. Usefulness of new imaging methods for assessment of type B aortic dissection. *Annals of Cardiothoracic Surgery* **3,** 314–318 (2014).

160. Hope, T. A. *et al.* Comparison of Flow Patterns in Ascending Aortic Aneurysms and Volunteers Using Four-Dimensional Magnetic Resonance Velocity Mapping. *Journal of Magnetic Resonance Imaging* **26,** 1471–1479 (2007).

161. Guzzardi, D. G. *et al.* Valve-Related Hemodynamics Mediate Human Bicuspid Aortopathy: Insights From Wall Shear Stress Mapping. *Journal of the American College of Cardiology* **66,** 892–900 (2015).

162. Tolenaar, J. L. *et al.* Morphologic predictors of aortic dilatation in type B aortic dissection. *Journal of Vascular Surgery* **58,** 1220–1225 (2013).

163. Nienaber, C. A., Divchev, D., Palisch, H., Clough, R. E. & Richartz, B. Early and late management of type B aortic dissection. *Heart,* 1–7 (2014).

164. Lowe, G. D. O. Virchow's Triad Revisited: Abnormal Flow. *Pathophysiology of Haemostasis and Thrombosis* **33,** 455–457 (2003).

165. Dillon-Murphy, D., Noorani, A., Nordsletten, D. & Figueroa, C. A. Multimodality image-based computational analysis of haemodynamics in aortic dissection. *Biomechanics and modeling in mechanobiology* **15,** 857–876 (2016).

166. Stalder, A. *et al.* Quantitative 2D and 3D Phase Contrast MRI: Optimized Analysis of Blood Flow and Vessel Wall Parameters. *Magnetic Resonance in Medicine* **60,** 1218–1231 (2008).

167. Cibis, M. *et al.* Wall shear stress calculations based on 3D cine phase contrast MRI and computational fluid dynamics: a comparison study in healthy carotid arteries. *NMR in Biomedicine* **27,** 826–834 (2014).

168. Potters, W. V., van Ooij, P., Marquering, H., vanBavel, E. & Nederveen, A. J. Volumetric Arterial Wall Shear Stress Calculation Based on Cine Phase Contrast MRI. *Journal of Magnetic Resonance Imaging* **41,** 505–516 (2015).

169. Harloff, A. *et al.* In Vivo Assessment of Wall Shear Stress in the Atherosclerotic Aorta Using Flow-Sensitive 4D MRI. *Magnetic Resonance in Medicine* **63,** 1529–1536 (2010).

170. Frydrychowicz, A. *et al.* Three-Dimensional Analysis of Segmental Wall Shear Stress in the Aorta by Flow-Sensitive Four-Dimensional-MRI. *Journal of Magnetic Resonance Imaging* **30,** 77–84 (2009).

171. Cibis, M. *et al.* The Effect of Spatial and Temporal Resolution of Cine Phase Contrast MRI on Wall Shear Stress and Oscillatory Shear Index Assessment. *PLoS ONE* **11,** e0163316 (2016).

172. Jr, J. E. M. & Ku, D. N. Pulsatile Velocity Measurements in a Model of the Human Abdominal Aorta Under Resting Conditions. *Journal of Biomechanical Engineering* **116,** 337–346 (1994).

173. Oshinski, J. N., Ku, D. N., Mukundan, S., Loth, F. & Pettigrew, R. I. Determination of Wall Shear Stress in the Aorta with the Use of MR Phase Velocity Mapping. *Journal of Magnetic Resonance Imaging* **5,** 640–647 (1995).

174. Oyre, S., Pedersen, E. M., Ringgaard, S., Boesiger, P. & Paaske, W. P. In vivo Wall Shear Stress Measured by Magnetic Resonance Velocity Mapping in the Normal Human Abdominal Aorta. *European Journal of Vascular and Endovascular Surgery* **13,** 263–271 (1997).

175. Oyre, S. *et al.* Accurate Noninvasive Quantitation of Blood Flow, Cross-Sectional Lumen Vessel Area and Wall Shear Stress by Three-Dimensional Paraboloid Modeling of Magnetic Resonance Imaging Velocity Data. *Journal of the American College of Cardiology* **32,** 128–134 (1998).

176. Van Ooij, P. *et al.* A Methodology to Detect Abnormal Relative Wall Shear Stress on the Full Surface of the Thoracic Aorta Using Four-Dimensional Flow MRI. *Magnetic Resonance in Medicine* **73,** 1216–1227 (2015).

177. Van Ooij, P. *et al.* Age-Related Changes in Aortic 3D Blood Flow Velocities and Wall Shear Stress: Implications for the Identification of Altered Hemodynamics in Patients with Aortic Valve Disease. *Journal of Magnetic Resonance Imaging,* 1–11 (2015).

178. Ehrlich, M. P. *et al.* Midterm Results After Endovascular Treatment of Acute, Complicated Type B Aortic Dissection. *The Annals of Thoracic Surgery* **90,** 1444–1449 (2010).

179. Wilkinson, D. A., Patel, H. J., Williams, D. M., Dasika, N. L. & Deeb, G. M. Early Open and Endovascular Thoracic Aortic Repair for Complicated Type B Aortic Dissection. *The Annals of Thoracic Surgery* **96,** 23–30 (2013).

180. Szeto, W. Y. *et al.* Results of a New Surgical Paradigm: Endovascular Repair for Acute Complicated Type B Aortic Dissection. *The Annals of Thoracic Surgery* **86,** 87–94 (2008).

181. Palma, J. H., de Souza, J. A. M., Alves, C. M. R., Carvalho, A. C. & Buffolo, E. Self-Expandable Aortic Stent-Grafts for Treatment of Descending Aortic Dissections. *The Annals of Thoracic Surgery* **73,** 1138–1142 (2002).

182. DiMusto, P. D. *et al.* Endovascular management of type B aortic dissection. *Journal of Vascular Surgery* **52,** 26S–36S (2010).

183. Neuhauser, B., Greiner, A., Jaschke, W., Chemelli, A. & Fraedrich, G. Serious complications following endovascular thoracic aortic stent-graft repair for type B dissection. *European Journal of Cardio-thoracic Surgery* **33,** 58–63 (2008).

184. Won, J. Y. *et al.* Problems Encountered during and after Stent-Graft Treatment of Aortic Dissection. *Journal of Vascular and Interventional Radiology* **17,** 271–281 (2006).

185. Dong, Z. *et al.* Stent graft-induced new entry after endovascular repair for Stanford type B aortic dissection. *Journal of Vascular Surgery* **52,** 1450–1458 (2010).

186. Pantaleo, A. *et al.* Distal Stent Graft-Induced New Entry: An Emerging Complication of Endovascular Treatment in Aortic Dissection. *The Annals of Thoracic Surgery* **102,** 527–533 (2016).

187. Brunkwall, J., Kasprzak, P., Verhoeven, E., Heijman, R. & Taylor, P. Endovascular Repair of Acute Uncomplicated Aortic Type B Dissection Promotes Aortic Remodeling: 1 Year Results of the ADSORB Trial. *European Journal of Vascular and Endovascular Surgery* **48,** 285–291 (2014).

188. Hughes, G. C. Management of acute type B aortic dissection; ADSORB trial. *The Journal of Thoracic and Cardiovascular Surgery* **149,** S158–S162 (2015).

189. Melissano, G. *et al.* Volume changes in aortic true and false lumen after the "PETTICOAT" procedure for type B aortic dissection. *Journal of Vascular Surgery* **55,** 641–651 (2012).

190. Mahadevia, R. *et al.* Bicuspid Aortic Cusp Fusion Morphology Alters Aortic Three-Dimensional Outflow Patterns, Wall Shear Stress, and Expression of Aortopathy. *Circulation* **129,** 673–682 (2014).

191. Roach, M. R. An experimental study of the production and time course of post-stenotic dilatation in the femoral and carotid arteries of adult dogs. *Circulation Research* **13,** 537–551 (1963).

192. Hashimoto, S. *et al.* Assessment of Transesophageal Doppler Echography in Dissecting Aortic Aneurysm. *Journal of the American College of Cardiology* **14,** 1253–1262 (1989).

193. Erbel, R. *et al.* Effect of medical and surgical therapy on aortic dissection evaluated by transesophageal echocardiography: Implications for Prognosis and Therapy. *Circulation* **87,** 1604–1615 (1993).

194. Iliceto, S. *et al.* Color Doppler evaluation of aortic dissection. *Circulation* **75,** 748–755 (1987).

195. Meredith, E. L. & Masani, N. D. Echocardiography in the emergency assessment of acute aortic syndromes. *European Journal of Echocardiography* **10,** i31–i39 (2009).

196. Schwein, A. *et al.* Feasibility of three-dimensional magnetic resonance imaging angiography-fluoroscopy image fusion technique in guiding complex endovascular aortic procedures in patients with renal insufficiency. *Journal of Vascular Surgery* (2016).